Development of $Cu_2ZnSn(S,Se)_4$ based solar cells

Andrew Fairbrother

Development of $Cu_2ZnSn(S,Se)_4$ based solar cells

Presented by Andrew Fairbrother

Thesis directors: Edgardo Saucedo and Alejandro Pérez-Rodríguez

Thesis tutor: Alejandro Pérez-Rodríguez

Thesis submitted February 2014 in completion of the requirements for the Doctor of Philosophy in Engineering and Advanced Technologies

University of Barcelona

Faculty of Physics, Department of Electronics

Table of Contents

Chapter 5.3 "Development of a selective chemical etch to improve the conversion efficiency of Zn-rich Cu_2ZnSnS_4 solar cells"

List of acronyms used in this work

CIGSe – $Cu(In,Ga)Se_2$

CTP – conventional thermal processing

CVD – chemical vapor deposition

Cu_2SnS_3 – CTS

Cu_2SnSe_3 – CTSe

CZTS – Cu_2ZnSnS_4

CZTSe – $Cu_2ZnSnSe_4$

CZTSSe – $Cu_2ZnSn(S,Se)_4$

GB – grain boundary

FWHM – full-width-at-half-max

NHH – nearest neighbor hopping

OVC – ordered vacancy compound

PCM – phonon confinement model

PV – photovoltaic

PVD – physical vapor deposition

RTP – rapid thermal processing

SEM – scanning electron microscopy

TCO – transparent conducting oxide

XRD – x-ray diffraction

XRF – x-ray fluorescence (spectroscopy)

Preface: Publications and summary of the thesis

The work presented in this thesis was carried out at the Catalonia Institute for Energy Research (IREC) in Sant Adrià de Besòs (Barcelona), Spain from 2011 to 2014. It is about the processing and characterization of $Cu_2ZnSn(S,Se)_4$ (CZTSSe) films for use as light absorbing layers in thin film photovoltaic (PV) devices. Each chapter is structured around one or more articles accepted or already published in peer-reviewed journals, including the following which are submitted in accord with the requirements for the Doctor of Philosophy in Engineering and Advanced Technologies at the University of Barcelona:

A. Fairbrother, E. García-Hemme, V. Izquierdo-Roca, X. Fontané, F. A. Pulgarín-Agudelo, O. Vigil-Galán, A. Pérez-Rodríguez, E. Saucedo. Development of a selective chemical etch to improve the conversion efficiency of Zn-rich Cu_2ZnSnS_4 solar cells, *Journal of the American Chemical Society* **2012**, *134 (19)*, 8018, DOI: 10.1021/ja301373e

C. M. Ruiz, X. Fontané, A. Fairbrother, V. Izquierdo-Roca, C. Broussillou, S. Bodnar, A. Pérez-Rodríguez, V. Bermúdez. Impact of electronic defects on the Raman spectra from electrodeposited $Cu(In,Ga)Se_2$ solar cells: Application for non-destructive defect assessment, *Applied Physics Letters* **2013**, *102*, 091106, DOI: 10.1063/1.4793418

A. Fairbrother, X. Fontané, V. Izquierdo-Roca, M. Espindola-Rodriguez, S. López-Marino, M. Placidi, J. López-García, A. Pérez-Rodríguez, E. Saucedo. Single-step sulfo-selenization method to synthesize $Cu_2ZnSn(S_ySe_{1-y})_4$ absorbers from metallic stack precursors, *ChemPhysChem* **2013**, *14 (9)*, 1836, DOI: 10.1002/cphc.201300157

A. Fairbrother, E. Saucedo, X. Fontané, V. Izquierdo-Roca, D. Sylla, M. Espindola-Rodriguez, F. A. Pulgarín-Agudelo, O. Vigil-Galán, A. Pérez-Rodríguez. Secondary phase formation in Zn-rich $Cu_2ZnSnSe_4$-based solar cells annealed in low pressure and temperature conditions, *Progress in Photovoltaics: Research and Applications* **2014**, accepted, in press, DOI: 10.1002/pip.2473

A. Fairbrother, V. Izquierdo-Roca, X. Fontané, M. Ibáñez, A. Cabot, E. Saucedo, A. Pérez-Rodríguez. ZnS grain size effects on near-resonant Raman scattering: Optical non-destructive grain size estimation, *CrystEngComm* **2014**, accepted, in press, DOI:10.1039/C3CE42578A

The thesis is structured into six chapters. The first chapter is an introduction into photovoltaics, including device structure and physics, motivation for the study of photovoltaics, and the current market situation and state of development. The focus is on thin film photovoltaics, in particular those based on chalcogenide compounds such as $Cu(In,Ga)Se_2$ (CIGSe) and mainly CZTSSe. The advantages and disadvantages of chalcogenide technologies, and of CZTSSe over CIGSe, are presented. An introduction into Raman scattering spectroscopy is made, because this technique is referred to frequently in subsequent chapters. Finally, the objectives of the thesis are detailed. The second chapter is an examination of the Cu-Zn-Sn-S(Se) material system, with particular focus on the secondary phases commonly encountered. The formation of secondary phases is very prevalent in this four or five element system because of the non-stoichiometric compositions used for the highest performing devices, namely Cu-poor and Zn-rich. Phase identification in some cases proves rather difficult, because some of the main phases have similar structural characteristics, which limits the use of conventional materials characterization methods such as x-ray diffraction. Raman scattering spectroscopy is shown to be especially useful in this material system, and this chapter is concluded with an analysis of one of the most common secondary phases (ZnS) in the paper "ZnS grain size effects on near-resonant Raman scattering: Optical non-destructive grain size estimation". Note that within the text of the thesis a short abstract of each article is presented, but the actual articles are found in the Appendix.

Chapter 3 details some the material properties of CZTSSe, such as crystal structure, defects, and related structural, optical, and electronic properties. Part of this chapter is based on a paper in preparation in which the electronic and chemical properties of CZTS films are studied by temperature dependent resistance measurements. Then a major part of this chapter is based on the paper "Impact of electronic defects on the Raman spectra from electrodeposited $Cu(In,Ga)Se_2$ solar cells: Application for non-destructive defect assessment". In this paper admittance spectroscopy is used to study the density of two main defect types in CIGSe, and these results are correlated with spectral features in Raman scattering measurements. CZTSSe is in a much earlier stage of research, so the defect structure is not clearly understood and a similar study is not yet feasible with this material. However, preliminary work to be published with CZTSSe in this line of study is presented, in which spectral features are correlated to changes in grain size (i.e. phonon confinement effects) and composition (i.e. variations in defect type and density).

The fourth and fifth chapters constitute the main body of the work and to date are the principle contributions of the author to the study of CZTSSe. Chapter 4 is about the deposition and thermal processing of CZTSSe thin films. The bulk of this chapter is based on the papers "Secondary phase formation in Zn-rich $Cu_2ZnSnSe_4$-based solar cells annealed in low pressure and temperature conditions" and "Single-step sulfo-selenization method to synthesize $Cu_2ZnSn(S_ySe_{1-y})_4$ absorbers from metallic stack precursors". The first focuses on $Cu_2ZnSnSe_4$, and the effect of annealing temperature and precursor composition on phase formation are studied. The other is quite unique in this field because it presents a method of simultaneous sulfurization and selenization of metallic precursor stacks to form $Cu_2ZnSn(S_ySe_{1-y})_4$ films. Typically CZTSSe is formed from non-metallic precursors or via the synthesis of nanoparticles. In each of these works Raman scattering spectroscopy is used regularly to study the phase formation.

Chapter 5 is in many respects the culmination and application of the ideas presented in the previous chapters and presents work on kesterite-based solar cell devices. It is about the optimization of device structure, including front and back interfaces. It is structured around the publication "Development of a selective chemical etch to improve the conversion efficiency of Zn-rich Cu_2ZnSnS_4 solar cells". Ultimately each of the previous subjects – materials properties, secondary phases, deposition and thermal processing – influence the final devices properties, so this chapter combines all of these elements and shows how they influence the performance of solar cell devices.

The final chapter of the thesis includes a summary and conclusion of the work.

Finally, the following papers are others, in addition to the five listed above, authored or co-authored by Andrew Fairbrother, and which are related to this thesis work:

A. Fairbrother, L. Fourdrinier, X. Fontané, V. Izquierdo-Roca, M. Dimitrievska, A. Pérez-Rodgríguez, E. Saucedo. Precursor stack ordering effects in $Cu_2ZnSnSe_4$ thin films prepared by rapid thermal processing, submitted and under review, **2014**.

A. Fairbrother, E. Saucedo, X. Fontané, V. Izquierdo-Roca, D. Sylla, M. Espíndola-Rodríguez, F.A. Pulgarín-Agudelo, O. Vigil-Galán, A. Perez-Rodriguez. Preparation of 4.8% efficiency $Cu_2ZnSnSe_4$ based solar cell by a two step process, *Proceedings of the 38th IEEE Photovoltaic Specialists Conference (PVSC)* **2012**, 002679

M. Ibáñez, D. Cadavid, D. Zamani, N. García-Castelló, V. Izquierdo-Roca, W. Li, A. Fairbrother, J.D. Prades, A. Shavel, J. Arbiol. Composition control and thermoelectric properties of quaternary chalcogenide nanocrystals: the case of stannite $Cu_2CdSnSe_4$, *Chemistry of Materials* **2012**, *24(3)*, 562

C.M. Ruiz, X. Fontane, A. Fairbrother, V. Izquierdo-Roca, C. Broussillou, S. Bodnar, A. Pérez-Rodríguez, V. Bermudez. Developing Raman scattering as quality control technique: Correlation with presence of electronic defects in CIGS-based devices, *Proceedings of the 38th IEEE Photovoltaic Specialists Conference (PVSC)* **2012**, 000455

A. Fairbrother, X. Fontané, V. Izquierdo-Roca, M. Espíndola-Rodríguez, S. López-Marino, M. Placidi, L. Calvo-Barrio, A. Pérez-Rodríguez. On the formation mechanisms of Cu_2ZnSnS_4 films prepared by sulfurization of metallic stacks, *Solar Energy Materials and Solar Cells* **2013**, *112*, 907

M. Espíndola-Rodríguez, M. Placidi, O. Vigil-Galán, V. Izquierdo-Roca, X. Fontané, A. Fairbrother, D. Sylla, E. Saucedo, A. Pérez-Rodríguez. Compositional optimization of photovoltaic grade Cu_2ZnSnS_4 films grown by pneumatic spray pyrolysis, *Thin Solid Films* **2013**, *535(1)*, 67

S. López-Marino, M. Placidi, A. Perez-Tomas, J. Llobet, V. Izquierdo-Roca, X. Fontané, A. Fairbrother, M. Espíndola-Rodríguez, D. Sylla, A. Perez-Rodriguez. Inhibiting the absorber/Mo-back contact decomposition reaction in $Cu_2ZnSnSe_4$ solar cells: the role of a ZnO intermediate nanolayer, *Journal of Materials Chemistry A* **2013**, *1,* 8338

O. Vigil-Galán, M. Espíndola-Rodríguez, M. Courel, X. Fontané, D. Sylla, V. Izquierdo-Roca, A. Fairbrother, E. Saucedo, A. Pérez-Rodríguez. Secondary phases dependence on composition ratio in sprayed Cu_2ZnSnS_4 thin films and its impact on the high power conversion efficiency, *Solar Energy Materials and Solar Cells* **2013**, *117,* 246

F.A. Pulgarín-Agudelo, S. López-Marino, A. Fairbrother, M. Placidi, V. Izquierdo-Roca, P.J. Sebastián, F. Ramos, B. Pina, A. Perez-Rodriguez, E. Saucedo. A thermal route to synthesize photovoltaic grade $CuInSe_2$ films from printed CuO/In_2O_3 nanoparticle-based inks under Se atmosphere, *Journal of Renewable and Sustainable Energy* **2013**, *5(5)*, 053140

F.A. Pulgarín–Agudelo, M. Placidi, A. Fairbrother, X. Fontané, V. Izquierdo-Roca, P.J. Sebastian, F. Ramos, B. Pina, A. Pérez–Rodríguez, E. Saucedo. Synthesis of $CuInSe_2$ nanopowders by microwave assisted solvothermal method, *International Journal of Nanotechnology* **2013**, *10(1)*, 1029

S. López-Marino, Y. Sánchez, M. Placidi, A. Fairbrother, M. Espíndola-Rodríguez, X. Fontané, V. Izquierdo-Roca, J. López-García, L. Calvo-Barrio, A. Pérez-Rodríguez. ZnSe etching of Zn-rich $Cu_2ZnSnSe_4$: An oxidation route for improved solar-cell efficiency, *Chemistry - A European Journal* **2013**, *19(44)*, 14814

O. Vigil-Galán, M. Courel, M. Espíndola-Rodríguez, V. Izquierdo-Roca, E. Saucedo, A. Fairbrother. Toward a high Cu_2ZnSnS_4 solar cell efficiency processed by spray pyrolysis method, *Journal of Renewable and Sustainable Energy* **2013**, *5(5)*, 053137

M. Dimitrievska, A. Fairbrother, X. Fontané, T. Jawhari, V. Izquierdo-Roca, E. Saucedo, A. Pérez-Rodríguez. Multiwavelength excitation Raman scattering study of polycrystalline kesterite Cu_2ZnSnS_4 thin films, *Applied Physics Letters* **2014,** *104(2)*, 021901

Contribution of the author to publications in the thesis

The author of this work, Andrew Fairbrother, has been responsible for the design and coordination of experiments on the development of different technological processes, as well as the interpretation of experimental results. He has directly participated in the deposition by sputtering of the metallic precursor films, thermal processing, and in chemical treatments to remove secondary phases. The author has also coordinated characterization of the processes, with particular emphasis on the interpretation of measurements by Raman spectroscopy and their correlation with the optoelectronic characterization of the devices.

Chapter 2.3:

- A. Fairbrother, et al., "ZnS grain size effects on near-resonant Raman scattering: Optical non-destructive grain size estimation", *CrystEngComm* **2014**, DOI 10.1039/C3CE42578A

Work selected for cover page of the journal

Impact Factor (IF): 3.88

1st quartile in areas: Chemistry (multidisciplinary), Crystallography

This article explores the potential of Raman spectroscopy for the advanced characterization of the ZnS phase, taking advantage of the knowledge and know-how acquired by the author in the development and characterization other processes related to CZTSSe. This permitted him to synthesize a series of samples for the study, and report for the first time in literature the dependence of grain size on quasi-resonant Raman spectra. Andrew Fairbrother was also responsible for the interpretation of the Raman data, coordination of characterization of the films by SEM and XRD, and writing of the article.

Chapter 3.3:

- C. M. Ruiz, X. Fontané, A. Fairbrother, et al., "Impact of electronic defects on the Raman spectra from electrodeposited Cu(In,Ga)Se_2 solar cells: Application for non-destructive defect assessment", *Applied Physics Letters* **2013**, *102*, 091106, DOI: 10.1063/1.4793418.

IF: 3.79

1st quartile in areas: Physics (applied)

In this work analysis by admittance spectroscopy of CIGSe-based solar cells is studied and correlated to the spectral features of Raman peaks. The density and type of defects correlate to changes in the Raman

spectra. The work is especially relevant because it shows for the first time the direct impact of defects associated with selenium vacancies on the principal peak of CIGSe. This opens very interesting prospects for the use of Raman spectroscopy for the non-destructive detection of electronic defects in the absorber films. In this work Andrew Fairbrother coordinated the work between the groups at NEXCIS Photovoltaic Technology and the University of Aix-Marseille, participating in the defining of the processes used in the clean room at NEXCIS for the fabrication of the devices and films studied. This implicated the selection of growth conditions of the films with different composition to favor the formation of defects associated with selenium and excess copper. The author was also responsible for processing of the cells to selectively remove the buffer and TCO layers, in order to be able to perform measurements directly on the surface of the absorber films. Finally, he made a comparative analysis between the results of the electrical characterization and the Raman measurements which form the basis of the work, and assisted in draft preparation of the article.

Chapter 4.3:

- A. Fairbrother et al, "Secondary phase formation in Zn-rich $Cu_2ZnSnSe_4$-based solar cells annealed in low pressure and temperature conditions", *Progress in Photovoltaics: Research and Applications* **2014**, DOI: 10.1002/pip.2473

IF: 7.71

1st quartile in areas: Materials Science (multidisciplinary), Physics (Applied), Energy & Fuels

In this article Andrew Fairbrother designed and coordinated an ambitious work which included the synthesis of CZTSe films by selenization treatments of metallic precursors films with different compositions deposited by sputtering. The advanced characterization of the films by Raman spectroscopy led to identification of secondary phases present in different regions of the films (ZnSe and Sn-Se), and to determine how their formation and distribution is influenced by the process parameters. Also studied was the impact on optoelectronic properties of the devices based on these films. Andrew Fairbrother organized and completed the synthesis processes for the study, and was responsible for coordination of the different measurements made. The optimization of the process presence resulted in a maximum efficiency of 4.8%. The author was also the primary writer of the manuscript, and prepared the submission of all required files to the journal

Chapter 4.4:

- A. Fairbrother et al, "Single-step sulfo-selenization method to synthesize $Cu_2ZnSn(S_ySe_{1-y})_4$ absorbers from metallic stack precursors", *ChemPhysChem* **2013**, *14 (9),* 1836, DOI: 10.1002/cphc.201300157C

IF: 3.35

1st quartile in areas: Physics (atomic, molecular & chemical)

This work described a process of sulfo-selenization which permits the synthesis of photovoltaic grade films of CZTSSe solid solutions with compositional control in the range of selenium to sulfur-pure films. This allowed a detailed study of the structural and morphological properties of the films, and the optoelectronic properties of the solar cells. The novelty of this work is the formation of CZTSSe from metallic precursors. CZTSSe is typically formed from non-metallic precursors, but this process results in the simultaneous introduction of sulfur and selenium into the films. Andrew Fairbrother designed and carried out the sulfo-selenization study, and was responsible for the synthesis and characterization of the films and devices. He coordinated the interpretation of the results, and wrote the article.

Chapter 5.3:

- A. Fairbrother et al., "Development of a selective chemical etch to improve the conversion efficiency of Zn-rich Cu_2ZnSnS_4 solar cells", *Journal of the American Chemical Society* 2012, *134 (19),* 8018, DOI: 10.1021/ja301373e

IF: 10.68

1st quartile in areas: Chemistry (multidisciplinary)

In this article Andrew Fairbrother identified a major problem for CZTS technologies, namely the presence of secondary phases and ZnS especially. This is particularly prevalent because device-grade films are prepared in Zn-rich conditions. He developed a selective etching procedure to remove this phase, which resulted in significant improvements in device efficiency. He coordinated sample fabrication and characterization of the devices and films. He was also responsible for writing of the article, and coordinated the discussion between the other co-authors.

None of these articles have been used by other co-authors for their doctoral thesis.

Barcelona, 25 of February 2014

Alejandro Pérez-Rodríguez

Edgardo Saucedo Silva

Prefacio: Publicaciones y resumen de la tesis

El trabajo presentado en esta tesis fue realizado en el Instituto de Investigación en Energía de Catalunia (IERC) en Sant Adrìa del Besòs (Barcelona), España desde el año 2011 hasta el 2014. Se trata del procesamiento y caracterización de películas de $Cu_2ZnSn(S,Se)_4$ (CZTSSe) como absorbedores de luz en dispositivos fotovoltaicos de capa delgada. Cada capítulo está estructurado sobre uno o más artículos en preparación o ya publicados en revistas de "peer-review", incluyendo los siguientes que se utilizan para cumplir los requisitos para el Doctorado en Filosofía en Ingeniería y Tecnologías Avanzadas en la Universidad de Barcelona:

A. Fairbrother, E. García-Hemme, V. Izquierdo-Roca, X. Fontané, F. A. Pulgarín-Agudelo, O. Vigil-Galán, A. Pérez-Rodríguez, E. Saucedo. Development of a selective chemical etch to improve the conversion efficiency of Zn-rich Cu_2ZnSnS_4 solar cells, *Journal of the American Chemical Society* **2012**, *134 (19)*, 8018, DOI: 10.1021/ja301373e

C. M. Ruiz, X. Fontané, A. Fairbrother, V. Izquierdo-Roca, C. Broussillou, S. Bodnar, A. Pérez-Rodríguez, V. Bermúdez. Impact of electronic defects on the Raman spectra from electrodeposited $Cu(In,Ga)Se_2$ solar cells: Application for non-destructive defect assessment, *Applied Physics Letters* **2013**, *102*, 091106, DOI: 10.1063/1.4793418

A. Fairbrother, X. Fontané, V. Izquierdo-Roca, M. Espindola-Rodriguez, S. López-Marino, M. Placidi, J. López-García, A. Pérez-Rodríguez, E. Saucedo. Single-step sulfo-selenization method to synthesize $Cu_2ZnSn(S_ySe_{1-y})_4$ absorbers from metallic stack precursors, *ChemPhysChem* **2013**, *14 (9)*, 1836, DOI: 10.1002/cphc.201300157

A. Fairbrother, E. Saucedo, X. Fontané, V. Izquierdo-Roca, D. Sylla, M. Espindola-Rodriguez, F. A. Pulgarín-Agudelo, O. Vigil-Galán, A. Pérez-Rodríguez. Secondary phase formation in Zn-rich $Cu_2ZnSnSe_4$-based solar cells annealed in low pressure and temperature conditions, *Progress in Photovoltaics: Research and Applications* **2014**, accepted, in press, DOI: 10.1002/pip.2473

A. Fairbrother, V. Izquierdo-Roca, X. Fontané, M. Ibáñez, A. Cabot, E. Saucedo, A. Pérez-Rodríguez. ZnS grain size effects on near-resonant Raman scattering: Optical non-destructive grain size estimation, *CrystEngComm* **2014**, accepted, in press, DOI:10.1039/C3CE42578A

La tesis está estructurada en seis capítulos. El primer capítulo es una introducción a la tecnología fotovoltaica: fundamentos físicos de la fotovoltaica, estructura de los dispositivos, motivación por investigar la fotovoltaica, y el mercado y estado actual del campo. El enfoque principal es la tecnología fotovoltaica de capa delgada, en particular la basada en compuestos calcogenuros como $Cu(In,Ga)Se_2$ (CIGSe), pero principalmente CZTSSe. En la Tesis, se presentan las ventajas y desventajas de las tecnologías de calcogenuros, comparando los dos materiales más significativos, el CZTSSe y el CIGSe. Además se incluye una introducción a la espectroscopia Raman, debido a que es la técnica de caracterización más ampliamente utilizada en la Tesis. Por último, se detallan los objetivos de las tesis. El segundo capítulo es un estudio del sistema Cu-Zn-Sn-S(Se), con énfasis en las fases secundarias más comunes. La formación de fases secundarias es uno de los temas más relevantes en este sistema multi-elemental debido a las condiciones no-estequiométricas que se utiliza para obtener dispositivos de mayor eficiencia de conversión fotovoltaica, en particular rico en Zn y pobre en Cu. La identificación de las fases resulta difícil en ciertos casos, porque algunos de las fases principales tienen características estructurales muy similares, lo cual limita el uso de los métodos de caracterización convencional como la difracción de rayos-x. La espectroscopia Raman se ha revelado como especialmente útil en este sistema, y el capítulo concluye con un análisis de una de las fases secundarias más comunes (ZnS) en el articulo "ZnS grain size effects on near-resonant Raman scattering: Optical non-destructive grain size estimation".

El tercer capítulo trata de algunas propiedades fundamentales del CZTSSe, tal como la estructura cristalina, los defectos,las propiedades estructurales, ópticas, y electrónicas. Parte de este capítulo se basa en un artículo en preparación en el cual las propiedades eléctricas y químicas de películas CZTS se estudian utilizando medidas de resistividad en función de la temperatura. La siguiente parte del capítulo se basa en el articulo "Impact of electronic defects on the Raman spectra from electrodeposited $Cu(In,Ga)Se_2$ solar cells: Application for non-destructive defect assessment". En este artículo se utiliza espectroscopia de admitancia para identificar y medir la densidad de dos defectos principales en CIGSe, y los resultados están correlacionados con propiedades espectrales obtenidas mediante medidas de espectroscopia Raman. El CZTSSe se encuentra en un estado mucho menos desarrollado que el CIGSe, y la estructura de defectos no se conoce adecuadamente, por tanto un estudio parecido aun no es factible en este material. No obstante, se presenta un trabajo preliminar pendiente de publicación con CZTSSe en esta línea, y en dicho trabajo las propiedades espectrales están relacionados con cambios en tamaño

de grano (efectos de confinamiento quántico) y composición (variaciones en tipo y densidad de defectos).

Los capítulos cuatro y cinco constituyen el cuerpo principal de este trabajo, y hasta ahora son las contribuciones más importantes del autor en el estudio del CZTSSe. El Capitulo 4 trata del depósito y procesamiento térmico de películas de CZTSSe. La mayor parte de éste capítulo se basa en los artículos "Secondary phase formation in Zn-rich $Cu_2ZnSnSe_4$-based solar cells annealed in low pressure and temperature conditions" y "Single-step sulfo-selenization method to synthesize $Cu_2ZnSn(S_ySe_{1-y})_4$ absorbers from metallic stack precursors". El primero se enfoca en CZTSe, y el efecto de temperatura y composición del precursor en la formación de fases secundarias. El segundo artículo es único en este campo porque presenta una metodología de sulfurizar y selenizar simultáneamente capas metálicas precursor para formar películas de CZTSSe. Generalmente CZTSSe se forma a partir de precursores no-metálicas o a través la síntesis de nanopartículas. En cada uno de estos trabajos la espectroscopia Raman se utiliza ampliamente para estudiar la formación de fases.

El Capitulo 5 es, en muchos sentidos, la culminación y aplicación de ideas presentadas en capítulos anteriores y se centra en el estudio de dispositivos basados en kesteritas. Se describen los primeros resultados de la optimización de la estructura de los dispositivos, tanto la interfaz delantera como trastera. El capítulo se estructura en base a la publicación "Development of a selective chemical etch to improve the conversion efficiency of Zn-rich Cu_2ZnSnS_4 solar cells". Cada uno de los temas anteriores – propiedades, fases secundarias, depósito y procesamiento térmico – influye en las propiedades del dispositivo final, por tanto este capítulo combina todos estos elementos y demuestra su influencia en los dispositivos.

El último capítulo de la tesis es un resumen y conclusión del trabajo.
Por último, en los artículos descritos a continuación Andrew Fairbrother ha participado como autor o co-autor, adicionalmente a los presentados anteriormente que forman el núcleo de la Tesis y están relacionados al trabajo experimental desarrollado durante este período:

A. Fairbrother, L. Fourdrinier, X. Fontané, V. Izquierdo-Roca, M. Dimitrievska, A. Pérez-Rodgríguez, E. Saucedo. Precursor stack ordering effects in $Cu_2ZnSnSe_4$ thin films prepared by rapid thermal processing, submitted and under review, **2014**.

A. Fairbrother, E. Saucedo, X. Fontané, V. Izquierdo-Roca, D. Sylla, M. Espíndola-Rodríguez, F.A. Pulgarín-Agudelo, O. Vigil-Galán, A. Perez-Rodriguez. Preparation of 4.8% efficiency $Cu_2ZnSnSe_4$ based solar cell by a two step process, *Proceedings of the 38th IEEE Photovoltaic Specialists Conference (PVSC)* **2012**, 002679

M. Ibáñez, D. Cadavid, D. Zamani, N. García-Castelló, V. Izquierdo-Roca, W. Li, A. Fairbrother, J.D. Prades, A. Shavel, J. Arbiol. Composition control and thermoelectric properties of quaternary chalcogenide nanocrystals: the case of stannite $Cu_2CdSnSe_4$, *Chemistry of Materials* **2012**, *24(3)*, 562

C.M. Ruiz, X. Fontane, A. Fairbrother, V. Izquierdo-Roca, C. Broussillou, S. Bodnar, A. Pérez-Rodríguez, V. Bermudez. Developing Raman scattering as quality control technique: Correlation with presence of electronic defects in CIGS-based devices, *Proceedings of the 38th IEEE Photovoltaic Specialists Conference (PVSC)* **2012**, 000455

A. Fairbrother, X. Fontané, V. Izquierdo-Roca, M. Espíndola-Rodríguez, S. López-Marino, M. Placidi, L. Calvo-Barrio, A. Pérez-Rodríguez. On the formation mechanisms of Cu_2ZnSnS_4 films prepared by sulfurization of metallic stacks, *Solar Energy Materials and Solar Cells* **2013**, *112*, 907

M. Espíndola-Rodríguez, M. Placidi, O. Vigil-Galán, V. Izquierdo-Roca, X. Fontané, A. Fairbrother, D. Sylla, E. Saucedo, A. Pérez-Rodríguez. Compositional optimization of photovoltaic grade Cu_2ZnSnS_4 films grown by pneumatic spray pyrolysis, *Thin Solid Films* **2013**, *535(1)*, 67

S. López-Marino, M. Placidi, A. Perez-Tomas, J. Llobet, V. Izquierdo-Roca, X. Fontané, A. Fairbrother, M. Espíndola-Rodríguez, D. Sylla, A. Perez-Rodriguez. Inhibiting the absorber/Mo-back contact decomposition reaction in $Cu_2ZnSnSe_4$ solar cells: the role of a ZnO intermediate nanolayer, *Journal of Materials Chemistry A* **2013**, *1,* 8338

O. Vigil-Galán, M. Espíndola-Rodríguez, M. Courel, X. Fontané, D. Sylla, V. Izquierdo-Roca, A. Fairbrother, E. Saucedo, A. Pérez-Rodríguez. Secondary phases dependence on composition ratio in sprayed Cu_2ZnSnS_4 thin films and its impact on the high power conversion efficiency, *Solar Energy Materials and Solar Cells* **2013**, *117,* 246

F.A. Pulgarín-Agudelo, S. López-Marino, A. Fairbrother, M. Placidi, V. Izquierdo-Roca, P.J. Sebastián, F. Ramos, B. Pina, A. Perez-Rodriguez, E. Saucedo. A thermal route to synthesize photovoltaic grade $CuInSe_2$ films from printed CuO/In_2O_3 nanoparticle-based inks under Se atmosphere, *Journal of Renewable and Sustainable Energy* **2013**, *5(5)*, 053140

F.A. Pulgarín–Agudelo, M. Placidi, A. Fairbrother, X. Fontané, V. Izquierdo-Roca, P.J. Sebastian, F. Ramos, B. Pina, A. Pérez–Rodríguez, E. Saucedo. Synthesis of $CuInSe_2$ nanopowders by microwave assisted solvothermal method, *International Journal of Nanotechnology* **2013**, *10(1)*, 1029

S. López-Marino, Y. Sánchez, M. Placidi, A. Fairbrother, M. Espíndola-Rodríguez, X. Fontané, V. Izquierdo-Roca, J. López-García, L. Calvo-Barrio, A. Pérez-Rodríguez. ZnSe etching of Zn-rich $Cu_2ZnSnSe_4$: An oxidation route for improved solar-cell efficiency, *Chemistry - A European Journal* **2013**, *19(44)*, 14814

O. Vigil-Galán, M. Courel, M. Espíndola-Rodríguez, V. Izquierdo-Roca, E. Saucedo, A. Fairbrother. Toward a high Cu_2ZnSnS_4 solar cell efficiency processed by spray pyrolysis method, *Journal of Renewable and Sustainable Energy* **2013**, *5(5)*, 053137

M. Dimitrievska, A. Fairbrother, X. Fontané, T. Jawhari, V. Izquierdo-Roca, E. Saucedo, A. Pérez-Rodríguez. Multiwavelength excitation Raman scattering study of polycrystalline kesterite Cu_2ZnSnS_4 thin films, *Applied Physics Letters* **2014,** *104(2)*, 021901

Contribución del autor a las publicaciones de la tesis

El autor de esta memoria, Andrew Fairbrother, ha sido responsable del diseño y coordinación de los experimentos que se han definido para el desarrollo de los diferentes procesos tecnológicos, así como de la interpretación de los datos experimentales. El autor ha participado de forma directa en la realización de los procesos de depósito por sputtering de las capas precursoras metálicas y en los tratamientos químicos para la eliminación de las fases secundarias, así como en la realización de los tratamientos térmicos de recristalización. Finalmente, el autor ha coordinado también la caracterización de los procesos, con un protagonismo especial en la interpretación de las mediadas de espectroscopia Raman y su correlación con la caracterización eléctrica y optoelectrónica de los dispositivos.

Capítulo 2.3:

- A. Fairbrother, et al., "ZnS grain size effects on near-resonant Raman scattering: Optical non-destructive grain size estimation", *CrystEngComm* **2014**, DOI 10.1039/C3CE42578A

Trabajo seleccionado para la portada de la revista

IF: 3.88

1er quartil en área: Chemistry (multidisciplinary), Crystallography

Este artículo profundiza en el potencial de la espectroscopia Raman para la caracterización avanzada de las fases ZnS, aprovechando el conocimiento y "know-how" adquiridos por el autor en el desarrollo y caracterización avanzada de los procesos. Esto le ha permitido sintetizar un juego adecuado de muestras que ha posibilitado el desarrollo del estudio permitiendo reportar por primera vez en la literatura la dependencia de los espectros Raman obtenidos en condiciones de quasi-resonancia respecto del tamaño de grano. A. Fairbrother fue responsable también de la interpretación de los espectros Raman, y de su coordinación con la caracterización de las capas por miscroscopía SEM y XRD, así como de la redacción del artículo.

Capítulo 3.3:

- C. M. Ruiz, X. Fontané, A. Fairbrother, et al., "Impact of electronic defects on the Raman spectra from electrodeposited Cu(In,Ga)Se_2 solar cells: Application for non-destructive defect assessment", *Applied Physics Letters* **2013**, *102*, 091106, DOI: 10.1063/1.4793418.

IF: 3.79

1er quartil en área: Physics (applied)

En este trabajo se realiza un análisis mediante medidas de espectroscopia de admitancia de celdas de $Cu(In,Ga)Se_2$ y se estudia la correlación entre las características espectrales de los picos Raman de las capas absorbedoras y la densidad y tipo de defectos. El trabajo tiene una relevancia especialmente significativa, ya que muestra por primera vez en la literatura el impacto directo de defectos asociados a vacantes de Se sobre el pico principal Raman de la fase calcopirita, lo que abre perspectivas muy interesantes para la utilización de la espectroscopia Raman para la detección de forma no destructiva de defectos electrónicos en las capas absorbedoras. En este trabajo, A. Fairbrother coordinó la cooperación con los grupos de NEXCIS Photovoltaic Technology y de la Universidad Aix-Marseille, participando en la definición de los procesos que se utilizaron en la Sala Blanca de NEXCIS para la fabricación de las células estudiadas (lo que implicó seleccionar condiciones de crecimiento de las capas absorbedoras con diferente composición, para favorecer la formación de defectos asociados a defecto de Se y exceso de Cu). El autor fue responsable también del procesado de las celdas para la eliminación selectiva de las capas buffer y TCO (con el fin de poder acceder de forma directa a la superficie de las capas absorbedoras), y realizó el análisis comparativo entre los resultados de la caracterización eléctrica de los dispositivos y las medidas de espectroscopia Raman en que se basa el trabajo.

Capítulo 4.3:

- A. Fairbrother et al, "Secondary phase formation in Zn-rich $Cu_2ZnSnSe_4$-based solar cells annealed in low pressure and temperature conditions", *Progress in Photovoltaics: Research and Applications* **2014**, DOI: 10.1002/pip.2473

IF: 7.71

1er quartil en área: Materials Science (multidisciplinary), Physics (Applied), Energy & Fuels

En este artículo, A. Fairbrother diseñó y coordinó un ambicioso trabajo que incluyó la síntesis en el laboratorio de capas CZTSe mediante tratamientos de selenización de capas precursoras metálicas con diferente composición que fueron depositadas previamente por sputtering. La caracterización avanzada de las capas mediante espectrocopía Raman le permitió identificar las fases secundarias presentes en las diferentes regiones de las capas (ZnSe, SnSe) y determinar su dependencia de los parámetros tecnológicos y su impacto sobre las características optoelectrónicas de los dispositivos. A. Fairbrother puso a punto y llevó a cabo los procesos tecnológicos fundamentales para la síntesis de las capas absorbedoras y fue responsable de la coordinación de las diferentes medidas que le permitió identificar

y proponer los principales mecanismos que limitan la eficiencia de los dispositivos. La optimización realizada que en este estudio no ha incluido tratamientos de ataque selectivo del ZnSe, y se llego a obtener una eficiencia máxima de 4.8%.

Capítulo 4.4:

- A. Fairbrother et al, "Single-step sulfo-selenization method to synthesize $Cu_2ZnSn(S_ySe_{1-y})_4$ absorbers from metallic stack precursors", *ChemPhysChem* **2013**, *14 (9)*, 1836, DOI: 10.1002/cphc.201300157C

IF: 3.35

1er quartil en área: Physics (atomic, molecular & chemical)

Este trabajo describe la puesta a punto de un proceso de sulfo-selenizacion que permite la síntesis de capas de grado fotovoltaico de aleaciones $Cu_2ZnSn(S,Se)_4$ con composición controlada en todo el rango de composiciones (desde el seleniuro hasta el sulfuro), lo que ha permitido realizar un estudio detallado de la dependencia de las propiedades estructurales y morfológicas de las capas sintetizadas y de los parámetros optoelectrónicos de las celdas solares fabricadas con estas capas respecto de la composición de las aleaciones (relación S/(S+Se)). A. Fairbrother diseñó y puso a punto el proceso de sulfo-selenizacion, y fue responsable de la síntesis de las capas (partiendo de precursores metálicos depositados por sputtering) y de la caracterización de las celdas solares que fueron fabricadas con ellas. El autor coordinó también la interpretación de los datos experimentales, y la redacción del artículo, que permitió reportar en ese momento la obtención de celdas con una eficiencia máxima de hasta 4.4%. .

Capítulo 5.3:

- A. Fairbrother et al, "Development of a selective chemical etch to improve the conversion efficiency of Zn-rich Cu_2ZnSnS_4 solar cells", *Journal of the American Chemical Society* **2012**, *134 (19)*, 8018, DOI: 10.1021/ja301373e

IF: 10.68

1er quartil en área: Chemistry (multidisciplinary)

En este artículo, A. Fairbrother diseño los procesos para la evaluación de los tratamientos propuestos para la eliminación selectiva de fases ZnS, y coordinó las medidas, estando a cargo de la implementación y caracterización de las celdas solares y de la interpretación de las medidas de caracterización Raman para la detección de las fase ZnS en la superficie de los absorbedores y su dependencia de los procesos.

A. Fairbrother fue responsable también de la redacción del artículo y coordinó la discusión con los otros coautores.

Ninguno de estos artículos ha sido utilizado por los otros coautores total o parcialmente para su Tesis Doctoral.

Barcelona, 25 de Febrero de 2014

Alejandro Pérez Rodríguez

Edgardo Saucedo Silva

1. Introduction and objectives

This work is about the processing and characterization of $Cu_2ZnSn(S,Se)_4$ (CZTSSe) thin films, including the sulfur-pure Cu_2ZnSnS_4 (CZTS) and selenium-pure $Cu_2ZnSnSe_4$ (CZTSe) compounds. This class of compounds is being investigated as a potential light absorbing layer in thin film photovoltaics. The introduction includes an overview of photovoltaics (PV), including the motivation of mass PV production, the current economic picture, the main technologies, and the basic physical principle exploited by PV to generate electricity. There is also a more in-depth look at thin film photovoltaic technologies, including device structure and materials. The next to last section is about Raman scattering spectroscopy, which has proven to be an invaluable tool in characterization of the complex CZTSSe material system, and is referred to regularly throughout the thesis. The final section includes the objectives of the thesis.

1.1 Current state of photovoltaic technologies

Energy is the invisible driver of modern economies, and consumption has increased exponentially since the 19th century with the onset of the Industrial Revolution. The main source of energy, including electricity, is from fossil fuels such as coal and natural gas,[1] but in recent decades there has been a push towards the usage of renewable energy sources. This effort is driven by the need to reduce greenhouse emissions and mitigate climate change, and also improve energy security via domestic energy production. In this context the conversion of sunlight into electricity has significant potential to be a viable energy source because of the sheer abundance of solar irradiation. Thus the development and industrialization of PV technologies in order to exploit this renewable energy source has intensified in the past several years.

The installed PV capacity is rapidly increasing each year, but is still far from the desired TW level production. As of 2012 there is an installed capacity of 102 GW,[1] less than 1% of the total electricity production worldwide (note, this percentage is usually higher in developed countries, for example 6% in Germany and 7% in Italy).[1] The reasons for the low production levels are various. On one hand, the cost per MWh is still higher than electricity production by fossil fuels, approximately $65-136 vs $144 (estimates for plants entering service in 2018).[2] This often requires the implementation of governmental policies to encourage PV installation, including feed-in-tariffs (guaranteed prices for electricity injection into the grid). Other challenges are environmental, for example, the availability of solar irradiation varies regularly from season to season, and even minute by minute. Without a viable long term storage technology, this means that more continuous production sources are required, in other words, coal,

natural gas, and nuclear electricity generation. In spite of the technological and manufacturing challenges, as production is increased, costs are steadily declining, and further developments in each PV technology lead to increases in performance and reductions in production costs.[1] In fact, historically each time the installed capacity doubles, the price per Watt peak decreases about 22%.[3]

1.2 Photovoltaic effect and main technologies

Photovoltaic solar cells function by exploiting the photovoltaic effect, in which separating photo-generated charge carriers are carried out through an external circuit. As a semiconductor absorbs a photon, an electron-hole pair can be generated, which normally recombine and generate a small amount of heat. In a PV solar cell however, a built in electric field is used to separate the electron-hole pair before recombination. This is achieved by the formation of a semiconductor p-n junction, as illustrated in Figure 1.1. The band structure at the junction bends in order to align the Fermi level energies of the different layers, and generates an electric field in this region. Now when an absorbed photon generates and electron-hole pair, these charge carriers separated by the field and run outside of the device into an external circuit.

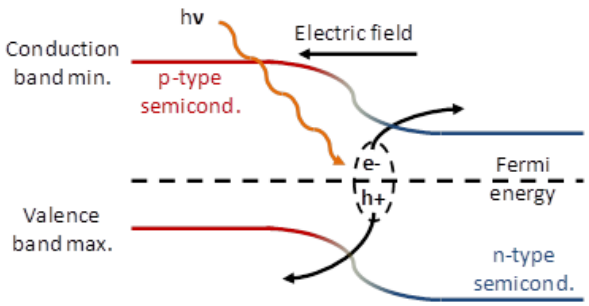

Figure 1.1. Band structure of a solar cell demonstrating the photovoltaic effect, with e-: free electron, h+: free hole, h**ν**: photon of a given energy.

As alluded to previously, there is actually a wide variety of PV technologies, though all operate on the same mechanism described above. PV is frequently divided into three generations of technologies. The first generation PV is the most developed, and includes mono- and poly-crystalline silicon. Research and development has been ongoing for decades, and the highest efficiency single junction solar cells are silicon-based (greater than 24%).[4] Silicon solar cells are slowly reaching their theoretical performance limit (29% given by the Shockley-Queisser limit)[5] so further improvements are harder and harder to come by, and they are limited by the high material cost, especially in the case of mono-crystalline

silicon. Additionally, because silicon has an indirect bandgap, and as a consequence a low absorption coefficient, relatively thick light absorbing layers (>100μm) are required, which increases module weight makes the layers inflexible. Nonetheless, as the most developed technology, about 90% of the PV market is controlled by the first generation technologies, though it is slowly decreasing and giving way to the second generation technologies.[1,3]

Second generation technologies are so-called thin film solar cells. Whereas the light absorbing layer in first generation PV is greater than 100 μm thick, thin film solar cells typically employ absorber layers which are less than 5 μm thick, even reaching submicron thickness. This is because of the use of direct bandgap materials which are much more efficient at absorbing light. In principle this confers a great advantage over silicon-based PV because this significantly reduces the material usage for modules and is potentially compatible with flexible substrates. Processing can be streamlined and costs may be reduced, especially with the development of roll-to-roll deposition. The main second generation technologies include $Cu(In,Ga)Se_2$ (CIGSe), CdTe, and stabilized amorphous silicon (a-Si:H). Some drawbacks of these technologies include the use of relatively rare or toxic elements (In, Ga, Cd, Te, Ag), and poor long-term performance (a-Si:H). These technologies currently account for about 10% of the PV market, and are at early stage of commercialization when compared to the first generation technologies. Further details of this generation are provided in the following section.

Third generation PV technologies are even less developed than the second generation PV, and are based on the incorporation of multiple ideas to increase efficiencies beyond the Shockley-Queisser theoretical limit. Some examples include intraband and tandem solar cells, photon up/down conversion, incorporation of quantum dots, and organic PV. Many of these technologies are attempts to use a broader spectrum of solar irradiation, because single junction solar cells (first and second generation) are limited by this. Some third generation technologies may also be considered thin film technologies, such as organic and dye sensitized solar cells, but because they employ non-conventional materials (i.e. organics), they are usually classed as third generation PV.

1.3 Thin film solar cells

Thin film photovoltaics based on CIGSe, CdTe, and a-Si:H form the second generation of photovoltaics, in between the mature and aging first generation mono- and poly-crystalline silicon technologies, and nascent third generation technologies intended to further lower cost and improve device efficiencies.

The device structure for a thin film (CIGSe-based) solar cell is shown in Figure 1.2, in what is called the substrate configuration. Thin film solar cells are typically characterized by a transparent front contact, usually a transparent conducting oxide (TCO) such as ZnO:Al, In_2O_3:Sn, and SnO_2:F, up to 500 nm thick. This layer acts as a conduit for the photo-generated electrons, and carries them to metal contacts. Beneath this is an n-type buffer layer, less than 100 nm thick, which, in conjunction with the p-type absorber, forms the p-n junction exploited for separation of the photo-generated charge carriers. The top two layers should have low electrical resistivity and be fairly transparent to allow light to pass through to the absorbing layer. The next lowest layer is the p-type semiconductor, which plays the role of absorbing the majority of incoming light, hence its commonly being referred to as the absorber layer, and has a thickness anywhere from submicron up to 5 µm. This layer is often used to describe a technology, for example, CIGSe-based solar cells use CIGSe as the absorbing layer, but many different materials can be used for the rest of the layers. Further down is the back contact layer which is usually a metal, but it may also be another semiconducting compound. And finally there is the substrate, which forms the basis of the solar cell, giving structural integrity to the entire device. The most commonly used substrate material is soda-lime glass because of its relatively low cost and the ease of working with a rigid substrate, but metal and polymer foils may also be used. Flexible substrates are of particular interest for low-weight applications, and for industrial roll-to-roll processing.

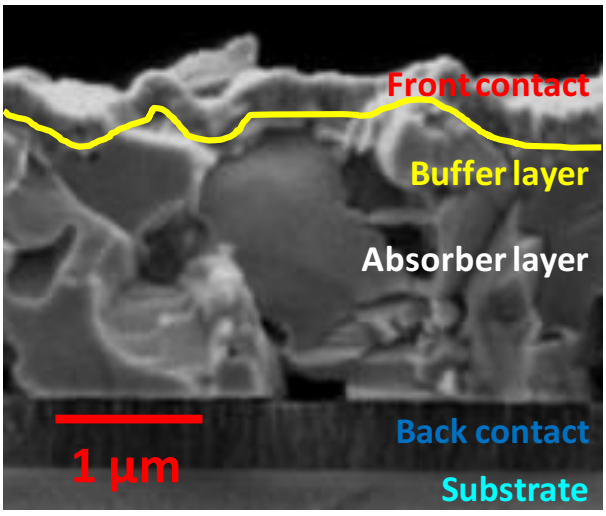

Figure 1.2. Thin film (CIGSe) solar cell device structure as seen by cross section.

CIGSe has proven to be the highest performing of thin film technologies in terms of device performance, recently achieving 20.8% on the laboratory scale.[6] The promise of CIGSe is also based on the potential

for cost reduction in module production compared to first generation silicon-based technologies from the lower material usage and the possibility of non-vacuum deposition for PV-grade material. However, CIGSe contains the relatively rare elements of In and Ga, in addition to Cd in the form of the commonly employed CdS buffer layer. These metals are a by-product of other mining operations, making "ramping up" of production difficult, and most operations are concentrated in a single country (China), which raises concerns about mid- to long-term material supply.[7,8] Additionally, there are toxicity concerns because of the use of heavy metals (Cd), and H_2Se gas which is often used in processing. These factors have led to investigation of absorber layers based on more earth abundant materials such as CZTSSe, in addition to more environmentally friendly buffer layers as alternatives to CdS. CZTSSe shares many commonalities with CIGSe, and as such is viewed as a potential replacement in long-term production of PV modules.

The development of CZTSSe-based solar cells has benefited tremendously from its similarities with CIGSe. By and large, the device structure has been copied (Figure 1.2), including the usage of a Mo back contact, CdS buffer layer, and ZnO:Al transparent conducting oxide layer (alternatively In_2O_3:Sn or SnO_2:F). Undoubtedly the use of an optimized structure for CIGSe has aided in the relatively rapid increase in efficiency up to 12.6% in a period of 17 years.[9] However, with time the differences between CZTSSe and CIGSe have become more apparent, and novel device structure and film processing must be developed in order to improve the efficiency of CZTSSe-based solar cells up to the 20% level of CIGSe. For example, CZTSSe has been shown to be unstable at high temperatures due to surface decomposition to form volatile Sn-S(Se) phases,[10,11] and also back interface decomposition because of the preferential formation of $MoS(Se)_2$.[12,13] Secondary phase formation is also a serious problem because of the non-stoichiometric compositions used for the highest efficiency devices, and identification of these phases requires more than conventional material characterization techniques such as x-ray diffraction.[14]

1.4 Raman scattering spectroscopy

Raman scattering spectroscopy has proven itself to be an invaluable tool in the characterization of thin film solar cells, especially with CZZTSe for reasons detailed in Chapter 2. It is based on the measurement of scattered light from a material. The physical process of light scattering is illustrated in Figure 1.3: monochromatic light of a known energy interacts with the material, and most light is elastically back-scattered (Rayleigh scattering); a small number of photons (typically 1 in 10^6) interacts with the crystal lattice and undergoes inelastic (Raman) scattering by generating (Stokes) or absorbing (anti-Stokes) a

phonon, and thus has a slightly lower or higher energy than the incident light. By measuring the energy of scattered light from a sample, Raman spectra can be generated, which are strongly dependent on material composition, structure, defects, and other factors.

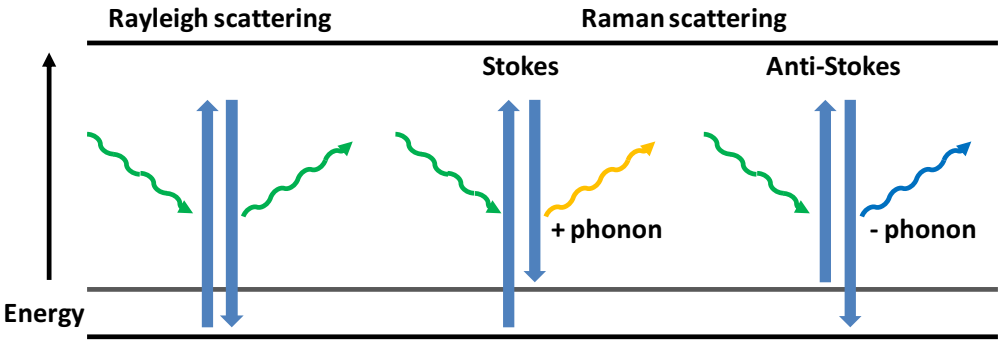

Figure 1.3. Schematic of the physical process in light scattering, including Rayleigh and Raman scattering.

Examples of Raman spectra are shown in Figure 1.4. Figure 1.4a shows spectra of kesterite compounds of different composition (selenium or sulfur) and crystalline quality. Note that the main peak is found at 197 cm^{-1} for CZTSe, and 337 cm^{-1} for CZTS. In the nanocrystalline CZTS thin, the Raman peaks becomes much broader (compare the two bottom spectra for CZTS). An additional Raman scattering phenomena of great interest is pre-resonant Raman scattering. Pre-resonant Raman scattering leads to a strong enhancement of the Raman signal, and is sometimes, but not always, achieved when the excitation source is closely matched to a fundamental energy value in the material such as the bandgap. Figure 1.4b shows Raman scattering spectra of ZnS measured under 514 and 325 nm (pre-resonant) excitation conditions. In the first case normal Raman scattering occurs with a main peak at 348 cm^{-1}. With 325 nm excitation ZnS is in pre-resonant conditions, and the signal is greatly enhanced, so that even second (697 cm^{-1}) and third order (1045 cm^{-1}) resonance of the main peak are visible. This enhancement is especially useful in cases which the phase is present in small quantities as a secondary phase, as seen in subsequent sections. It is important to note that the acquisition times between the two spectra is 2-3 orders of magnitude lower in the pre-resonant case.

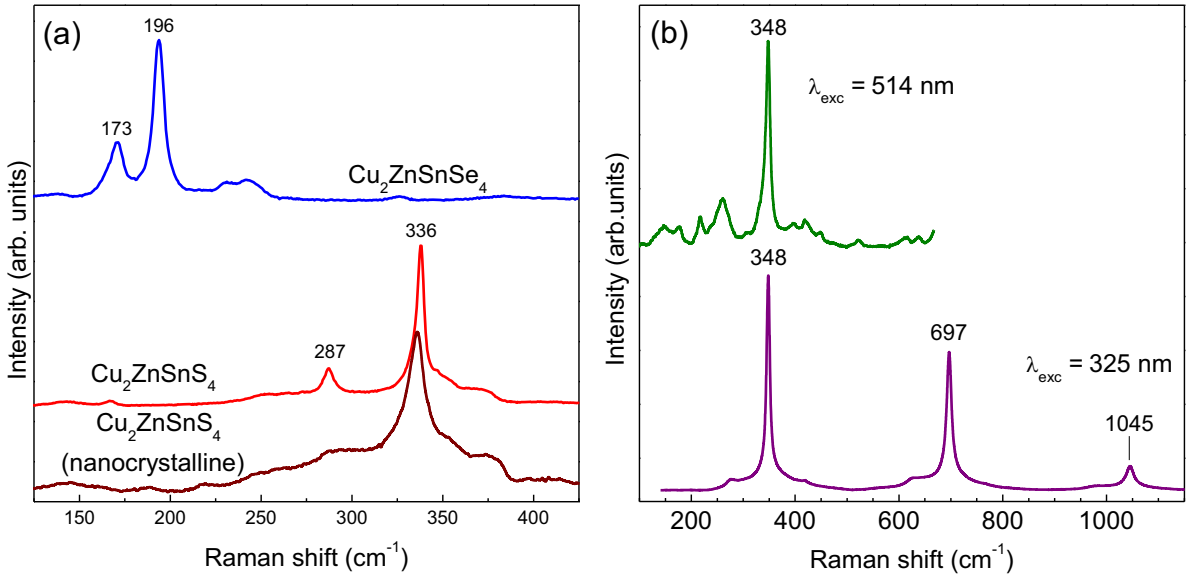

Figure 1.4. Raman scattering spectra of CZTSe and CZTS, including nanocrystalline CZTS (i.e. low crystalline quality) (a), and Raman spectra of ZnS powder with 514 nm excitation ((b) top spectra), and 325 nm excitation ((b) bottom spectra); note that measurement acquisition times when using 325 nm excitation are 2-3 orders of magnitude shorter when compared with 514 nm excitation.[15]

1.5 Objectives of this thesis

The main objective of the thesis is to further develop a two-stage process for the preparation of high efficiency $Cu_2ZnSn(S,Se)_4$ thin film solar cells. In view of this goal, some of the specific objectives of this thesis include:

- Study and optimization of metallic precursor film deposition by DC-magnetron sputtering, including minimization of surface roughness, ideal stack order, thickness, and compositional ratios
- Optimization of thermal processes for forming CZTS, CZTSe, and CZTSSe thin films from metallic precursors, including understanding of phase formation and reaction mechanisms
- Preparation of solar cell devices from CZTSSe thin films, including development of etching processes for secondary phases
- Characterization and testing of CZTSSe thin films and CZTSSe-based solar cells, including with Raman scattering spectroscopy, x-ray diffraction, scanning electron microscopy, x-ray fluorescence spectroscopy, etc.

2. Cu-Zn-Sn-S(Se) material system

Of course CZTS and CZTSe are not the only phases which may form in the Cu-Zn-Sn-S(Se) material systems, as secondary phases may form in any multi-element material systems. This is particularly true for CZTSSe, in which the highest performance devices are formed under nonstoichiometric compositions.[16–18] CZTSSe of photovoltaic grade is formed under Cu-poor and Zn-rich conditions: Cu/(Zn+Sn) = 0.7-0.9 and Zn/Sn = 1.1-1.3. The phase stability region of CZTSSe is much smaller than CIGSe, which increases the chances of secondary phase formation, especially ZnS(Se).[19,20] This chapter is about the different phases in this material system, and concludes with the publication "ZnS grain size effects on near-resonant Raman scattering: Optical non-destructive grain size estimation".

2.1 Cu-Zn-Sn-S(Se) phase diagram

The phase diagram of Cu-Zn-Sn-S has only been studied extensively by Olekseyuk et al.[21] Figure 2.1a shows the pseudo-ternary phase diagram of Cu_2S-ZnS-SnS, and Figure 2.1b shows the middle section at higher amplification along with expected secondary phases for a given composition (note that the Zn and Sn axes are swapped between (a) and (b)). In addition to CZTS, binary sulfides and ternary Cu-Sn-S phases may form. Given the non-stoichiometric compositions of the highest efficiency devices (Cu-poor and Zn-rich), ZnS is the most expected secondary phase (Figure 2.1b). Similar phase behavior is expected for the Cu-Zn-Sn-Se system, though to date no similar studies exist. In the five element Cu-Zn-Sn-S-Se system even less is known about phase formation, though there is evidence to suggest that sulfur-containing binaries would form preferentially over selenium-containing binaries because of lower free energy of formation.[22]

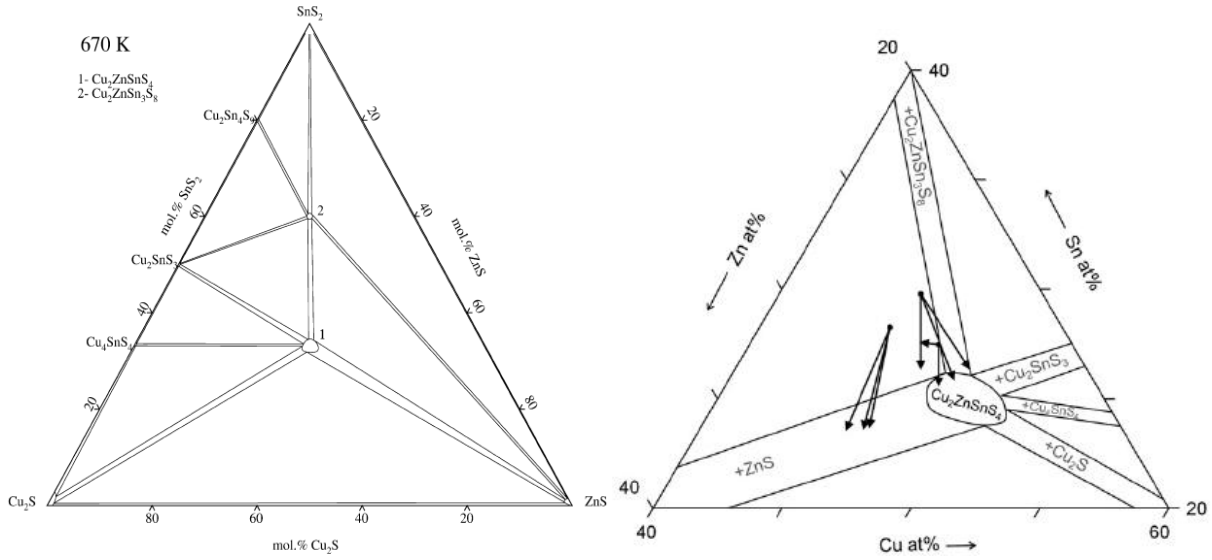

Figure 2.1 Psuedo-ternary phase diagram of Cu_2S-ZnS-SnS_2 (a),[21] note that compound 2 ($Cu_2ZnSn_3S_8$) has not been detected in other works, though this projection is taken at approximately 400 °C; (b) shows a zoomed view of the center showing expected secondary phases for different compositions,[20] note that the Zn(S) and Sn(S) axes are swapped between the two figures.

The presence of secondary phases is generally regarded as undesirable in CZTSSe-based devices. Secondary phases may act as recombination centers for charge carriers by creation of additional interfaces in the PV device. Lower bandgap phases may reduce the maximum open circuit voltage of the solar cell (i.e. $Cu_2SnS(Se)_3$),[23] and highly resistive (ZnS(Se))[24,25] or conductive phases ($Cu_xS(Se)$) could also reduce device performance. This presents a serious challenge for development of CZTSSe as a light absorbing layer, because of the aforementioned Cu-poor and Zn-rich conditions used in higher efficiency device fabrication. Thus strategies to minimize secondary phase formation or reduce its impact on final device properties, including posterior removal, are important.

2.2 Phase identification

Not only does the presence of secondary phases pose challenge for CZTSSe, so does the detection and identification of these phases. This can be difficult because of overlap in the principle x-ray diffraction (XRD) peaks, as an example illustrates in Figure 2.2a for $Cu_2ZnSnSe_4$, ZnSe, and Cu_2SnSe_3 (CTSe) (the same issue occurs in the sulfur system). In order to surpass this shortcoming, Raman scattering spectroscopy has proven to be a nearly indispensible tool. Figure 2.2b shows Raman spectra for these same phases, where more unique signatures are found for each compound, though still with some

overlapping. If a phase is present in small quantities, normal Raman scattering may not be sufficient to detect it. In this case pre-resonant Raman scattering can be employed to enhance phase detection, as seen in Figure 2.2c for the ZnSe phase under 458 nm excitation conditions (and Figure 1.4b for ZnS under 325 nm excitation). Under these excitation conditions Raman scattering of ZnSe is in pre-resonant conditions,[26,27] and measuring times are greatly reduced compared to, for example, 532 nm measurement conditions. Figure 2.3 contains Raman spectra from standard samples of some of the common phases in the Cu-Zn-Sn-Se (Figure 2.3a) and Cu-Zn-Sn-S (Figure 2.3b) material system.

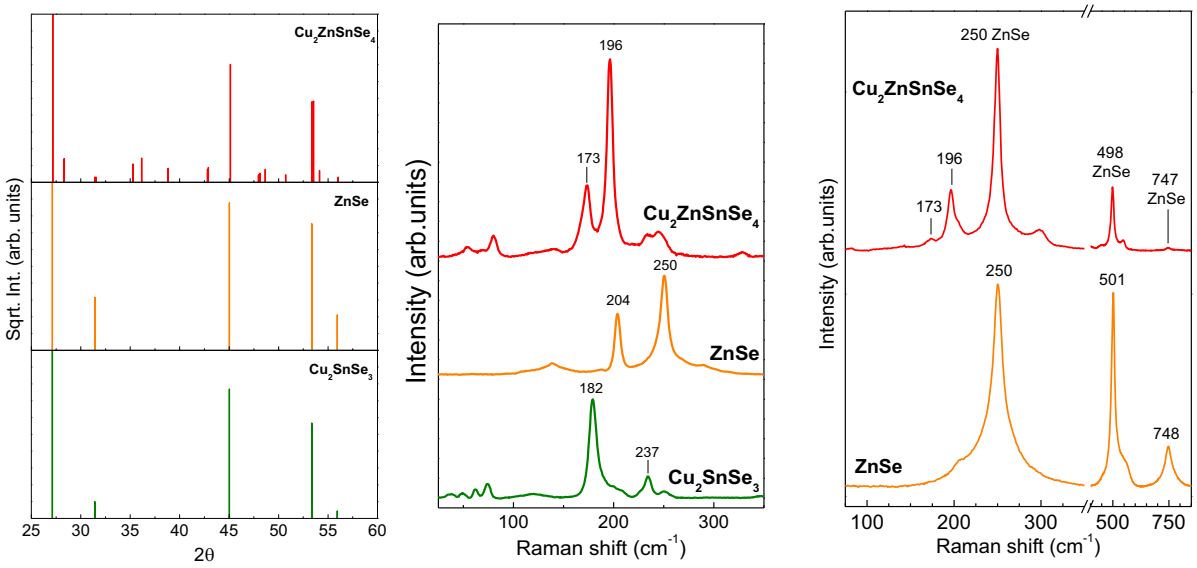

Figure 2.2. XRD reference patterns (a) and Raman scattering spectra (b,c) of CZTSe, ZnSe, and CTSe, showing the limitations of the former technique, and advantages of Raman, especially with pre-resonant scattering (c).

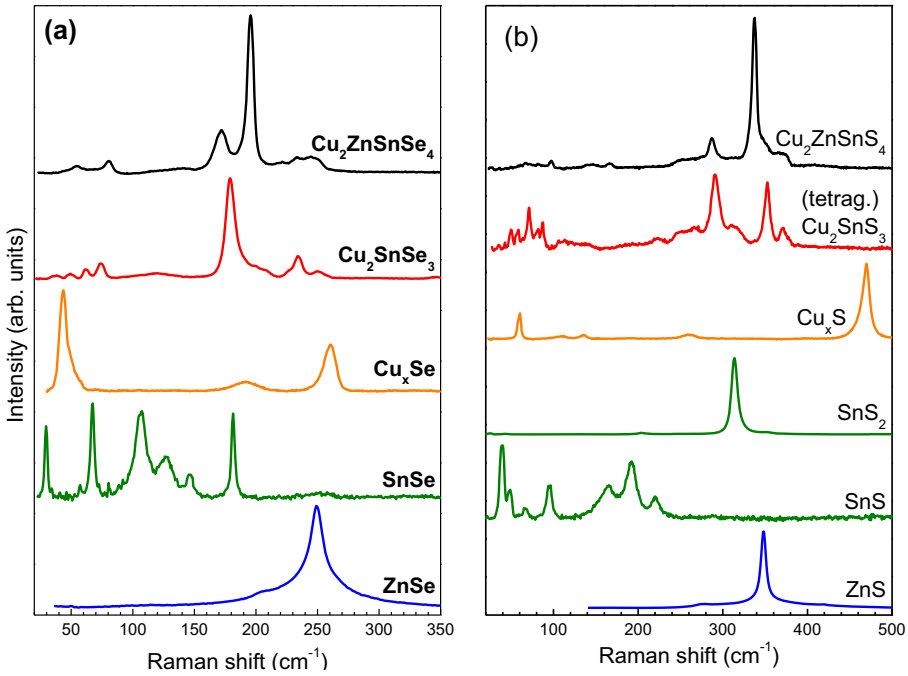

Figure 2.3. Raman spectra of some common phases in the Cu-Zn-Sn-Se (a) and Cu-Zn-Sn-S (b) material systems (modified from reference [28])

2.3 "ZnS grain size effects on near-resonant Raman scattering: Optical non-destructive grain size estimation"

This publication which is attached in the Appendix is accepted and in press in *CrystEngComm*. It is about the near-resonant Raman scattering characterization of ZnS nanoparticles and thin films. As seen in the previous sections, ZnS is one of the main expected secondary phases in the CZTS and CZTSSe material systems. This work correlates pre-resonant (325 nm) Raman spectral features, namely the intensity of the first, second, and third order main peaks, with the ZnS grain size. The cause of this variation is a change in the optical bandgap of the material due to phonon confinement, which leads to preferential enhancement of the different modes, depending on the energy of the photoluminescence emission (corresponding to bandgap). The final part of the paper is an application of the developed methodology on CZTS thin films with varying amounts of ZnS on the surface of the films. The graphical abstract submitted with this manuscript is shown in Figure 2.4.

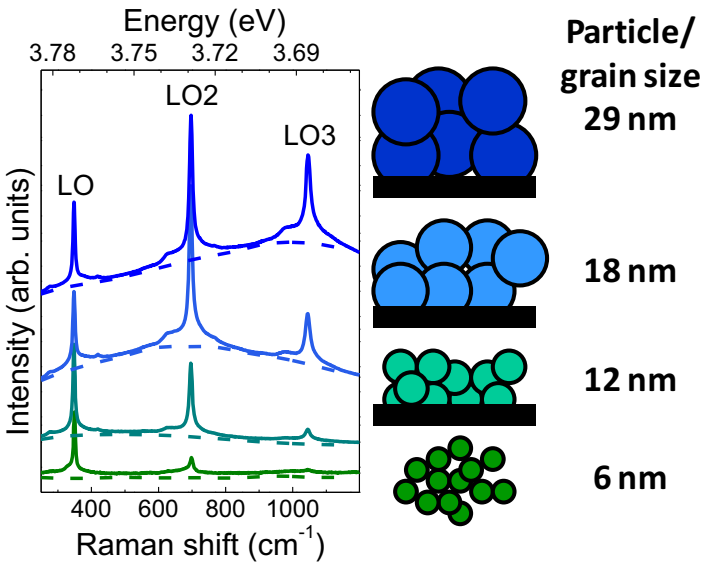

Figure 2.4. Graphical abstract for "ZnS grain size effects on near-resonant Raman scattering: Optical non-destructive grain size estimation", illustrating how increasing ZnS particle or grain size correlates with changes in the near-resonant Raman scattering spectra.

3. Properties of kesterite compounds

This chapter is about various characteristics of CZTSSe, including structural, optical, and electronic properties. The combination of ideal properties makes it a strong candidate to replace CIGSe as an absorber layer in thin film PV devices. Part of this chapter is based on the papers "Compositional dependence of chemical and electrical properties in Cu_2ZnSnS_4 thin films" and "Impact of electronic defects on the Raman spectra from electrodeposited $Cu(In,Ga)Se_2$ solar cells: Application for non-destructive defect assessment". The first is under preparation for submission, and the later is published in *Applied Physics Letters* (DOI: 10.1063/1.4793418). The first paper examines compositional dependence of the electrical properties in CZTS thin films. The second is a study correlating defect properties (type and density) with Raman spectral features of CIGSe films. The remainder of the chapter is a preliminary extension of the ideas in the latter paper to the CZTSe compound, the defect structure of which is understood much less than CIGSe.

3.1 Structural, optical, and electrical properties

CZTSSe crystallizes in the kesterite structure which is a derivative of the chalcopyrite (CIGS) structure, which itself is a derivative of the zincblende or sphalerite (ZnS) structure.[29–32] Chalcopyrites and kesterites have a unit cell that is twice as long in which Cu^+, $In^{3+}(Ga^{3+})$, Zn^{2+}, or Sn^{4+} replace the Zn^{2+} ions in adjacent positions, as illustrated in Figure 3.1. Until recently there was some controversy as to whether CZTSSe crystallizes in the stannite or kesterite structure.[19,30] Both structure are quite similar, except for the positioning of the Cu^+ and Zn^{2+} cations. Numerous theoretical and experimental results now point to kesterite as the lowest energy equilibrium structure of both CZTS and CZTSe. Nonetheless, stannite may still persist as a secondary structure in kesterite CZTSSe. In addition to stannite, disordered kesterite[33] and wurtzite[34,35] crystal structures have been reported for CZTSSe. Considerable work is still left to be done to understand the defect structure of CZTSSe, especially considering the non-stoichiometric compositions used in film growth (discussed in the following sections).

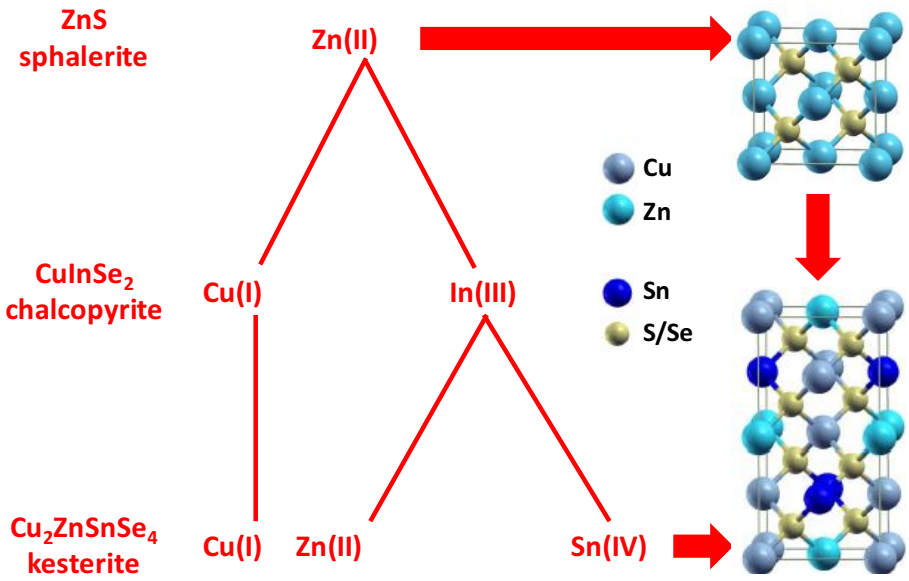

Figure 3.1. Derivation of the CZTSe crystal structure from ZnS.[29]

CZTSSe has a direct bandgap, the value of which varies depending on the anion composition. As such, it can range from about 1.0 eV in CZTSe up to 1.5 eV in CZTS.[14,27,36] Cation substitution in kesterites is also being explored to modify this energy, for example, with Cd in place of Zn,[37] and Ge or Si in place of Sn.[38] The absorption coefficient of CZTSSe has been measured to be greater than 10^{-4} cm^{-1} in the visible range,[39] which, along with its direct bandgap energy, make it ideal as a light absorbing material in thin film PV. Defect type and density play an integral role in the optical and electronic properties of semiconducting compounds. The main p-type defects expected in CZTSSe – because of their low formation energy – include V_{Cu} and Cu_{Zn}.[19,36,40,41] This is based mostly on theoretical calculations, and of stoichiometric CZTSSe, rather than Cu-poor and Zn-rich compounds. Interestingly, the Zn_{Cu} point defect, which may be expected because of theZn-rich compositions, is actually an n-type defect. The formation of [Cu_{Zn}+Zn_{Cu}] defect clusters has been proposed as a cause for lower than expected V_{OC}.[36,42] Experimental work is still somewhat scarce in this matter, though it is of high importance. Nonetheless, it is clear that CZTSSe, similar to CIGSe, exhibits p-type conductivity because of the formation of p-type defects. The conductivity of CZTSSe has been found in the range of 10^{0}-10^{-1} Ωcm,[39] and is dependent on both cation[43] and anion[44] ratios.

3.2 Compositional dependence of electronic properties

This section contains portions of a publication currently being written and tentatively titled "Compositional dependence of chemical and electrical properties in Cu_2ZnSnS_4 thin films". CZTS films of varying composition were prepared by DC-magnetron sputtering deposition using the parameters presented in references [14,24]. The range of compositions includes Cu/(Zn+Sn) = 0.61-0.89 and Zn/Sn = 1.10-1.43, which include compositions used for device-grade CZTS films. Annealed films were etched in HCl in order to remove superficial ZnS phases, a procedure presented in reference [24]. Composition measurements were made by x-ray fluorescence spectroscopy and electrical conductivity was measured as a function of temperature (10-430 K) using the van der Pauw method.

The cation composition of the precursor, annealed, and etched films is shown in Figure 3.2a. In general the samples become more Zn-rich with annealing, an effect attributed to Sn-loss.[10,11] Most notably though is the composition after etching which falls on a line of constant Cu/Zn, this is seen more clearly with the cation ratios, shown in Figure 3.2b. This seems to indicate that after a certain amount of Zn is incorporated into the CZTS films, the Zn-excess tends to accumulate on the surface of the films. This is why the Cu/Zn ratios are constant after etching, and vary within the small range of 1.84-1.92. On the other hand, Cu/Sn ratios vary greatly from 1.57-2.12. While this may be attributable to the presence of secondary phases (Sn-S), none are detected on the surface by Raman scattering spectroscopy. Thus, this may be a result of the multivalent nature of Sn, i.e. from Sn^{4+} to Sn^{2+}.[45] This possibility may arise with the formation of Sn_{Cu} or Sn_{Zn} anti-site defects, and are expected to have an effect on the electrical properties of the films.

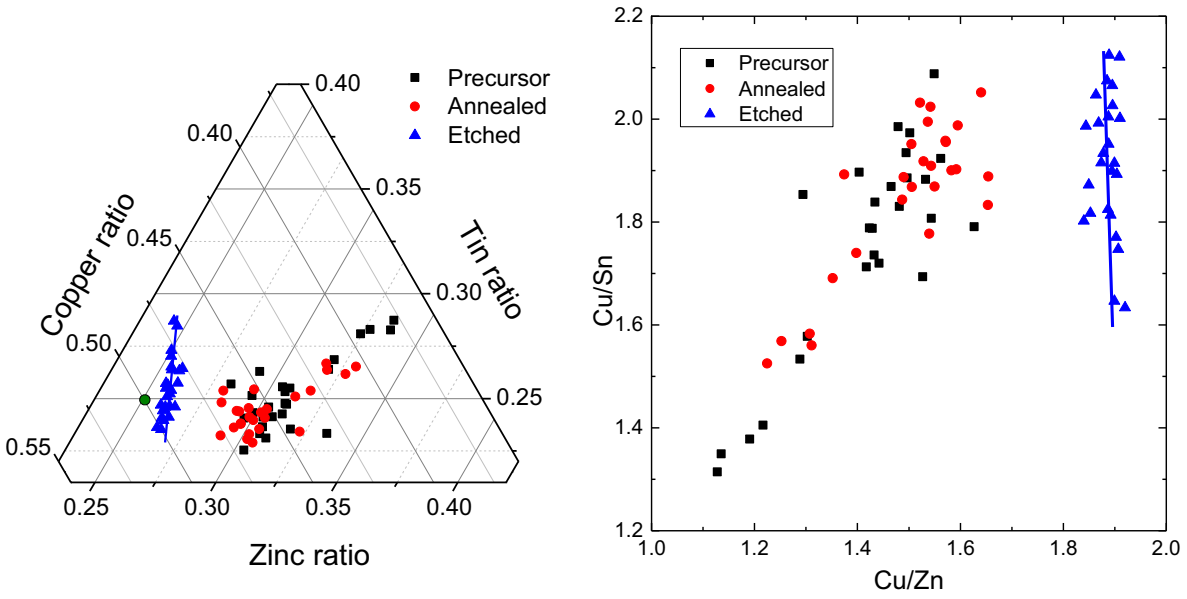

Figure 3.2. Psuedo-ternary phase diagram of Cu-Zn-Sn (a) for precursor metallic stack, as-grown, and etched CZTS films; the stoichiometric composition for CZTS is indicated by a green dot; Cu/Zn versus Cu/Sn ratio for the CZTS films (b), while there is a relatively large spread for precursor and annealed compositions, after etching there is a tendency towards nearly constant Cu/Zn, and a range of Cu/Sn.

Electrical measurements were made on a series of samples with varying Cu/Sn ratio (1.57-1.88) to determine differences in electrical conductivity, shown in Figure 3.3a. As the Cu/Sn ratio increases, so does the conductivity, from 2.2 up to 16.0 $m\Omega^{-1}cm^{-1}$ (resistivity 450 to 63 Ωcm). The resistivities are much higher than other reported values,[39,43] and may be non-ideal for a solar cell device, but a posterior heating procedure reduces the resistivity by two orders of magnitude. The results of the posterior heating are not shown here, as the work is preliminary and still ongoing. The activation energy of different charge carrier processes is strongly depending on this ratio. The two main processes are grain boundary (GB) conduction and nearest neighbor hopping (NNH), and activation energies, shown in Figure 3.3b, are proportional to the slope of the conduction curves in Arrhenius plots. GB barrier energy is found through a linear fit of the high temperature data points, and NNH activation energy is calculated by fitting the lower temperature data points. Both energies increase as the samples become more Cu-poor. There are no Cu-rich samples with which to compare, but it appears that while Cu-poor conditions are necessary to fabricate device-grade CZTS films, it should not be too far from stoichiometry because of the increase in charge carrier activation energies.

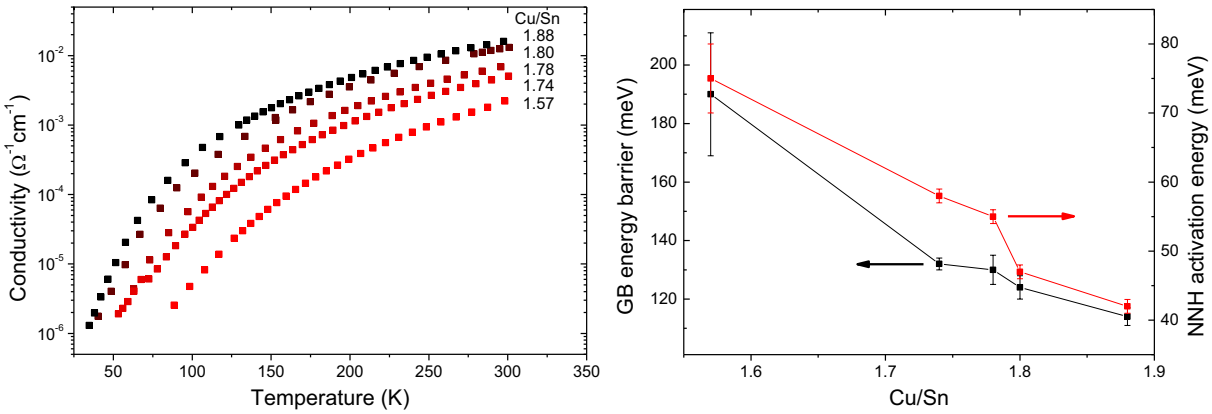

Figure 3.3. Temperature dependent conductivity of CZTS films with varying etched Cu/Sn ratios (a), and activiation energies of different charge carrier processes (b).

3.3 "Impact of electronic defects on the Raman spectra from electrodeposited Cu(In,Ga)Se_2 solar cells: Application for non-destructive defect assessment"[46]

This paper, found in the Appendix, is submitted in requirement for the Doctor of Philosophy in Engineering and Advanced Technologies at the University of Barcelona. The paper is based on the electrical and Raman scattering characterization of CIGSe thin films with varying densities of defects. Copper and selenium related point defects and their density were measured by admittance spectroscopy, and these values were correlated to changes in the Raman spectral features. The results show the potential of Raman scattering for optical and non-destructive detection of electronic defects which may potentially impact the performance of the solar cell devices. This is a great advantage because admittance measurements typically require sample destruction (isolation and contacting) and are slow compared to Raman spectroscopy. In the following section a preliminary extension of these results is made to understand Raman spectra of CZTSSe.

3.4 Defect analysis in Raman spectra

The defect structure of CZTSSe is not as well understood as in CIGSe, which is an impediment to the application of a similar study presented in section 3.3 to the kesterite material system. Nonetheless, there is some preliminary work along these lines which should eventually open the possibility of such an extension in the future. The first of these is based on samples prepared in [14], where Cu-Zn-Sn stacks were annealed at 550 °C for various times. The result was CZTS films of varying crystalline quality and grain size, as seen in Figure 3.4. The average grain size increases from hundreds of nanometers at 0 minutes to greater than 2 µm for the film annealed 120 minutes.

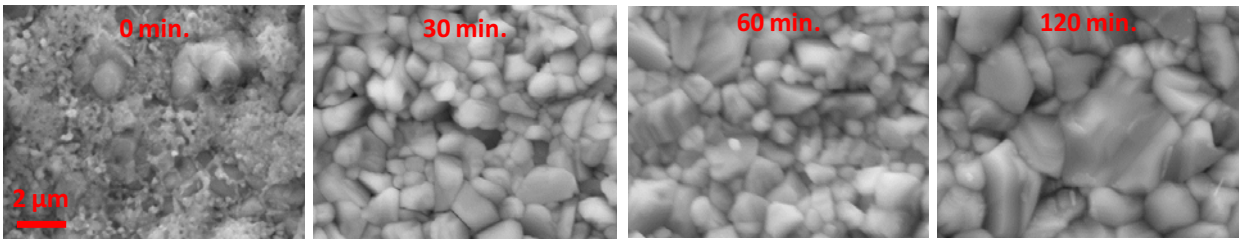

Figure 3.4. Surface SEM images of CZTS films annealed at different times, showing variations in average grain size.[47]

In Figure 3.5 Raman spectra of each film made with 532 nm excitation are shown, centered on the main A1 peak. These spectra are ordered top to bottom by annealing time, and consequently grain size. There is a clear shift and broadening of the main CZTS peak with the lower grain size films. The broadening is also asymmetric, tending towards lower Raman shift. The cause of this broadening is attributed to both strain and phonon confinement effects.[47] These results are particularly relevant because they relate microstructural information via fast and non-destructive Raman measurements. Understanding the influence of microstructure on the Raman spectra is a major step to furthering the application of Raman-based methodologies to CZTS (and CZTSe, CZTSSe).

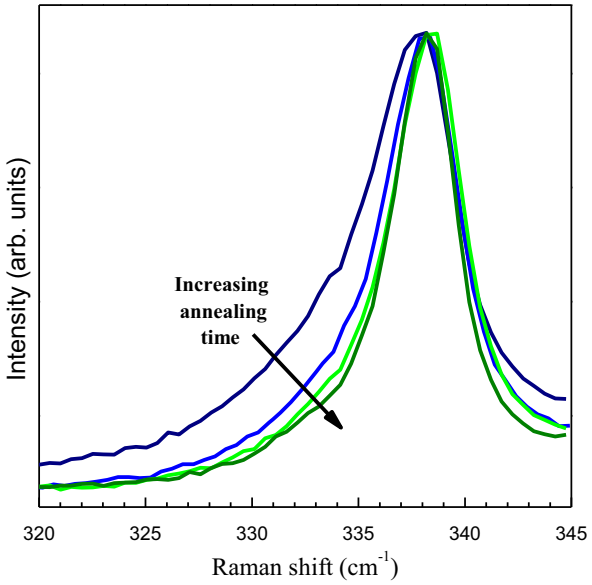

Figure 3.5. Raman spectra of CZTS films annealing different times zoomed on the main A1 peak.[47]

In addition to phonon confinement effects in Raman spectra, point defects are also expected to influence them. Point defects such as V_{Cu} and Cu_{Zn} are the most expected defects in CZTSSe of PV-grade (Cu-poor and Zn-rich).[36] The density and kind of defects are expected to vary with the film composition. For example, while increasing the Cu/(Zn+Sn) ratio one would expect fewer V_{Cu} to form, and perhaps more Cu_{Zn} point defects. Most compositional studies focus on sets of samples, with a range of compositions, but because of the "piece-by-piece" nature of such studies, the range and variations must be limited. To overcome this limitation a compositionally graded CZTSe film was made. The precursor film was prepared with the same conditions presented in other works.[25,27] However, to form the gradient composition the substrate was not rotated during precursor deposition. Because of the off-center position of the three metallic targets, areas of higher or lower metal content are formed, depending on the relative position from the targets. From the graded precursor film, a 5x5 cm^2 sample was cut and selenized, resulting in a smoothly graded range of compositions from Cu/(Zn+Sn) = 0.60-1.00 and Zn/Sn = 1.00-2.50. This is an especially interesting range because it falls within the Cu-poor and Zn-rich compositions used for the highest efficiency devices, and even goes beyond them to attain an even greater range of compositions. A 14x15 grid of 3x3 mm^2 squares was scribed in the film to delineate different compositional regions, and then composition was measured using x-ray fluorescence spectroscopy at the center of each square. The resulting compositional ratios (Cu/(Zn+Sn) and Zn/Sn) are shown in Figure 3.6.

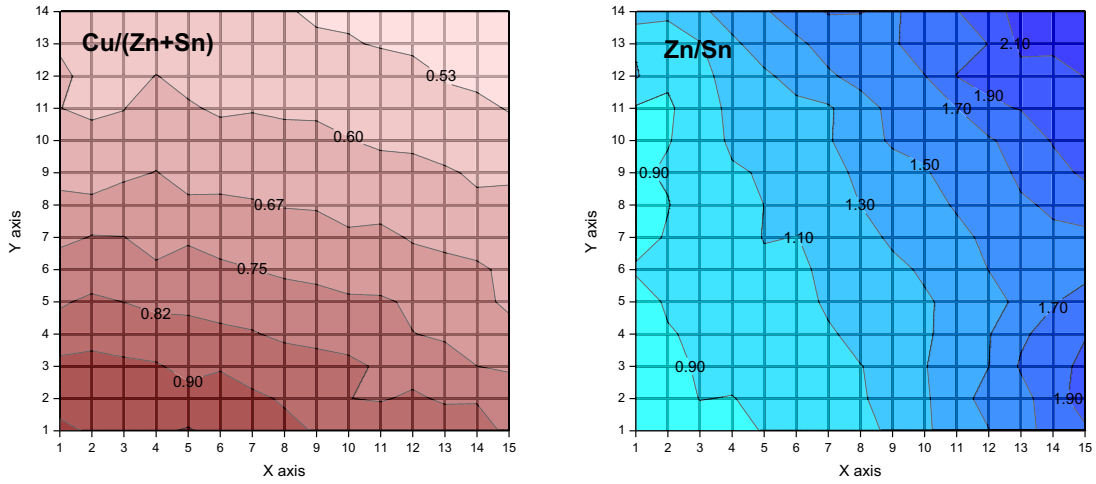

Figure 3.6. Mapping of cation compositional ratios Cu/(Zn+Sn) and Zn/Sn in a compositionally graded CZTSe film.

Next Raman scattering measurements were made at the center of each square using green (532 nm) excitation conditions. Four sample spectra are shown in Figure 3.7a. The main CZTS peak (197 cm^{-1}) is notably broader under increasingly Cu-poor compositions, and changes in peak shape around 173 cm^{-1} are even more notable. Additionally, in the higher Raman shift range (230-250 cm^{-1}) there are also changes in peak shape. Taking "iso-compositional" lines and comparing the features seen in Raman spectra yields particularly interesting results. In Figure 3.7b peak ratios and full-width-at-half-max (FWHM) of an "iso-composition" of Zn/Sn = 1.10 are shown. As the Cu/(Zn+Sn) ratio increases the intensity ratios of the A1 and A2 peaks increases from 0.40 to 0.57. In the same range FWHM decreases from 15.2 to 6.1 cm^{-1} (A2) and 4.9 to 3.3 cm^{-1} (A1). It should be noted that the A2 region is actually an overlapping of multiple peaks, which explains why the FWHM varies much more than for the A1 peak. This indicates that Cu-excess improves the crystalline quality of the films. A study of the defect types and their density is ongoing for similar samples, and here one may only speculate that the compositional deviations shown here are the source of variations in the Raman scattering spectra.

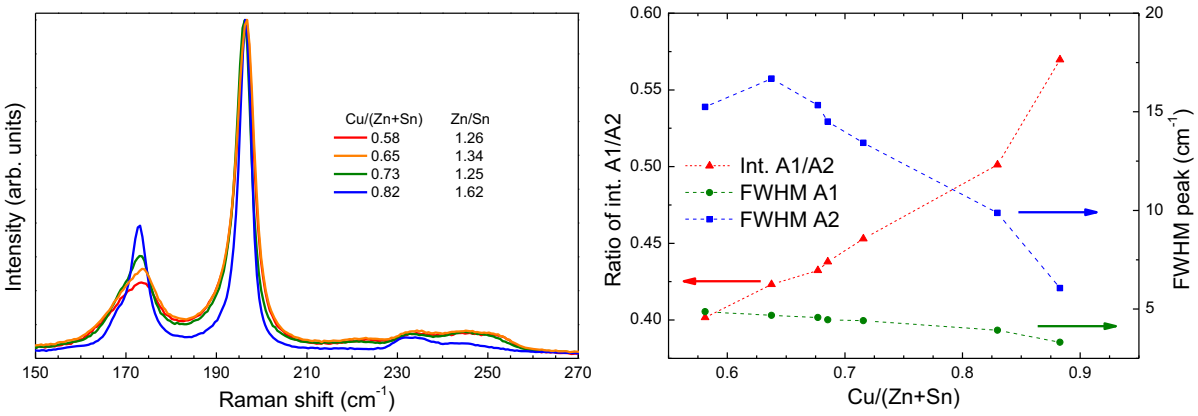

Figure 3.7. Four sample spectra from the compositionally graded CZTSe film (a); ratio of the main CZTSe peaks (A1/A2) and FWHM of each with respect to Cu/(Zn+Sn) ratio (in a line of constant composition, Zn/Sn = 1.10) (b).

4. $Cu_2ZnSn(S,Se)_4$ deposition and thermal processing

CZTSSe thin films can be deposited by a wide array of techniques, including physical vapor deposition (PVD - sputtering, evaporation, pulsed laser), chemical vapor deposition (CVD), chemical deposition (electroplating, slurry) and printing (nanoparticles). Typically the highest efficiency chalcogenide-based devices are prepared by PVD because it affords greater compositional and morphological control than non-vacuum methods. For example, the highest efficiency CIGSe device (20.8%)[6], CZTS (9.2%)[18], and CZTSe (9.2%)[17] based devices were prepared co-evaporation. A notable exception is the highest efficiency CZTSSe device (12.6%)[9] which was prepared by a hydrazine slurry deposition process. This chapter will focus first on the deposition of CZTSSe films by sputtering deposition, and then on the thermal processing of precursor films in order to chalcogenize (sulfurize/selenize) and recrystalize the precursor films. The majority of this chapter is based on four publications, three of which are already published or in press, and one which is under review.

4.1 Sputtering deposition

Physical vapor deposition is commonly divided into three main categories: sputtering, evaporation, and pulsed-laser deposition. These deposition processes share some similarities, the most fundamental of which is the use of a physical process – such as laser ablation or bombardment of energetic particles – to remove material from a target material and deposit in the vapor phase onto a substrate. This is in contrast to chemical vapor deposition, in which a precursor gas containing the elements to be deposited is reacted in the chamber, and subsequently deposited onto the substrate. Sputtering is the most commonly used PVD method for CZTSSe films,[13,24,25,27] followed by evaporation,[12,17,48] and finally pulsed-laser deposition[49] which is the least commonly employed. Sputtering deposition is the main technique employed in the works presented in this thesis, and functions by bombarding a target with energetic particles (from a plasma, typically Ar). A schematic of this process is shown in Figure 4.1. PVD methods are used for the highest efficiency CIGSe (20.8%)[6], CZTS,[18] and CZTSe[17] devices. However, the highest efficiency CZTSSe based device is produced by hydrazine solution processing (12.6%)[9]. PVD is an industrially important technique which has been regularly used in the microelectronic industry for decades. This is because of high material usage rate, good step coverage, and process control. The highest efficiency CIGSe devices have carefully controlled In-Ga gradients in order to optimize photon absorption and charge carrier separation, which is much easier to control in PVD processes.

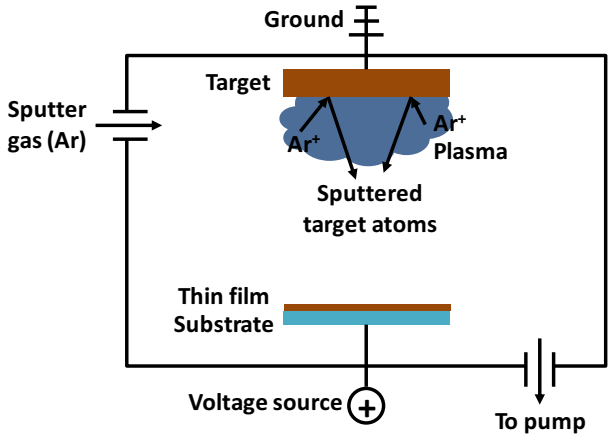

Figure 4.1 Schematic of sputtering deposition chamber, Ar^+ ions are generated in the plasma and eject atoms from the target material, which then condense onto the substrate to form a thin film.

Target materials used for PVD may be metallic or non-metallic.[17,24,27,48,50] Metal deposition is more simple from a technological point of view, and knowledge gained from such processes is somewhat transferable to other thin film metal deposition processes like electroplating.[51] The majority of the work presented in this thesis uses metallic precursor films deposited by DC-magnetron sputtering deposition.[14,15,24,27,52] However, vertical compositional gradient control is more difficult, and Zn is more readily lost in its metallic form due to its low vapor pressure. Deposition of sulfide and selenide compounds is more complex, and more expensive, but has produced the highest efficiency CZTS and CZTSe devices to date. From a developmental point of view, it is also easy to attain a better understand of the thermal treatments in a PVD metal precursor process of CZTSSe and later apply it to non-vacuum methods such as electroplating.

4.2 Thermal processing

Regardless of the deposition method used for CZTSSe films, a high temperature thermal processing step is utilized almost universally. In the case of metallic precursors, it is necessary to "chalcogenize" the film and form the desired kesterite compound. It is also necessary to crystallize the films, which is necessary for deposition processes performed at relatively low temperatures. The range of temperatures used varies from about 400 °C up to 600 °C. High temperatures are desirable to improve the crystalline quality of the films,[13,50] however, low temperatures may also be of interest because of the loss of volatile elements. Figure 4.2 shows the vapor pressure of the most volatile components of the CZTSSe

system in order of decreasing vapor pressure: sulfur, selenium, zinc, tin selenide, and tin sulfide. If loss of a certain element is too high, it may seriously affect final film composition and properties.

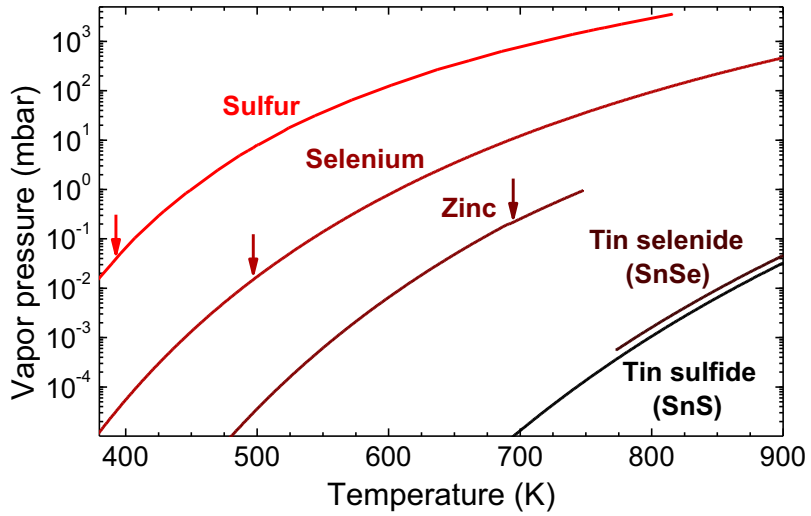

Figure 4.2. Vapor pressure of the most volatile elements and compounds in the CZTSSe system, arrows mark the melting point of each phase.[53–57]

Additional concerns during thermal processing arise from the occurrence of at least two detrimental reactions. The first is decomposition of CZTSSe at the surface, and volatilization of low-vapor pressure Sn-S(Se) compounds.[10,11] Because of this the thermal treatment atmosphere is often charged with Sn in order to suppress elemental loss by this means. The second reaction of note occurs in the region of the conventionally employed Mo back contact. $MoS(Se)_2$ is formed in preference of CZTSSe, leaving binary copper, zinc, and tin compounds in this area.[12,13,22] A schematic of these two reactions in the case of CZTS is shown in Figure 4.3, and both are treated in more detail in following sections.

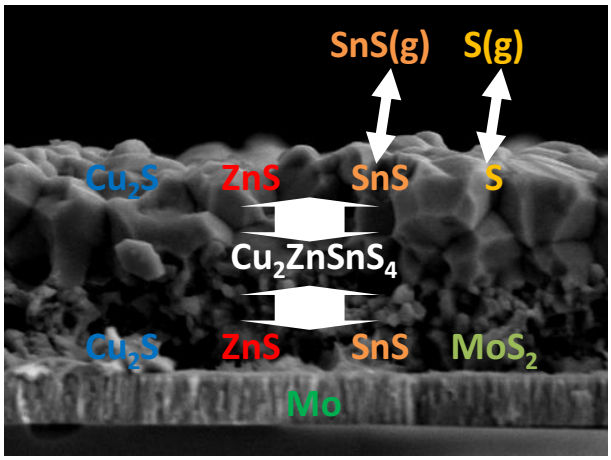

Figure 4.3. Schema of detrimental reactions in CZTS thin films during high temperature processing; on the surface is the decomposition of CZTS and evaporation of sublimation of SnS and S, and on the back region is the decomposition of CZTS to form MoS_2 and other binary sulfides.

4.3 "Secondary phase formation in Zn-rich $Cu_2ZnSnSe_4$-based solar cells annealed in low pressure and temperature conditions"[27]

This is the third article submitted for the Doctor of Philosophy in Engineering and Advanced Technologies at the University of Barcelona, and was published in *Progress in Photovoltaics: Research and Applications* (DOI: 10.1002/pip.2473). In this paper the effect of annealing temperature and precursor Zn-excess on secondary phase formation and accumulation is detailed. ZnSe is the main secondary phase, and increasing annealing temperature and Zn-excess promotes its accumulation in the back contact region, where it is especially detrimental to device performance. The highest performing device was prepared under low temperature and Zn-excess conditions, resulting in a 4.8% efficiency. The full paper is found in the Appendix.

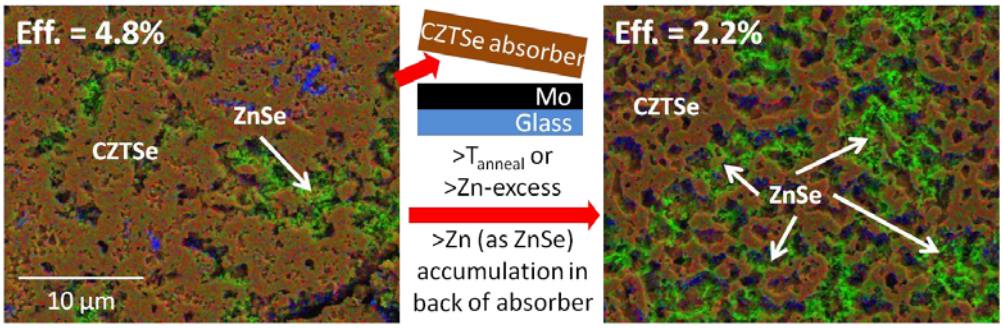

Figure 4.5. Graphical abstract for the article "Secondary phase formation in Zn-rich $Cu_2ZnSnSe_4$-based solar cells annealed in low pressure and temperature conditions", illustrating how the accumulation of ZnSe is influences by processing temperature and precursor Zn-excess.

4.4 "Single-step sulfo-selenization method to synthesize $Cu_2ZnSn(S_ySe_{1-y})_4$ absorbers from metallic stack precursors"[52]

This is the fourth article submitted to complete the graduation requirements for the Doctor of Philosophy in Engineering and Advanced Technologies at the University of Barcelona, and was published in *ChemPhysChem* (DOI: 10.1002/cphc.201300157). Found in the Appendix, it details the development of a process to simultaneously sulfurize and selenize ("sulfo-selenization") metallic precursors to form CZTSSe films. This is an especially unique work because to date sulfur-selenium kesterites are formed from non-metallic precursors, or from solution and nanoparticle synthesis. By tailoring the thermal processing conditions, including temperature, chalcogen source, and pressure, a range of S/(S+Se) compositions from very selenium-rich to very sulfur-rich is attained. The best performing device in this study is 4.4%.

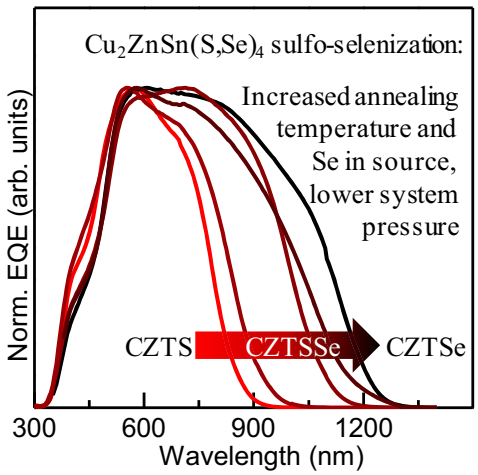

Figure 4.7. Graphical abstract of "Single-step sulfo-selenization method to synthesize $Cu_2ZnSn(S_ySe_{1-y})_4$ absorbers from metallic stack precursors", by modifying the process conditions CZTSSe films of varying S/(S+Se) content were synthesized from metallic precursors.

5. Kesterite-based devices

CZTSSe films form just one layer of the thin film PV device structure (Figure 1.1), and the function of the entire cell depends on the proper optimization of each layer. Perhaps the principle reason for the rapid improvement of CZTSSe-based devices (Table 5.1) has been the inheritance of an optimized device structure from CIGSe. The most commonly used device structure includes a Mo back contact, CdS buffer layer, and TCO front contact. It is becoming increasingly clear that while these materials may be adequate for CZTSSe, they are certainly not optimum. Further improvement of CZTSSe-based devices must optimize the front and back contact interfaces. While a detailed review of the other layers is beyond the scope of this thesis, this chapter will look at some of these factors. Here some front and back interface optimization strategies will be detailed. Part is based on a publication about removing secondary phases from the surface of CZTS and CZTSe films. The problems encountered include potentially non-optimal materials for proper band alignment, and also depend strongly on the deposition and processing parameters, for example, the presence of secondary phases in these regions. Of the highest efficiency CZTSSe-based devices shown in Table 5.1, many employ strategies to overcome issues with the front and back interfaces.

Table 5.1. Some of the highest efficiency CZTSSe, CZTS, and CZTSe devices which have been reported, including compositional ratios and deposition method.

Absorber	Eff. (%)	Cu/(Zn+Sn)	Zn/Sn	Method	Reference
CZTSSe	12.6	0.8	1.1	Hybrid sol-part.	[9]
CZTSSe	9.6	0.8	1.2	Hybrid sol-part.	[59]
CZTS	8.9	---	1.1	Co-sputter	[48]
CZTS	8.4	---	1.3	Co-evap.	[60]
CZTSe	9.2	0.9	1.2	Co-evap.	[17]
CZTSe	8.4	---	1.3	Co-evap.	[50]

5.1 Back interface optimization

In the back contact Mo typically reacts to form $MoS(Se)_2$ when processed at high temperatures. But rather than forming solely from excess sulfur or selenium in the atmosphere, there is evidence of a decomposition reaction in the proximity of Mo for both CZTS and CZTSe (section 4.2). $MoS(Se)_2$ has a lower enthalpy of formation than CZTS or CZTSe, so a decomposition occurs to form $MoS(Se)_2$, $Cu_2S(Se)$, ZnS(Se), and SnS(Se).[12,13,22] The presence of these secondary phases would likely act as recombination

centers for charge carrier, reducing device performance. This leaves the CZTSSe community with three main options:[12] 1. replace the Mo back contact for another, more stable compound 2. introduce barrier layers to reduce decomposition, and 3. modify processing to reduce the possibility for decomposition.[12] Very little work has been done finding a replacement for Mo (option 1), and in CZTSSe based devices it is the only back contact material with notable research results to date.

Concerning option 2, at least two different barrier layers have been investigated, including TiN and ZnO. Shin et al. and Scragg et all have used TiN in CZTS and CZTSe based devices,[48,50] showing that the barrier is effective and reducing the formation of $MoS(Se)_2$ and inhibiting CZTS(Se) decomposition in the vicinity of Mo. Lopez-Marino et al. shows ZnO to be an effective barrier for preventing decomposition of CZTSe, though ineffective at preventing selenization of the Mo back contact.[13] Finally, modifications of the thermal process (option 3) may also help prevent the decomposition of CZTSSe. It is important to note that decomposition is not readily observed by all researchers, and the various thermal processes may be a reason. An idea studied by Scragg et al. includes supplying an external sulfur source they show how the decomposition can be suppressed.[12,48]

5.2 Front interface optimization

CdS is the most commonly used buffer layer in CIGSe- and CZTSSe-based devices. In conjunction with the CZTSSe layer, the interface forms the p-n junction. Band alignment in the p-n junction is an important factor in device properties. Optimally there should be a perfect alignment between the absorber and buffer layer conduction band minimums. In reality, it is more commonly to encounter a higher buffer layer conduction band (“spike”) or lower conduction band (“cliff”). These two configurations are illustrated in Figure 5.1. In the case of a spike, photogenerated charge carriers encounter a barrier, and the series resistance of the device is increased. In the case of a cliff there is increased recombination of charge carriers at the interface, and the maximum open circuit voltage attainable is decreased. Of these two alignment types, cliff alignment is the most detrimental to device performance because it may potentially reduce open circuit voltage of the devices.

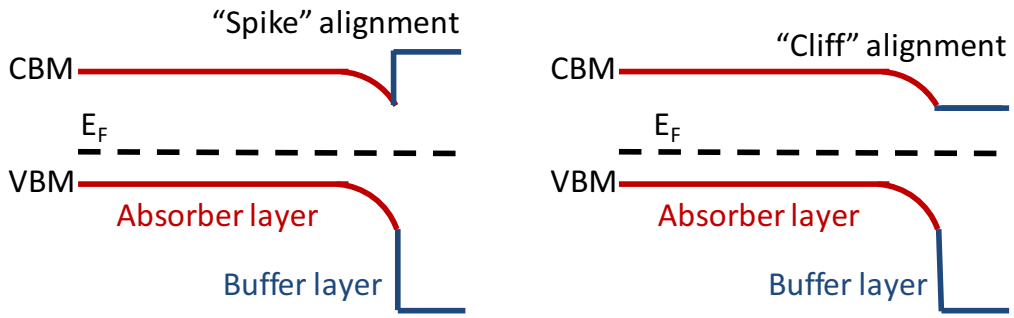

Figure 5.1. Band structure at the p-n junction in a CZTSSe solar cell device, showing different alignment possibilities, including "spike" (left) and "cliff" (right) offsets.

The alignment between CZTSSe and CdS is not yet clear, and there are conflicting theoretical and experimental results.[61–63] Also, the alignment may also be different for pure CZTS or CZTSe. CZTS devices have much lower than expected Voc, and one explanation for this is a cliff-type configuration. Additionally, the use of Cd is non-ideal, because it is a relatively rare element, and poses environmental hazards as a heavy metal. Some works have looked at alternative buffer layer materials such as ZnO and In_2S_3,[18,64] but with poorer results than CdS. Further compromising the junction quality is the presence of secondary phases on the surface. Many different phases have been detected on the surface of CZTSSe absorbers, including native oxide phases,[65] ZnS(Se)[24,25,66], and $Cu_XS(Se)$.[43] While the influence of these phases is only partially understood, they are expected to lower junction quality, and thus device performance.

5.3 "Development of a selective chemical etch to improve the conversion efficiency of Zn-rich Cu_2ZnSnS_4 solar cells"[24]

This is the final article used in completion of the requirements for the Doctor of Philosophy in Engineering and Advanced Technologies at the University of Barcelona, attached in the Appendix. ZnS is shown to be accumulated on the surface of the CZTS absorbers, and a HCl-based etch is used to selectively remove it. The removal of this phase leads to a massive increase in device efficiency, from 2.7 up to 5.2%, in part from the reduction in series resistance of the solar cell. The graphical abstract is shown in Figure 5.2. It should be noted that ZnSe is the most expected secondary phases in CZTSe films, and this etching procedure has been found to be relatively ineffective at removing it. Other work has been made to remove ZnSe, and is based on a two-step etching processing, first with potassium permanganate, and then sodium sulfide.[25]

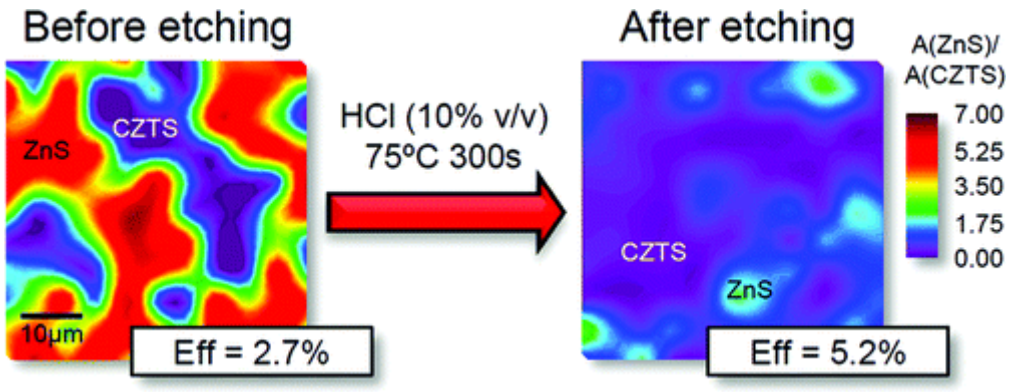

Figure 5.2. Abstract image for "Development of a selective chemical etch to improve the conversion efficiency of Zn-rich Cu_2ZnSnS_4 solar cells", it shows the non-homogeneous distribution of ZnS on a CZTS films, and how it is effectively removed with a HCl etch, leading to large increases in device efficiency.

6. Conclusions

The main of objective of this thesis was to deepen understanding of CZTS, CZTSe, and CZTSSe thin films and solar cell devices prepared by a two stage process, specially developed at IREC. This principally included studies about the processing of these materials, and how this influences the material properties and secondary phase formation of these systems, and finally the device performance. The results were shown in a series of articles which have been published or are under review. In the first of these ZnS nanoparticles and thin films were studied with UV Raman spectroscopy. The photoluminescence emission was shown to shift depending on grain size, thus preferentially enhancing first, second, or third order ZnS Raman peaks. By comparing the ratios of these peaks, it is possible to estimate the grain size in an optical and non-destructive way. This methodology was then applied to CZTS films with varying quantities of ZnS in order to estimate the thickness of this secondary phase on the films. Next, features in Raman spectra were correlated to defect density of CIGSe thin films. This is particularly interesting because defect analysis is typically a destructive process, and requires elaborate sample preparation, whereas Raman spectroscopy is a more rapid and non-destructive process. This idea was extended preliminarily to CZTS and CZTSe, which are still at early stages of development, so their defect structures are not widely understood.

The next four articles are focused on thermal processing of CZTS, CZTSe, and CZTSSe. In the first, the reaction mechanisms of CZTS from metallic precursors were studied, resulting in a process yielding CZTS-based devices of 5.5% efficiency. It elucidated the reaction mechanisms for the synthesis of CZTS, showing that the reaction proceeds first by the formation of inter-metallic compounds, and that the presence of (SnS-Cu_2S) solid solution is a key step for the formation of CZTS in a solid-liquid-gas reaction at temperatures higher than 480 °C. Also, it was shown that Zn-excess is segregated towards the back region as ZnS during the crystallization step. In the next two CZTSe is studied by CTP and RTP processes. By CTP the effect of annealing temperature and precursor Zn-excess are shown to affect secondary phase formation and distribution in the films, using a low-temperature/low-pressure process with the best performing device prepared under low temperature and Zn-excess conditions (4.8%). Further optimization of this process at IREC has resulted in an 8.2% efficiency device. In the RTP work precursor stack order is demonstrated to influence phase formation, distribution, and device performance, with a maximum of 4.3% in this first optimization of the process. For the RTP processes Zn loss is identified as a big challenge, due to the volatility of Zn, and that the stack order plays a major role in the synthesis of CZTSe. In the work on CZTSSe a one-step sulfo-selenization process was developed, that opens the

possibility to control the S/Se ratio in the whole range, using a single thermal step to incorporate both elements. CZTSSe is typically formed from non-metallic precursors, thus excluding deposition of metallic precursors from forming this compound. In this work simultaneous sulfurization and selenization are used to form CZTSSe from metallic precursors, and the influence of process parameters (pressure, chalcogen source, temperature) on sulfur/selenium incorporation are studied. A maxium 4.4% efficiency device was produced in this work, and further optimization at IREC has resulted in a maximum efficiency of 5.9%. The final chapter includes work on an HCl etching process for ZnS in CZTS films. This was the first customized etching published for kesterite technologies, demonstrating the high selectivity of this etching process and their effectiveness. By removing this phase the series resistance of CZTS-based devices decreases, leading to significant improvements in efficiency, from 2.6% up to 5.2%, which is demonstrated to correlate with the ZnS removal on the CZTS surface.

In conclusion, the works presented in this thesis are a significant contribution to the study of thin film photovoltaics in general, and kesterite materials in particular. While still at an incipient state of development, kesterite-based devices have shown their potential with maximum device efficiencies of 12.6%, compared to over 20% for chalcopyrite-based devices. While still much lower, this is a notable result because much less research has been carried out on this material system. In order to improve this efficiency even further, specialized and unique processes and device structures must be developed. In this way the true potential and advantages of kesterite materials – the usage of earth abundant elements – may be realized.

Acknowledgements

First I would like to thank my advisors, Alejandro Pérez-Rodríguez and Edgardo Saucedo, for their guidance through these past years, and for taking a chance on a previously unknown foreigner by awarding me a PhD fellowship at IREC. It has been a tremendous experience and I am grateful to have had the opportunity to work with them and learn so much. I would also like to acknowledge and thank my colleagues in the Solar Energy Materials and Systems Laboratory at IREC, including: Victor Izquierdo-Roca, Xavier Fontané, Dioulde Sylla, Moises Espíndola-Rodríguez, Simon López-Marino, Marcel Placidi, Juan Lopez, Yudania Sanchez, Cristina Isignares, Mirjana Dimitrievska, Markus Neuschitzer, and Haibing Xie. Each and everyone have at some point collaborated or assisted me in some way, especially Victor, Xavier, and Dioulde, who have been at IREC since the time I arrived. I am also thankful for the help and collaboration of others at IREC, most notably the Functional Nanomaterials Group (Andreu Cabot, Maria Sabate Ibáñez, Doris Cadavid-Rodríguez, and Alex Carreté-Bello). My work has benefited greatly from collaborations with people in other institutions, especially the University of Barcelona. And also outside of Barcelona, with Eric Garcia-Hemme, Lionel Fourdrinier and Carmen Ruiz-Herrero, just to name a few. To finish on the professional side of things, I would simply like to acknowledge funding from the Spanish MINECO from grant FPU12/05508.

Work is only one side of the picture, and I must thank many people for their personal support during my life. First of course are my parents, Kevin Fairbrother and Andrea Morris, who taught me that I could be anything I wanted to be when I grew up, and always encouraged my curiosity and inquisitiveness, qualities which are of supreme importance to a good scientist or engineer. Also my brother, Curtis Fairbrother, who has always been there through the numerous moves to new cities, new schools, and new neighborhoods. My extended family was a little further because we always lived in different cities, but it was always a pleasure to visit them in Colorado or New York, and I am thankful to have them in my life. Many people have come and gone, such is the way things are when you constantly travel and work in new places, and they touched me at some point in my life. A couple I would like to especially thank are Maegen Lynch and Norelle Shlanta, who have been around the longest, and are always there when I need to talk. And I cannot forget to thank mila moja, who has brightened my life and made me more optimistic about the future, one I hope to share with her.

There are really too many people to thank, and I have surely overlooked some of great importance. Not only from my PhD work, but from all of my previous studies and work, because this has been a

cumulative effort, and there are countless people who have helped me both professionally and personally over the years.

References

(1) European Photovoltaic Industry Association. Global Market Outlook for Photovoltaics 2013-2017, 2013.

(2) US Energy Information Administration. Levelized Cost of New Generation Resources in the Annual Energy Outlook 2013, 2013.

(3) European Photovoltaic Industry Association. Solar Generation 6: Solar Photovoltaic Electricity Empowering the World, 2011.

(4) Zhao, J.; Wang, A.; Green, M. A.; Ferrazza, F. 19.8% Efficient "honeycomb" Textured Multicrystalline and 24.4% Monocrystalline Silicon Solar Cells. *Appl. Phys. Lett.* **1998**, *73*, 1991–1993.

(5) Shockley, W.; Queisser, H. J. Detailed Balance Limit of Efficiency of P-n Junction Solar Cells. *J. Appl. Phys.* **2004**, *32*, 510–519.

(6) Press Release 18/2013: ZSW Produces World Record Solar Cell, 2013.

(7) Candelise, C.; Speirs, J. F.; Gross, R. J. K. Materials Availability for Thin Film (TF) PV Technologies Development: A Real Concern? *Renew. Sustain. Energy Rev.* **2011**, *15*, 4972–4981.

(8) Zuser, A.; Rechberger, H. Considerations of Resource Availability in Technology Development Strategies: The Case Study of Photovoltaics. *Resour. Conserv. Recycl.* **2011**, *56*, 56–65.

(9) Wang, W.; Winkler, M. T.; Gunawan, O.; Gokmen, T.; Todorov, T. K.; Zhu, Y.; Mitzi, D. B. Device Characteristics of CZTSSe Thin-Film Solar Cells with 12.6% Efficiency. *Adv. Energy Mater.* **2013**, n/a–n/a.

(10) Scragg, J. J.; Ericson, T.; Kubart, T.; Edoff, M.; Platzer-Björkman, C. Chemical Insights into the Instability of Cu_2ZnSnS_4 Films during Annealing. *Chem. Mater.* **2011**, *23*, 4625–4633.

(11) Redinger, A.; Berg, D. M.; Dale, P. J.; Siebentritt, S. The Consequences of Kesterite Equilibria for Efficient Solar Cells. *J. Am. Chem. Soc.* **2011**, *133*, 3320–3323.

(12) Scragg, J. J.; Wätjen, J. T.; Edoff, M.; Ericson, T.; Kubart, T.; Platzer-Björkman, C. A Detrimental Reaction at the Molybdenum Back Contact in $Cu_2ZnSn(S,Se)_4$ Thin-Film Solar Cells. *J. Am. Chem. Soc.* **2012**, *134*, 19330–19333.

(13) López-Marino, S.; Placidi, M.; Pérez-Tomás, A.; Llobet, J.; Izquierdo-Roca, V.; Fontané, X.; Fairbrother, A.; Espíndola-Rodríguez, M.; Sylla, D.; Pérez-Rodríguez, A.; et al. Inhibiting the absorber/Mo-Back Contact Decomposition Reaction in $Cu_2ZnSnSe_4$ Solar Cells: The Role of a ZnO Intermediate Nanolayer. *J. Mater. Chem. A* **2013**, *1*, 8338–8343.

(14) Fairbrother, A.; Fontané, X.; Izquierdo-Roca, V.; Espíndola-Rodríguez, M.; López-Marino, S.; Placidi, M.; Calvo-Barrio, L.; Pérez-Rodríguez, A.; Saucedo, E. On the Formation Mechanisms of Zn-Rich Cu_2ZnSnS_4 Films Prepared by Sulfurization of Metallic Stacks. *Sol. Energy Mater. Sol. Cells* **2013**, *112*, 97–105.

(15) Fairbrother, A.; Izquierdo-Roca, V.; Fontané, X.; Ibáñez, M.; Cabot, A.; Saucedo, E.; Pérez-Rodríguez, A. ZnS Grain Size Effects on near-Resonant Raman Scattering: Optical Non-Destructive Grain Size Estimation. *CrystEngComm* **2014**, *in press*.

(16) Todorov, T. K.; Tang, J.; Bag, S.; Gunawan, O.; Gokmen, T.; Zhu, Y.; Mitzi, D. B. Beyond 11% Efficiency: Characteristics of State-of-the-Art $Cu_2ZnSn(S,Se)_4$ Solar Cells. *Adv. Energy Mater.* **2013**, *3*, 34–38.

(17) Repins, I.; Beall, C.; Vora, N.; DeHart, C.; Kuciauskas, D.; Dippo, P.; To, B.; Mann, J.; Hsu, W.-C.; Goodrich, A.; et al. Co-Evaporated $Cu_2ZnSnSe_4$ Films and Devices. *Sol. Energy Mater. Sol. Cells* **2012**, *101*, 154–159.

(18) Kato, T.; Hiroi, H.; Sakai, N.; Muraoka, S.; Sugimoto, H. Characterization of Front and Back Interfaces on Cu_2ZnSnS_4 Thin-Film Solar Cells. *Proc. 27th Eur. Photovolt. Sol. Energy Conf. Exhib.* **2012**, 2236–2239.

(19) Chen, S.; Gong, X. G.; Walsh, A.; Wei, S.-H. Defect Physics of the Kesterite Thin-Film Solar Cell Absorber Cu_2ZnSnS_4. *Appl. Phys. Lett.* **2010**, *96*, 021902–021902–3.

(20) Platzer-Björkman, C.; Scragg, J.; Flammersberger, H.; Kubart, T.; Edoff, M. Influence of Precursor Sulfur Content on Film Formation and Compositional Changes in Cu_2ZnSnS_4 Films and Solar Cells. *Sol. Energy Mater. Sol. Cells* **2012**, *98*, 110–117.

(21) Olekseyuk, I. D.; Dudchak, I. V.; Piskach, L. V. Phase Equilibria in the Cu_2S–ZnS–SnS_2 System. *J. Alloys Compd.* **2004**, *368*, 135–143.

(22) Scragg, J. J.; Dale, P. J.; Colombara, D.; Peter, L. M. Thermodynamic Aspects of the Synthesis of Thin-Film Materials for Solar Cells. *ChemPhysChem* **2012**, *13*, 3035–3046.

(23) Marcano, G.; Rincón, C.; de Chalbaud, L. M.; Bracho, D. B.; Pérez, G. S. Crystal Growth and Structure, Electrical, and Optical Characterization of the Semiconductor Cu_2SnSe_3. *J. Appl. Phys.* **2001**, *90*, 1847.

(24) Fairbrother, A.; García-Hemme, E.; Izquierdo-Roca, V.; Fontané, X.; Pulgarín-Agudelo, F. A.; Vigil-Galán, O.; Pérez-Rodríguez, A.; Saucedo, E. Development of a Selective Chemical Etch To Improve the Conversion Efficiency of Zn-Rich Cu_2ZnSnS_4 Solar Cells. *J. Am. Chem. Soc.* **2012**, *134*, 8018–8021.

(25) López-Marino, S.; Sánchez, Y.; Placidi, M.; Fairbrother, A.; Espindola-Rodríguez, M.; Fontané, X.; Izquierdo-Roca, V.; López-García, J.; Calvo-Barrio, L.; Pérez-Rodríguez, A.; et al. ZnSe Etching of Zn-Rich $Cu_2ZnSnSe_4$: An Oxidation Route for Improved Solar-Cell Efficiency. *Chem. – Eur. J.* **2013**, *19*, 14814–14822.

(26) Nesheva, D.; Šćepanović, M. J.; Aškrabić, S.; Levi, Z.; Bineva, I.; Popović, Z. V. Raman Scattering from ZnSe Nanolayers. *Acta Phys. Pol. A* **2009**, *116*, 75.

(27) Fairbrother, A.; Saucedo, E.; Fontané, X.; Izquierdo-Roca, V.; Sylla, D.; Espindola-Rodriguez, M.; Pulgarín-Agudelo, F. A.; Vigil-Galán, O.; Pérez-Rodríguez, A. Secondary Phase Formation in Zn-Rich $Cu_2ZnSnSe_4$ Based Solar Cells Annealed in Low Pressure and Temperature Conditions. *Prog. Photovolt. Res. Appl. accepted, in press*.

(28) Fontané, X.; Izquierdo-Roca, V.; Fairbrother, A.; Espindola-Rodriguez, M.; López-Marino, S.; Placidi, M.; Jawhari, T.; Saucedo, E.; Pérez-Rodríguez, A. Selective Detection of Secondary Phases in $Cu_2ZnSn(S,Se)_4$ Based Absorbers by Pre-Resonant Raman Spectroscopy. In *2013 39th IEEE Photovoltaic Specialists Conference (PVSC)*; 2013.

(29) Chen, S.; Gong, X. G.; Walsh, A.; Wei, S.-H. Electronic Structure and Stability of Quaternary Chalcogenide Semiconductors Derived from Cation Cross-Substitution of II-VI and I-III-VI_2 Compounds. *Phys. Rev. B* **2009**, *79*, 165211.

(30) Schorr, S.; Hoebler, H.-J.; Tovar, M. A Neutron Diffraction Study of the Stannite-Kesterite Solid Solution Series. *Eur. J. Mineral.* **2007**, *19*, 65–73.

(31) Schorr, S. The Crystal Structure of Kesterite Type Compounds: A Neutron and X-Ray Diffraction Study. *Sol. Energy Mater. Sol. Cells* **2011**, *95*, 1482–1488.

(32) Lafond, A.; Choubrac, L.; Guillot-Deudon, C.; Deniard, P.; Jobic, S. Crystal Structures of Photovoltaic Chalcogenides, an Intricate Puzzle to Solve: The Cases of CIGSe and CZTS Materials. *Z. Für Anorg. Allg. Chem.* **2012**, *638*, 2571–2577.

(33) Fontané, X.; Izquierdo-Roca, V.; Saucedo, E.; Schorr, S.; Yukhymchuk, V. O.; Valakh, M. Y.; Pérez-Rodríguez, A.; Morante, J. R. Vibrational Properties of Stannite and Kesterite Type Compounds: Raman Scattering Analysis of $Cu_2(Fe,Zn)SnS_4$. *J. Alloys Compd.* **2012**, *539*, 190–194.

(34) Chen, S.; Walsh, A.; Luo, Y.; Yang, J.-H.; Gong, X. G.; Wei, S.-H. Wurtzite-Derived Polytypes of Kesterite and Stannite Quaternary Chalcogenide Semiconductors. *Phys. Rev. B* **2010**, *82*, 195203.

(35) Lu, X.; Zhuang, Z.; Peng, Q.; Li, Y. Wurtzite Cu_2ZnSnS_4 Nanocrystals: A Novel Quaternary Semiconductor. *Chem. Commun.* **2011**, *47*, 3141–3143.

(36) Chen, S.; Walsh, A.; Gong, X.-G.; Wei, S.-H. Classification of Lattice Defects in the Kesterite Cu_2ZnSnS_4 and Cu</sub>2<sub>ZnSnSe$_4$ Earth-Abundant Solar Cell Absorbers. *Adv. Mater.* **2013**, *25*, 1522–1539.

(37) Ito, K.; Nakazawa, T. Electrical and Optical Properties of Stannite-Type Quaternary Semiconductor Thin Films. *Jpn. J. Appl. Phys.* **1988**, *27*, 2094–2097.

(38) León, M.; Levcenko, S.; Serna, R.; Nateprov, A.; Gurieva, G.; Merino, J. M.; Schorr, S.; Arushanov, E. Spectroscopic Ellipsometry Study of $Cu_2ZnGeSe_4$ and $Cu_2ZnSiSe_4$ Poly-Crystals. *Mater. Chem. Phys.* **2013**, *141*, 58–62.

(39) Mitzi, D. B.; Gunawan, O.; Todorov, T. K.; Wang, K.; Guha, S. The Path towards a High-Performance Solution-Processed Kesterite Solar Cell. *Sol. Energy Mater. Sol. Cells* **2011**, *95*, 1421–1436.

(40) Chen, S.; Yang, J.-H.; Gong, X. G.; Walsh, A.; Wei, S.-H. Intrinsic Point Defects and Complexes in the Quaternary Kesterite Semiconductor Cu_2ZnSnS_4. *Phys. Rev. B* **2010**, *81*, 245204.

(41) Grossberg, M.; Krustok, J.; Raudoja, J.; Raadik, T. The Role of Structural Properties on Deep Defect States in Cu_2ZnSnS_4 Studied by Photoluminescence Spectroscopy. *Appl. Phys. Lett.* **2012**, *101*, 102102–102102–4.

(42) Gokmen, T.; Gunawan, O.; Todorov, T. K.; Mitzi, D. B. Band Tailing and Efficiency Limitation in Kesterite Solar Cells. *Appl. Phys. Lett.* **2013**, *103*, 103506.

(43) Tanaka, T.; Sueishi, T.; Saito, K.; Guo, Q.; Nishio, M.; Yu, K. M.; Walukiewicz, W. Existence and Removal of Cu_2 Se Second Phase in Coevaporated $Cu_2ZnSnSe_4$ Thin Films. *J. Appl. Phys.* **2012**, *111*, 053522–053522–4.

(44) Redinger, A.; Mousel, M.; Wolter, M. H.; Valle, N.; Siebentritt, S. Influence of S/Se Ratio on Series Resistance and on Dominant Recombination Pathway in $Cu_2ZnSn(SSe)_4$ Thin Film Solar Cells. *Thin Solid Films* **2013**, *535*, 291–295.

(45) Biswas, K.; Lany, S.; Zunger, A. The Electronic Consequences of Multivalent Elements in Inorganic Solar Absorbers: Multivalency of Sn in Cu_2ZnSnS_4. *Appl. Phys. Lett.* **2010**, *96*, 201902–201902–3.

(46) Ruiz, C. M.; Fontané, X.; Fairbrother, A.; Izquierdo-Roca, V.; Broussillou, C.; Bodnar, S.; Pérez-Rodríguez, A.; Bermúdez, V. Impact of Electronic Defects on the Raman Spectra from Electrodeposited Cu(In,Ga)Se_2 Solar Cells: Application for Non-Destructive Defect Assessment. *Appl. Phys. Lett.* **2013**, *102*, 091106.

(47) Dimitrievska, M.; Fairbrother, A.; Pérez-Rodríguez, A.; Saucedo, E.; Izquierdo-Roca, V. Raman Scattering Crystalline Assessment of Polycrystalline Cu_2ZnSnS_4 Thin Films for Sustainable Photovoltaic Technologies: Phonon Confinement Model. **2014**, Under review.

(48) Scragg, J. J.; Kubart, T.; Wätjen, J. T.; Ericson, T.; Linnarsson, M. K.; Platzer-Björkman, C. Effects of Back Contact Instability on Cu_2ZnSnS_4 Devices and Processes. *Chem. Mater.* **2013**.

(49) Surgina, G. D.; Zenkevich, A. V.; Sipaylo, I. P.; Nevolin, V. N.; Drube, W.; Teterin, P. E.; Minnekaev, M. N. Reactive Pulsed Laser Deposition of Cu_2ZnSnS_4 Thin Films in H_2S. *Thin Solid Films* **2013**, *535*, 44–47.

(50) Shin, B.; Zhu, Y.; Bojarczuk, N. A.; Jay Chey, S.; Guha, S. Control of an Interfacial $MoSe_2$ Layer in $Cu_2ZnSnSe_4$ Thin Film Solar Cells: 8.9% Power Conversion Efficiency with a TiN Diffusion Barrier. *Appl. Phys. Lett.* **2012**, *101*, 053903–053903–4.

(51) Ahmed, S.; Reuter, K. B.; Gunawan, O.; Guo, L.; Romankiw, L. T.; Deligianni, H. A High Efficiency Electrodeposited Cu_2ZnSnS_4 Solar Cell. *Adv. Energy Mater.* **2012**, *2*, 253–259.

(52) Fairbrother, A.; Fontané, X.; Izquierdo-Roca, V.; Espindola-Rodriguez, M.; López-Marino, S.; Placidi, M.; López-García, J.; Pérez-Rodríguez, A.; Saucedo, E. Single-Step Sulfo-Selenization Method to Synthesize $Cu_2ZnSn(S_ySe_{1-y})_4$ Absorbers from Metallic Stack Precursors. *ChemPhysChem* **2013**, n/a–n/a.

(53) Brooks, L. S. The Vapor Pressures of Tellurium and Selenium. *J. Am. Chem. Soc.* **1952**, *74*, 227–229.

(54) Hirayama, C.; Ichikawa, Y.; DeRoo, A. M. Vapor Pressure of Tin Selenide and Tin Telluride. *J. Phys. Chem.* **1963**, *67*, 1039–1042.

(55) Alcock, C. B.; Itkin, V. P.; Horrigan, M. K. Vapour Pressure Equations for the Metallic Elements: 298–2500K. *Can. Metall. Q.* **1984**, *23*, 309–313.

(56) Piacente, V.; Foglia, S.; Scardala, P. Sublimation Study of the Tin Sulphides SnS_2, Sn_2S_3 and SnS. *J. Alloys Compd.* **1991**, *177*, 17–30.

(57) West, W. A.; Menzies, A. W. C. The Vapor Pressures of Sulphur between 100° and 550° with Related Thermal Data. *J. Phys. Chem.* **1928**, *33*, 1880–1892.

(58) Fairbrother, A.; Fourdrinier, L.; Fontané, X.; Izquierdo-Roca, V.; Dimitrievska, M.; Pérez-Rodríguez, A.; Saucedo, E. Precursor Stack Ordering Effects in $Cu_2ZnSnSe_4$ Thin Films Prepared by Rapid Thermal Processing. **2014**, Under review.

(59) Todorov, T. K.; Reuter, K. B.; Mitzi, D. B. High-Efficiency Solar Cell with Earth-Abundant Liquid-Processed Absorber. *Adv. Mater.* **2010**, *22*, E156–E159.

(60) Shin, B.; Gunawan, O.; Zhu, Y.; Bojarczuk, N. A.; Chey, S. J.; Guha, S. Thin Film Solar Cell with 8.4% Power Conversion Efficiency Using an Earth-Abundant Cu_2ZnSnS_4 Absorber. *Prog. Photovolt. Res. Appl.* **2013**, *21*, 72–76.

(61) Siebentritt, S. Why Are Kesterite Solar Cells Not 20% Efficient? *Thin Solid Films* **2013**, *535*, 1–4.

(62) Haight, R.; Barkhouse, A.; Gunawan, O.; Shin, B.; Copel, M.; Hopstaken, M.; Mitzi, D. B. Band Alignment at the $Cu_2ZnSn(S_xSe_{1-x})_4$/CdS Interface. *Appl. Phys. Lett.* **2011**, *98*, 253502.

(63) Bao, W.; Ichimura, M. Prediction of the Band Offsets at the CdS/Cu_2ZnSnS_4 Interface Based on the First-Principles Calculation. *Jpn. J. Appl. Phys.* **2012**, *51*, 10NC31.

(64) Barkhouse, D. A. R.; Haight, R.; Sakai, N.; Hiroi, H.; Sugimoto, H.; Mitzi, D. B. Cd-Free Buffer Layer Materials on $Cu_2ZnSn(S_xSe_{1-x})_4$: Band Alignments with ZnO, ZnS, and In_2S_3. *Appl. Phys. Lett.* **2012**, *100*, 193904.

(65) Bär, M.; Schubert, B.-A.; Marsen, B.; Krause, S.; Pookpanratana, S.; Unold, T.; Weinhardt, L.; Heske, C.; Schock, H.-W. Native Oxidation and Cu-Poor Surface Structure of Thin Film Cu_2ZnSnS_4 Solar Cell Absorbers. *Appl. Phys. Lett.* **2011**, *99*, 112103–112103–3.

(66) Timo Wätjen, J.; Engman, J.; Edoff, M.; Platzer-Björkman, C. Direct Evidence of Current Blocking by ZnSe in Cu_2ZnSnS_4 Solar Cells. *Appl. Phys. Lett.* **2012**, *100*, 173510–173510–3.

Appendix – Articles

Here the following articles referenced in the respective chapters may be found:

Chapter 2.3 “ZnS grain size effects on near-resonant Raman scattering: Optical non-destructive grain size estimation”

Chapter 3.3 “Impact of electronic defects on the Raman spectra from electrodeposited Cu(In,Ga)Se_2 solar cells: Application for non-destructive defect assessment”

Chapter 4.3 “Secondary phase formation in Zn-rich $Cu_2ZnSnSe_4$-based solar cells annealed in low pressure and temperature conditions”

Chapter 4.4 “Single-step sulfo-selenization method to synthesize $Cu_2ZnSn(S_ySe_{1-y})_4$ absorbers from metallic stack precursors”

Chapter 5.3 “Development of a selective chemical etch to improve the conversion efficiency of Zn-rich Cu_2ZnSnS_4 solar cells”

ZnS grain size effects on near-resonant Raman scattering: Optical non-destructive grain size estimation

Andrew Fairbrother,[a] Victor Izquierdo,[a] Xavier Fontané,[a] Maria Ibáñez,[a] Andreu Cabot,[a,b] Edgardo Saucedo,*[a] Alejandro Pérez-Rodríguez[a,c]

[a] Catalonia Institute for Energy Research (IREC), Jardins de les Dones de Negre 1, 08930 Sant Adrià de Besòs, Barcelona, Spain
[b] Institució Catalana de Recerca i Estudis Avançats (ICREA), Passeig Lluís Companys 23, 08010 Barcelona, Spain
[c] IN^{2}UB, Departament d´Electrònica, Universitat de Barcelona, C. Martí Franquès 1, 08028 Barcelona, Spain
* Email: afairbrother@irec.cat

Abstract

Near-resonant Raman scattering measurements of zinc sulfide nanoparticles and thin films have been made and correlated to grain or particle size respectively using a 325 nm wavelength excitation source. The area ratios between first, second, and third order peaks of ZnS identified as the T_2(LO) mode decrease with increasing ZnS grain size. This is an effect attributed to changes in bandgap energy from quantum confinement due to the varying grain size between the films/particles, as noted by a shift in the room temperature photoluminescence emission corresponding to the free exciton emission energy. While Raman scattering spectroscopy is typically limited to identification of phases and their crystalline properties, it is possible to attain more than such straightforward information by calibrating spectral features to variations between a set of samples. These results open the possibility of making a quantitative grain size estimation in ZnS thin films and nanostructures, as well as in other material systems where it may be expected as a secondary phase, such a Cu_2ZnSnS_4. Additionally, more commonly used excitation wavelengths for Raman scattering, such as 514 or 532 nm, are shown to be of limited use in characterizing ZnS thin films due to extremely low Raman scattering efficiency in films with sub-micron thicknesses.

Introduction

Zinc sulfide is a wide bandgap semiconductor of interest because of its optical and electronic properties. With a wide bandgap of 3.7 eV, and consequent low absorption in visible wavelengths, it has numerous applications, from filter and lens materials, to UV photodiodes and other compound semiconducting devices.[1–6] Depending on the intended application, ZnS nanoparticles and thin films can be prepared by various methods including physical vapor deposition, chemical vapor deposition, chemical bath deposition, and other wet chemical synthesis methods.[3–5,7,8] The fabrication method can significantly affect optical and electronic properties, in part because of varying grain or particle size which can affect these properties due to increased quantum confinement effects at the nanometer scale.[3–5,7–11]

In the Zn-S binary material system ZnS is the only expected phase under ambient pressure conditions.[12] The two polymorphs of ZnS include the low temperature α-ZnS, and high temperature β-ZnS (>1293 K), which crystallize, respectively, in the zincblende (cubic) and wurtzite (hexagonal) crystal structures.[12] Characterization of crystalline quality and thickness of ZnS thin films and devices is commonly made with traditional methods such as x-ray diffraction (XRD) and scanning or transmission electron microscopy (SEM or TEM).[2,3,5–7,10] As the physical dimensions of the films or structures are decreased, XRD becomes less viable due to the smaller amount of material available for analysis, and SEM becomes limited by resolution. In light of

this deficiency, Raman scattering spectroscopy is a promising alternative because it can be more sensitive to thinner films and able to measure in a smaller, and even microscopic area when coupled with a microscope.[13,14]

The Raman scattering spectra of ZnS (Alfa Aesar, 99.99%) under green excitation conditions (λ = 514 nm, 2.41 eV) is shown in Fig. 1, and is found to have a main peak at 347.8 cm^{-1}, identified as a T_2(LO) mode,[14,15] commonly referred to as simply a LO mode in literature (i.e. references 2, 4, 10). In order to simplify notation and better fit with the commonly used description of this peak, hereafter this peak will be referred to as a LO mode, rather than T_2(LO). In addition to this LO peak, several weaker peaks are identified as pure acoustic or optical modes, and combinations of these.[14,15] Under UV excitation conditions (λ = 325 nm, 3.82 eV) near-resonant scattering is observed[4,9,13] and the peak at 348 cm^{-1} is strongly enhanced. Second and third order peaks of each of these modes are also observed (LO2 and LO3). Additional peaks are identified at 277 cm^{-1} (T_2(TO)) and 419 cm^{-1} (second order TO + LA and LO + TA modes)[14] are also observed. The broad bands centered around 635 and 978 cm^{-1} are higher order combinations of these fundamental modes. It is important to note that because of the near-resonant scattering, the measurement acquisition time is two to three orders of magnitude lower than under green excitation conditions, on the order of seconds versus minutes.

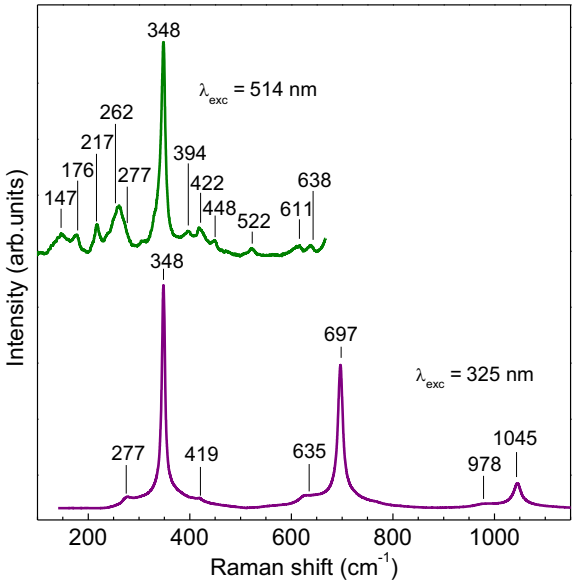

Fig. 1. Raman spectra of ZnS powder with 514 nm excitation (top spectra), a 325 nm excitation (bottom spectra); note that measurement acquisition times when using 325 nm excitation are 2-3 orders of magnitude shorter when compared with 514 nm excitation.

ZnS may also appear as a secondary phase in other multinary compound material systems, such as I-Zn-IV-S (I: Cu, Ag, Au; IV: Si, Ge, Sn),[16–18] and Zn,(II)-III-S (II: Cd, Hg; III: Al, Ga, In).[19–21] Of these, Cu_2ZnSnS_4 (CZTS) has received significant attention recently due to promising results for use as a thin film absorber layer in solar cells.[17,18] The highest performance devices are based on CZTS absorber layers are prepared under Zn-rich conditions, which can lead to the formation of ZnS. The ZnS secondary phase has been shown to affect solar cell device properties by increasing series resistance when present on the surface of the CZTS absorber films.[17,18] ZnS in this system is particularly difficult to detect in part because it is present in minor quantities, but more critically due to the overlapping of most characteristic x-ray diffraction peaks with CZTS, including the main peak around 2θ = 28-29°. However, with near-resonant Raman scattering this limitation is overcome due to the strong enhancement of the Raman scattering cross section and consequent increase in Raman scattering efficiency.

In this work a study of ZnS nanoparticles and thin films with varying particle size of thickness, respectively, was made using x-ray diffraction and Raman scattering spectroscopy with 514 nm and 325 nm excitation. ZnS is shown to have very low scattering efficiency with 514 nm excitation, and being detectable only in films with thicknesses on the order of 1 μm and higher. With 325 nm excitation even the thinnest film (about ten nm thick) is readily detectable. A correlation between grain size and the area or intensity ratio of the first, second, and third order LO peaks (LO/LO2 and LO/LO3) is found. This behavior is attributed to variations of the material bandgap energy from quantum confinement due to the small grain size, and a corresponding shift in the photoluminescence emission from the free exciton energy.[3,9,13] Correlating the crystallite size measured by XRD with the UV Raman measurements permits an estimation of ZnS grain size and minimum thickness in thin films and other nanostructures. Application of this measurement to estimate the ZnS grain size is applied to CZTS films in which ZnS is present as a secondary phase in varying quantities.

Experimental

Thin film formation

ZnS thin films were prepared by sulfurization of sputter deposited Zn films. Glass substrates with 500 nm of Mo were used for the deposition of Zn thin films by DC-magnetron sputtering (Alliance Concepts Ac450) at room temperature from a 99.99% purity Zn target. Mo-coated glass was chosen in order to provide a reference signal for normalization in XRD measurements, and also to reduce interference in XRD and Raman measurements from fluorescence of the underlying glass substrate. Deposition parameters for the Zn precursor films include a power density of 1.27 W/cm^2 and Ar pressure of 1x10^3 mbar. Zn films were prepared with thicknesses from a few nanometers up to hundreds of nanometers. The Zn precursor films were placed in a graphite box containing 50 mg of sulfur power (Alfa-Aesar, 99.995%), and then heated up to 550 ºC for 30 minutes under a 1 bar Ar atmosphere, and left to cool naturally to room temperature. The thermal treatment leads to the formation of ZnS films of varying thickness and grain size.

Nanoparticle formation

ZnS nanoparticles were prepared using a modified approach developed by Yu et al.[8] Octadecene (10 mmol, Sigma-Aldrich, 90%), hexadecylamine (Sigma-Aldrich, 90%), and elemental sulfur (3 mmol, Sigma-Aldrich, 99.98%) were mixed and degassed under vacuum for one hour at 100 ºC. With the addition of diethyl zinc (0.5 mmol, Sigma-Aldrich, 52.0 wt%), the temperature reduced to 45 ºC, and the mixture was then heated to 300 ºC, at which point the temperature maintained for two hours. After cooling to room temperature, the crude solution was washed by sequential precipitation with acetone and redispersion with chloroform. Varying the amount of hexadecylamine in the starting mixture changes the size of the resulting ZnS nanoparticles.

Characterization

As-grown ZnS nanoparticles and films were then characterized and the particle or grain sizes correlated to these results. X-ray diffraction (XRD) measurements with a Bruker D8 diffractometer were made in order to estimate the crystallite/grain size in the films. A Zeiss Series Auriga field emission scanning electron microscope (SEM) with 10 kV acceleration voltage was used to probe film morphology, and in addition to x-ray fluorescence measurements (XRF) with a Fischerscope XVD spectrometer, used to estimate film thickness. Transmission electron microscopy (TEM) was used to measure average size of the nanoparticles using a Zeiss Libra 120 microscope with a 120 keV accelerating voltage. Finally, room temperature Raman scattering measurements were made using a T64000 Horiba-Jobin Yvon spectrometer (514 nm excitation source) and LabRam HR800-UV Horiba-Jobin Yvon spectrometer (325 nm excitation source). The measurement spot sizes were approximately 100 μm for 514 nm excitation, and 1 μm for the 325 nm excitation, rastered over an area of

30x30 μm using a DuoScan accessory. Based on the results from these characterizations, the estimation for ZnS grain size is applied to CZTS films with varying amounts of superficial ZnS, where it is present as a secondary phase.

Results and discussion:

Fig. 2 shows TEM and SEM images of some of the nanoparticle and thin film samples used in this work. A relatively uniform distribution of nanoparticle sizes is evident in Fig. 2A. For the thinner ZnS film there is uniform growth, and a thickness of less than 30 nm (Fig. 2B). Also visible is the underlying Mo/MoS_2 substrate. For a much thicker ZnS film (Fig. 2C) nanometric grains are seen in spite of the thickness being greater than 1 μm. This is later confirmed with XRD measurements which were used to estimate the grain sizes of the thin films.

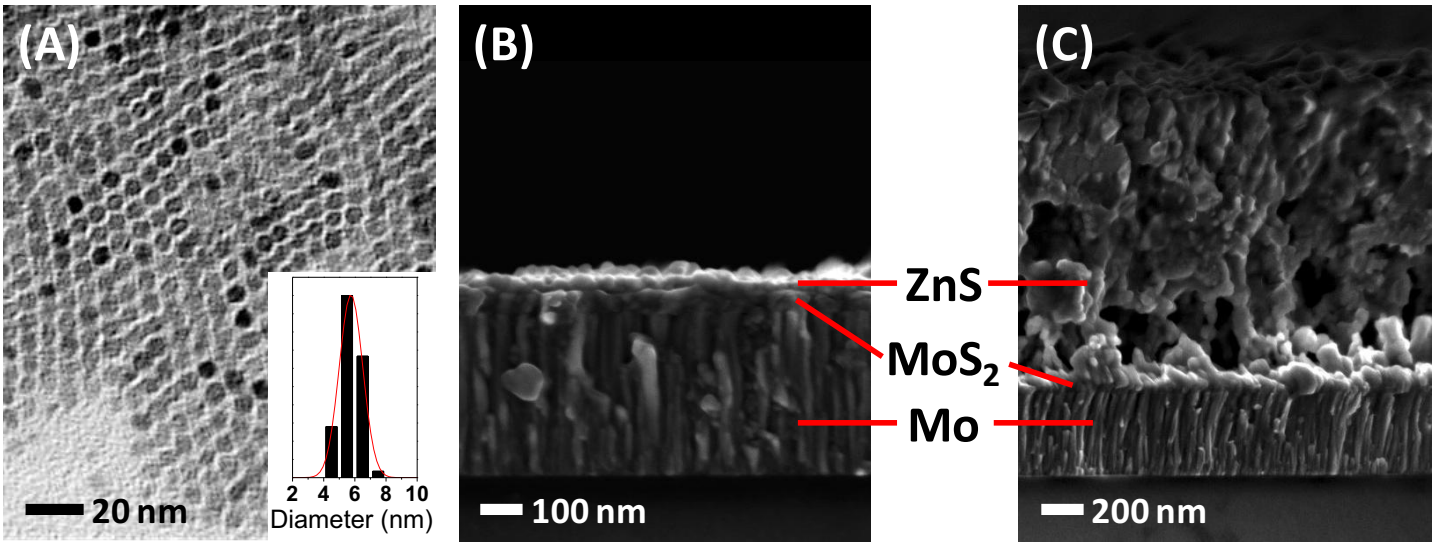

Fig. 2. TEM of ZnS nanoparticles with inset showing histogram of size distribution (A), and cross sectional SEM of ZnS thin films of different thickness (B and C).

Characterization of the ZnS films by Raman scattering spectroscopy with standard excitation conditions (λ_{exc} = 514 nm) and XRD proved to be rather limited, especially in the case of the thinnest films. Raman scattering spectra of two ZnS films are shown in Fig. 3A. Raman scattering efficiency in ZnS films is very weak with green excitation, due to low absorption and scattering in that range.[7] In fact, the strongest signal comes from the underlying MoS_2 layer which formed from sulfurization of the substrate during thermal treatment. The MoS_2 signal (principal peaks at 286, 383, and 408 cm^{-1}) is visible even for relatively thick ZnS films (1400 nm), while ZnS only barely becomes detectable above this thickness. As most standard Raman measurements are performed with 514 nm or 532 nm excitations, it is important to take note of the low Raman scattering efficiency of ZnS with visible wavelengths, due to weak photon-matter interaction under such conditions. XRD is more capable in characterization of the thinner ZnS films, as seen in Fig. 3B, and ZnS (zincblende), Mo, and MoS_2 are the main phases detected. With XRD a 30 nm thick film is barely detectable, though for more detailed characterization, thicker films would be more ideal. In the thicker films there is clear preferential texturing of the along the (220) plane when compared with the bulk reference. Under near-resonant Raman scattering conditions shown next, this texturing should have little effect on the results, except in the case polarization measurements are performed. Though wurtzite ZnS may be present in small quantities as a secondary phase, it has similar scattering characteristics in near-resonant Raman and is not expected to significantly alter the interpretation of the subsequent results if it is present. Diffractograms of the thin films were used to make an estimation of the crystallite size using the Scherrer equation. The crystallite size is

approximately equivalent to the grain size, though actual grain size may be larger than crystallite size in some cases.

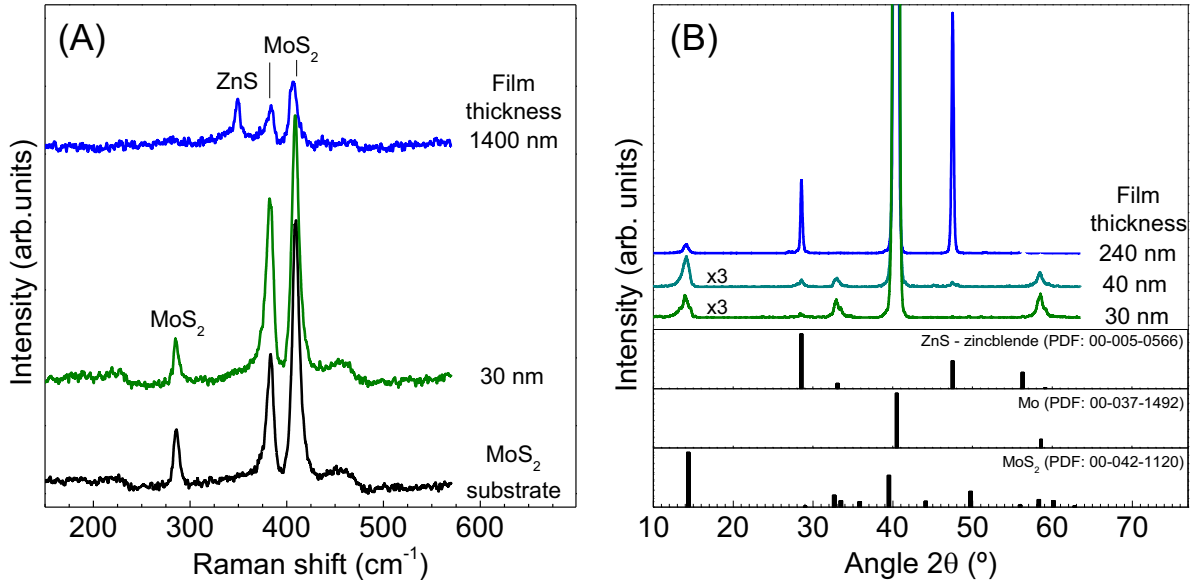

Fig. 3. Raman spectra with green excitation (514 nm) of ZnS films showing the underlying MoS_2 layer and demonstrating the limited detection of ZnS (A), and XRD of sample films, including reference patterns for both ZnS, Mo, and MoS_2 (B).

Raman scattering measurements using UV excitation (λ_{exc} = 325 nm) are shown in Fig. 4A of as prepared ZnS nanoparticles and thin films. Note that samples are now referred to by their estimated grain size, and not their thickness. In contrast with Raman scattering using 514 nm excitation and XRD, even the thinnest ZnS film is readily detected with characteristics peaks as seen in the powder sample (Fig. 1). The LO peak position moves slightly towards lower Raman shift as particle or grain size increases, from 349.4 cm^{-1} for the thinnest film, up to 348.0 cm^{-1} for the film with the largest grains. This shift may be attributed to strain effects from a lattice mismatch with the substrate,[4] an effect of phonon confinement,[11] or both factors. Additionally, and more significantly, there is a change in area and intensity ratios between the first, second, and third order ZnS peaks (LO/LO2 and LO/LO3). As shown in Fig. 4B, this ratio increases with the decrease in grain size. This is attributed to a room temperature photoluminescence emission correlated to the free exciton energy, which is related to and on the order of the bandgap energy, but with lower energy.[9,13] This contribution is shown in Fig. 4A by dashed lines. In the case of the nanoparticles and thinnest films, which exhibit higher bandgap energies, the free exciton energy is at or even above to the excitation energy of 325 nm (3.82 eV), which leads to an enhancement of the principal LO mode of ZnS. As the film thickness and grain size increases, the corresponding bandgap energies are lower, and the free exciton energy shifts further away from the excitation energy, leading to increased enhancement of the LO2, and then LO3 peaks. This effect seen more clearly when calculating the area or intensity ratios of LO/LO2 and LO/LO3, shown in Fig. 4B. The decrease is logarithmic up to approximately 20 nm, at which point quantum confinement effects become less significant and the values level off. A logarithmic dependence of the bandgap is expected for nanometric semiconductor crystallites,[22,23] in agreement with the observed trend. Note that these ratios are calculated after removing the baseline photoluminescence contribution (dashed lines in Fig. 4A). It is interesting to remark that Fig. 4B also contains data from Wang et al.[5] for even smaller sized nanoparticles, which agrees with the behavior observed in the nanoparticles and thin films of this work.

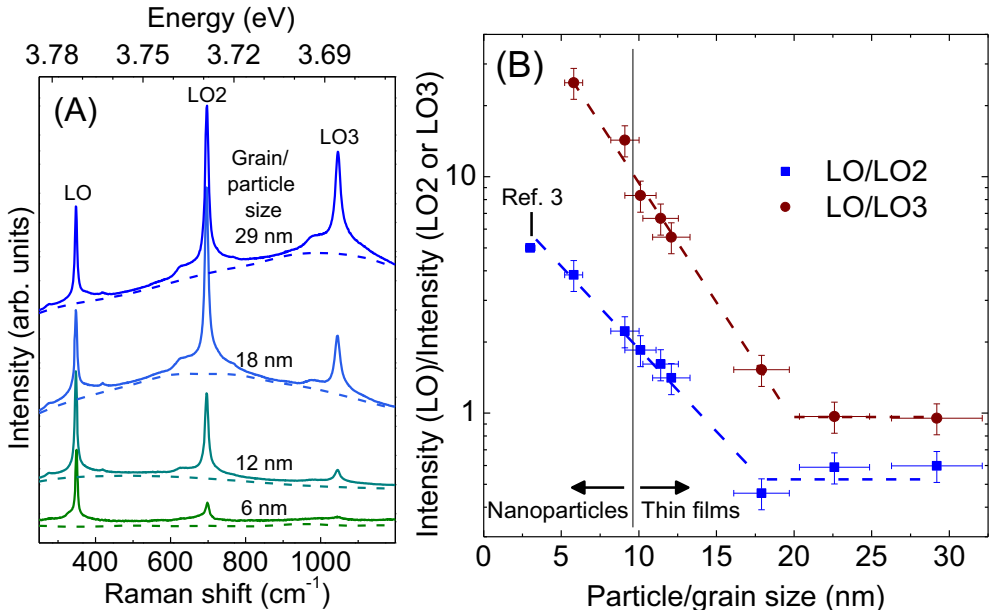

Fig. 4. Raman spectra (solid lines) with UV excitation (325 nm) of ZnS nanoparticles and films and, including baseline photoluminescence contribution (dashed lines) (A), and intensity ratio of the main ZnS peaks (LO/LO2 and LO/LO3), showing dependence on grain or particle size (B), note that the first data point for LO/LO2 is taken from Wang et al.[5]

These results open interesting perspectives for the non-destructive estimation of ZnS grain sizes, which is particularly useful because numerous applications require careful control of crystallite size. For example, Hu et al.[1] develop ZnO/ZnS photodetectors which have stronger absorption and photocurrent than monolayer-based devices, which they attribute to the presence of whispering gallery mode resonances in the ZnS layer. These resonances are strongly dependent on the optical and electronic properties of a material, and while the size of their ZnS crystallites is about 20 nm, on the limit of the dependence shown in Fig. 4, if they were reduced in size the performance of the device may be significantly altered. Again, in quantum dots not only is the material itself important, but also the particle size or layer thickness (in case of multilayer quantum dots), both of which influence absorption and photoluminescence properties, and final device characteristics.[2,6] Use of near-resonant excitation conditions allows the use of very short integration times that can be on the order of seconds, which is a significant advantage when compared to TEM- or XRD-base grain size estimations. The possibility of using a small sized Raman spectrometer probe together with the short measurement times makes these measurements compatible with the development of methodologies for process monitoring applications at the online/inline level, which are required for process and quality control in large scale industrial applications.

In addition to ZnS nanoparticles and thin films, this method of quasi-quantitative analysis can be applied to other material systems in which ZnS is an expected secondary phase. A noteworthy example is Cu_2ZnSnS_4 (CZTS), which has received significant interest in recent years due to its potential as a low-cost thin film solar cell absorber material. Higher efficiency devices based on CZTS films are typically prepared under Zn-rich conditions, and this imposed Zn-excess may lead to the formation of ZnS as a secondary phase.[16–18] It is of interest to be able to detect and characterize this phase, and also remove it, as it can deteriorate the performance of CZTS-based devices. To apply this measurement methodology, Zn-rich CZTS films were selectively etched using a procedure presented in work by Fairbrother et al.[17] The films were etched in an HCl solution for varying amounts of time, which selectively removes ZnS from the CZTS film surface until little ZnS is present (>300 seconds of etching). The UV Raman spectra for this set of samples is shown in Fig. 5, while the inset shows the LO/LO2 area ratios. Similar to the case observed previously, the increasing spatial confinement of the ZnS phase from etching results in an increase in free exciton energy, and consequent enhancement of the LO peak with respect to the LO2 peak. Using the rubric presented in Fig. 4B, the grain

size of the superficial ZnS layer is estimated to decrease from 14 nm in the as-grown film, to less than 7 nm after 300 seconds of etching, an etch rate of approximately 1.4 nm per minute. Further etching does not reduce the signal of ZnS, indicating that part of this phase is located just beneath the surface of the films and is therefore unaffected by the etching process. This removal of ZnS from the CZTS films is further corroborated by XRF measurements, with which a reduction in the Zn content from 17 at% down to 14 at% is observed after the etching procedure.

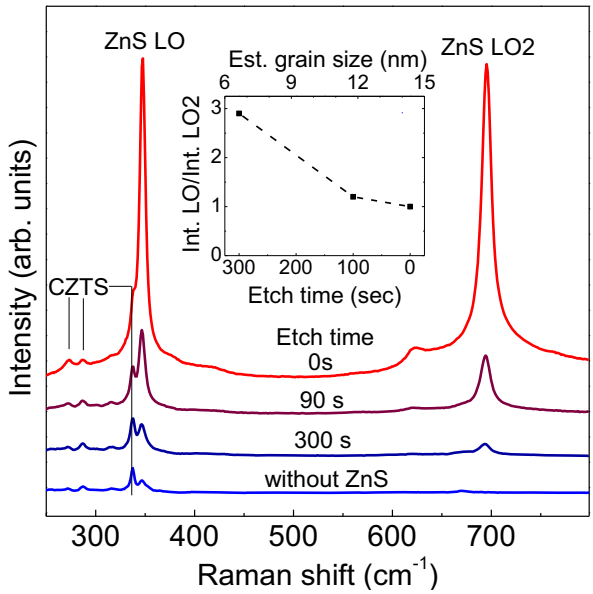

Fig. 5. UV Raman spectra of as-grown and etched CZTS films (from procedure presented in Fairbrother et al.[17]), the inset shows the intensity ratio of LO/LO2 ZnS peaks from the spectra.

Conclusions

XRD and Raman scattering spectroscopy have been used for structural and grain size characterization of ZnS nanoparticles and thin films. XRD and Raman with 514 nm excitation are shown to be of limited use for characterizing ZnS thin films with sub-micron dimensions because of the small quantity of material available for analysis. Near-resonant Raman scattering characterization with a 325 nm excitation source is much more aptly suited, and spectral characteristics were correlated to particle and grain size. At the nanometer scale decreasing the grain size leads to an increase in quantum confinement, which causes an increase in the optical bandgap of the material. This increase is reflected in a varied photoluminescence emission from the free exciton energy, and preferentially enhances the main LO Raman peak, or the LO2 and LO3 peaks, depending on the grain size. The ratio of LO/LO2 and LO/LO3 can thus be used to perform a quantitative estimation of the grain size in ZnS nanoparticles and films. An application using CZTS thin films, in which ZnS is commonly encountered as a secondary phase, was demonstrated. The CZTS films were etched for different times in an HCl solution which preferentially removed ZnS from the surface.

Acknowledgements

This research was supported by the People Programme (Marie Curie Actions) of the European Union´s Seventh Framework Programme under REA grant agreement number 269167 (PVICOKEST) and the Spanish Ministerio de Economía y Competividad (MINECO) under KEST-PV (ref. ENE2010-121541-C03-01/02). Authors from IREC belong to the M-2E (Electronic Materials for Energy) Consolidated Research Group and the XaRMAE Network of Excellence on Materials for Energy of the “Generalitat de Catalunya”. A. Fairbrother

thanks the MINECO for support via the FPU program (FPU12/05508), V. Izquierdo for the Juan de la Cierva program (JCI-2011-10782), and E. Saucedo for the Ramón y Cajal program (RYC-2011-09212).

Notes and references

1. L. Hu, M. Chen, W. Shan, T. Zhan, M. Liao, X. Fang, X. Hu, and L. Wu, *Adv. Mater.*, 2012, **24**, 5872–5877.
2. S. Kim, T. Kim, M. Kang, S. K. Kwak, T. W. Yoo, L. S. Park, I. Yang, S. Hwang, J. E. Lee, S. K. Kim, and S.-W. Kim, *J. Am. Chem. Soc.*, 2012, **134**, 3804–3809.
3. A. U. Ubale, V. S. Sangawar, and D. K. Kulkarni, *Bull. Mater. Sci.*, 2007, **30**, 147–151.
4. Y.-M. Yu, M.-H. Hyun, S. Nam, D. Lee, B. O, K.-S. Lee, P. Y. Yu, and Y. D. Choi, *J. Appl. Phys.*, 2002, **91**, 9429–9431.
5. X. Wang, J. Shi, Z. Feng, M. Li, and C. Li, *Phys. Chem. Chem. Phys.*, 2011, **13**, 4715–4723.
6. J. Liu, H. Chen, Z. Lin, and J.-M. Lin, *Anal. Chem.*, 2010, **82**, 7380–7386.
7. S. S. Kumar, M. A. Khadar, K. G. M. Nair, S. Dhara, and P. Magudapathy, *J. Raman Spectrosc.*, 2008, **39**, 1900–1906.
8. J. H. Yu, J. Joo, H. M. Park, S.-I. Baik, Y. W. Kim, S. C. Kim, and T. Hyeon, *J. Am. Chem. Soc.*, 2005, **127**, 5662–5670.
9. Y.-M. Yu, S. Nam, B. O, K.-S. Lee, Y. D. Choi, M.-Y. Yoon, and P. Y. Yu, *Mater. Chem. Phys.*, 2003, **78**, 149–153.
10. A. V. Baranov, Y. P. Rakovich, J. F. Donegan, T. S. Perova, R. A. Moore, D. V. Talapin, A. L. Rogach, Y. Masumoto, and I. Nabiev, *Phys. Rev. B*, 2003, **68**, 165306.
11. A. K. Arora, M. Rajalakshmi, T. R. Ravindran, and V. Sivasubramanian, *J. Raman Spectrosc.*, 2007, **38**, 604–617.
12. K. C. Sharma and Y. A. Chang, *J. Phase Equilibria*, 1996, **17**, 261–266.
13. H. Kanie, M. Nagano, and M. Aoki, *Jpn. J. Appl. Phys.*, 1991, **30**, 1360–1362.
14. W. G. Nilsen, *Phys. Rev.*, 1969, **182**, 838–850.
15. Y. C. Cheng, C. Q. Jin, F. Gao, X. L. Wu, W. Zhong, S. H. Li, and P. K. Chu, *J. Appl. Phys.*, 2009, **106**, 123505.
16. X. Fontané, L. Calvo-Barrio, V. Izquierdo-Roca, E. Saucedo, A. Pérez-Rodriguez, J. R. Morante, D. M. Berg, P. J. Dale, and S. Siebentritt, *Appl. Phys. Lett.*, 2011, **98**, 181905–181905–3.
17. A. Fairbrother, E. García-Hemme, V. Izquierdo-Roca, X. Fontané, F. A. Pulgarín-Agudelo, O. Vigil-Galán, A. Pérez-Rodríguez, and E. Saucedo, *J. Am. Chem. Soc.*, 2012, **134**, 8018–8021.
18. T. Kato, H. Hiroi, N. Sakai, S. Muraoka, and H. Sugimoto, *Proc. 27th Eur. Photovolt. Sol. Energy Conf. Exhib.*, 2012, 2236–2239.
19. H. Zhang, Y. Zhang, Q. He, L. Liu, G. Ding, and Z. Jiao, *CrystEngComm*, 2011, **13**, 6650–6657.
20. S. B. Bonsall and F. A. Hummel, *J. Solid State Chem.*, 1978, **25**, 379–386.
21. S. Peng, L. Li, Y. Wu, L. Jia, L. Tian, M. Srinivasan, S. Ramakrishna, Q. Yan, and S. G. Mhaisalkar, *CrystEngComm*, 2013, **15**, 1922–1930.
22. L. E. Brus, *J. Chem. Phys.*, 1984, **80**, 4403–4409.
23. S. Baskoutas and A. F. Terzis, *J. Appl. Phys.*, 2006, **99**, 013708.

AIP | Applied Physics Letters

Impact of electronic defects on the Raman spectra from electrodeposited Cu(In,Ga)Se2 solar cells: Application for non-destructive defect assessment

C. M. Ruiz, X. Fontané, A. Fairbrother, V. Izquierdo-Roca, C. Broussillou et al.

Citation: Appl. Phys. Lett. **102**, 091106 (2013); doi: 10.1063/1.4793418
View online: http://dx.doi.org/10.1063/1.4793418
View Table of Contents: http://apl.aip.org/resource/1/APPLAB/v102/i9
Published by the American Institute of Physics.

Impact of electronic defects on the Raman spectra from electrodeposited Cu(In,Ga)Se_2 solar cells: Application for non-destructive defect assessment

C. M. Ruiz,[1,2] X. Fontané,[3] A. Fairbrother,[3] V. Izquierdo-Roca,[3] C. Broussillou,[1] S. Bodnar,[1] A. Pérez-Rodríguez,[3,4] and V. Bermúdez[1]
[1]*NEXCIS, Photovoltaic Technology, Rousset, France*
[2]*Aix-Marseille University-IM2NP, CNRS, UMR 7334, France*
[3]*IREC, Catalonia Institute for Energy Research, Sant Adrià del Besòs, Barcelona, Spain*
[4]*IN^{2}UB, Departament d'Electrònica, Universitat de Barcelona, Barcelona, Spain*

(Received 19 November 2012; accepted 11 February 2013; published online 6 March 2013)

This work reports on the electrical and Raman scattering analysis of Cu(In,Ga)Se_2 cells synthesised with different densities of Se and Cu related point defects. The analysis of the Raman spectra from the surface region of the absorbers shows a direct correlation between the spectral features of the main Raman peak and the density of Se vacancies detected by admittance spectroscopy, being sensitive to the presence of vacancy densities higher than 10^{15} cm^{-3}. These results corroborate the potential of Raman scattering for the non-destructive detection of electronic defects with potential impact on the characteristics of the solar cells. © *2013 American Institute of Physics*. [http://dx.doi.org/10.1063/1.4793418]

$CuInSe_2$ and its related chalcopyrite alloys—such as Cu(In,Ga)Se_2 (CIGS)—have received strong interest in the last years because of their potential for the development of high efficiency and low cost solar cells and modules. The efficiency of chalcopyrite based laboratory cells has achieved a record value higher than 20%.[1] Chalcopyrite based technologies have already entered the stage of industrial mass production, with commercial modules that provide stable efficiencies in the range of 12%–13%.[2] However, attaining higher efficiency values at the module level is challenging due to the difficulty of controlling the production processes on large area substrates. In particular, CIGS films produced by large scale processes may contain several inhomogeneities that can lead to significant loss in the performance of the modules or to their degradation over time. Detection of potentially detrimental defects at an early stage of production is of great interest, giving the possibility to correct the anomalies in the process and minimize their impact on the completed devices. While certain inhomogeneities such as Ga distribution or selenization rate can already be detected by current inline quality control techniques applied to CIGS module production, such as techniques based on x-ray fluorescence (XRF) or photoluminescence (PL),[3] detection at early process stages of inhomogeneities related to point defects is still a challenging issue. Point defects normally occur in sufficiently low concentrations to be undetectable by XRF measurements, but can potentially be very detrimental for the final module performance. They cannot be detected by room temperature PL either, because of the low optical efficiency of their corresponding transitions. Traditional techniques for detection of these kinds of defects such as low temperature PL, admittance spectroscopy, or deep level transient spectroscopy (DLTS) are not suitable for in-line process control applications, due to the necessity of long measurement times and limited size of the samples.[4]

On the other hand, Raman scattering is an optical non-destructive technique that has a significant potential for the development of process monitoring tools, thanks to its ability to provide information directly related to the chemical and structural properties of the films at different process steps. The technique is also very well adapted to the analysis of the homogeneity of the films and is able to achieve diffraction limited spatial resolution ($\sim$1 μm). The direct interrelation of these features with the optoelectronic properties of the solar cells developed with these materials shows a correlation between the spectral features of the main Raman peaks in the spectra from chalcopyrite based absorbers and the characteristics of the devices.[5,6] This has usually been related to the presence of defects affecting the crystalline quality of the absorbers. However, quantitative correlation of these effects with the presence of point defects identified in the films is still lacking in literature reports.

In this context, we report on the correlation between the electrical characterization and the Raman scattering analysis of electrodeposited CIGS absorber films and devices.

Electrodeposition based processes have a strong potential to achieve a significant reduction of production costs with an industrial implementation at mass production stages. CIGS cells have been produced with different densities of electronic defects that have been identified and characterised by admittance spectroscopy measurements. This has allowed us to analyse the dependence of the Raman spectral features on the presence and density of the different kinds of defects identified in the films. The results corroborate the potential of Raman scattering measurements for the early stage non-destructive detection of inhomogeneities related to the presence of electronic defects with a potential impact on the characteristics of the cells, such as Se vacancies in Cu(In,Ga)Se_2 based devices.

Cu(In,Ga)Se_2 absorbers have been synthesised on 15×15 cm^2 Mo coated soda-lime glass substrates with a two-step process including the electrodeposition of Cu/In/Ga metallic stack precursors followed by the selenization under different rapid thermal processing (RTP) conditions. For these experiments, two sets of Cu-poor precursors (Cu/(Ga + In) = 0.8 and 0.95 content ratios) have been used with

a constant Ga/(Ga + In) content ratio of 0.3. A selenium layer has then been deposited on the precursors prior to the RTP annealing step.[7]

After absorber formation, cells have been completed by chemical bath deposition of a CdS buffer layer and sputtering deposition of a ZnO(i)-ZnO(Al) window layer. The best material obtained on these $15 \times 15\,cm^2$ samples yielded active area efficiencies up to 12%.

Admittance spectroscopy measurements have been carried out on the finished devices in the 80 K–320 K temperature range with an Agilent 4282 LCR-meter. Density of states (DOS) profiles have been calculated following the method proposed by Walter *et al.*[8] for all the samples. Defect density has been determined from the area of the peak for each defect. Raman scattering measurements have been performed directly on the surface of the absorbers, after an HCl-etching of the window and buffer layers. The Raman spectra have been made in backscattering configuration using a Horiba Jobin-Yvon T64000 spectrometer with an Ar^+ laser excitation source (514.5 nm excitation wavelength), with a laser spot size on the sample of about 100 μm. For these experimental conditions, penetration depth of scattered light in Cu(In,Ga)Se_2 is approximately 100 nm. This is similar to the depth of the space charge region where the DOS profiles have been extracted from the electrical measurements. The spectral features of the main peaks in the spectra (frequency, full width at half maximum (FWHM)) have been obtained from their fitting with Lorentzian curves.

Figure 1 shows typical DOS profiles measured from different devices. These measurements allow identification of two main defects in the samples: one at about 100 meV (D_1 defect) and a deeper one at 210 meV (D_2 defect). The presence and intensity of both defects vary from one sample to another, indicating the variation of the electronic nature of the samples with the changes in the absorber layer. In particular, the defect at 100 meV has been previously identified as the selenium vacancy (V_{Se}).[9] The nature of the 210 meV remains unclear, but it seems to be related with the Cu content of the CIGS layers. Defect densities calculated from each peak surface area on the DOS give values from $10^{15}\,cm^{-3}$ up to $6 * 10^{16}\,cm^{-3}$ for defect D_1, while defect D_2 appears within a smaller density range (from $5 * 10^{15}\,cm^{-3}$ up to $10^{16}\,cm^{-3}$).

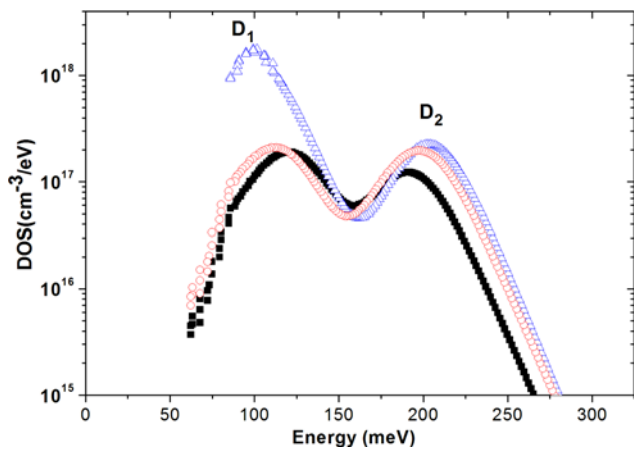

FIG. 1. DOS energy profile from selected cells showing the presence of two defects at 100 meV (D_1) and 210 meV (D_2).

As the impact of a particular defect in the characteristic of the cells is difficult to assess from experimental values, a batch of simulations has been performed with SCAPS 3.0.01 (Refs. 10 and 11) to determine the effect of defects D_1 and D_2 in the performance of the devices. JV curves have been calculated taking as starting point a model of a standard NEXCIS cell developed from experimental results as in other cases.[12] The model is constructed as a stacking of layers, with each layer corresponding to a film in the actual device. Measured physical parameters of the layers (such as thickness, bandgap, doping density, etc) are introduced in the software in order to produce a model comparable with a real cell.[13] The defects are included in the layer corresponding to the CIGS properties. For this, experimental data from the admittance measurements are implemented for each defect (defect energy, density, energy distribution, etc).[14] Two different types of defects have been introduced in the CIGS layer, with similar characteristics and densities as the defects observed by admittance spectroscopy from the different samples. IV curves show a deterioration of photovoltaic parameters as the density of the defects increases on the CIGS layer, as can be seen in Figure 2. This figure shows a decrease in both V_{oc} and J_{sc} (with a relative decrease of 27% and 44% of both parameters) that is directly related to the presence of defect D_2. Similar quantitative results are obtained for defect D_1. This gives strong interest in the early detection of these defects.

Figure 3 shows the typical Raman spectrum measured in the 100–250 cm^{-1} region of a sample corresponding to devices with the lowest densities of defects. Raman spectra have also been measured on unetched cells, focusing the laser spot through the window and buffer layers. The spectra measured from both HCl etched and unetched samples are very similar and show the same behavior with the density of defects D_1 and D_2 detected by admittance spectroscopy. This allows us to rule out the potential presence of HCl etching effects in the reported measurements. The spectrum is characterised by a dominant peak centered at about 175 cm^{-1} that corresponds to the main A_1 Raman mode from CIGS. As already reported, the frequency of this peak depends linearly on the Ga/(In + Ga) relative content in the CIGS alloy.[15] The spectrum also shows additional weaker peaks in the 210–230 cm^{-1} spectral region that are identified with E/B_2 and E/B_1 symmetry modes. Detection of these weaker modes in the spectra suggests a high crystalline

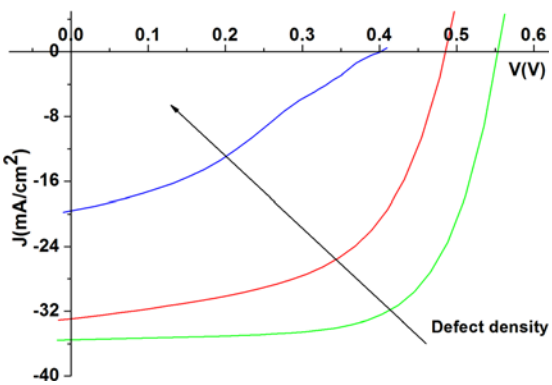

FIG. 2. Simulated JV curves for different D_2 defect densities.

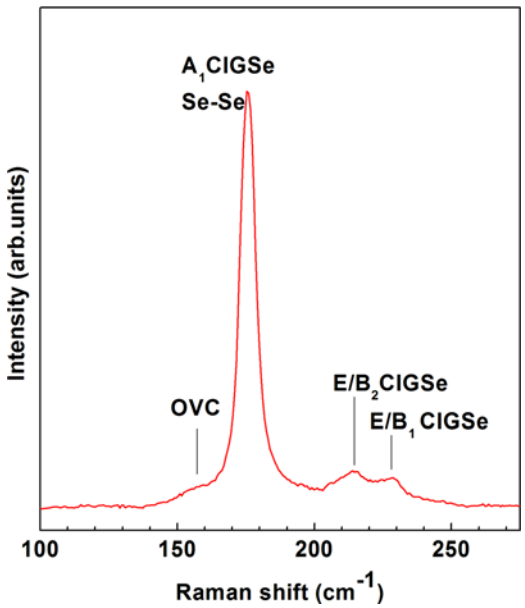

FIG. 3. Raman spectrum from a CIGS absorber corresponding to cells with lower point defect densities, showing A_1 and E/B CIGS peaks and OVC contribution at 150 cm^{-1} spectral region.

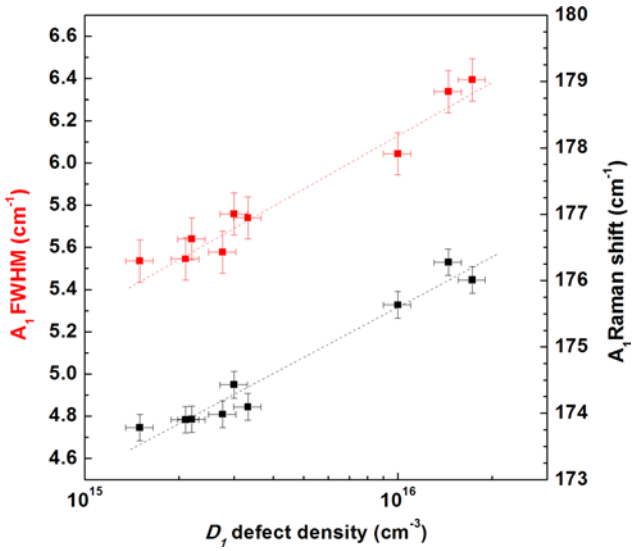

FIG. 4. Frequency (black squares) and FWHM (red circles) of the main A_1 CIGS peak in the Raman spectra versus density of defect D_1. Dashed lines are included as guide for the eye.

quality of the absorbers, in spite of the presence of the electronic defects identified by the electrical measurements. In addition, there is a shoulder in the 150–160 cm^{-1} spectral region, which has been identified with the main vibrational mode from a Cu-poor ordered vacancy compound (OVC) phase.[16] OVC phases are closely related to the chalcopyrite-type structure and can be derived by randomly introducing in the lattice complex defects in the form of In_{Cu} antisites and Se vacancies (V_{Se}^{2-}) and imposing the preservation of the charge neutrality in the lattice. Formation of these phases is favoured by the existence of a Cu-poor composition of the films, which has been assessed by quantitative inductive coupled plasma (ICP) measurements. According to these measurements, the final Cu/(Ga + In) content in the absorbers ranges from 0.8 (for samples with the lowest density of D_2 defect) up to 0.95 (for samples with the highest density of D_2 defect). In principle, penetration depth of scattered light in the absorbers is of the order of 100 nm. This implies that detected OVC phases are located at the surface region of the layers and agrees with the depth of the space charge region where the DOS profiles are measured. Detection of the OVC phase at greater depths would require the use of higher excitation wavelengths with longer penetration depth.

The spectral features analysis of the main A_1 CIGS peak has enabled the observation of a blue shift (towards higher values) of the frequency and an increase in the FWHM with the increase in the density of defect D_1, as shown in Figure 4. External quantum efficiency (EQE) measurements performed in the cells with different defect densities give a roughly constant value of the bandgap of the order of 1.04 eV ± 0.02 eV. This contrasts with the estimation of the bandgap assuming that the blue shift of the Raman peak is due to changes in the Ga/(In + Ga) relative content, which gives values between 1.01 eV and 1.30 eV. This allows the exclusion of the presence of effects related to different Ga contents in the changes of the spectral features of the A_1 peak from the different samples.

Accordingly, the blue shift and broadening of the A_1 peak have been directly related to the presence of the D_1 defect. The broadening of the peak with the increasing density of Se vacancies is related to the decrease of the phonon lifetime for higher defect densities, as the phonon lifetime is inversely proportional to the FWHM of the corresponding peak.[6,17] Presence of these point defects in the scattering volume also indicates a relaxation of the momentum conservation rule in the crystal, enabling the activation of phonons with non-zero wave vector.[18] Because of the positive slope of the phonon dispersion curve in the vicinity of the Γ point of the Brillouin zone,[19] this leads to the observed blue shift of the peak and contributes to an asymmetric broadening of the peak with the increase of the density of defects. In addition, stress effects in the CIGS lattice can also partially contribute to the observed blue shifts of the Raman peak.

This behavior contrasts with that observed for samples with different densities of defect D_2, where no significant changes are observed in the spectral features of the main A_1 Raman peak. This can be observed in Figure 5, where the spectra corresponding to the absorbers with the lower (5×10^{15} cm^{-3}) and higher ($\geq 8 \times 10^{15}$ cm^{-3}) D_2 defect densities are plotted. Main differences related to these spectra are located in the spectral region corresponding to the OVC secondary phase contribution: as can be observed, increasing the density of defect D_2 to values higher than 5×10^{15} cm^{-3} leads to a significant decrease of the relative intensity of this contribution. This indicates that synthesis conditions favoring formation of the D_2 defect (which is likely related to Cu-excess in the lattice) also lead to an inhibition in the formation of the Cu-poor OVC secondary phase. This is also accompanied by a shift of this contribution towards higher frequencies with the increase of the content of the D_2 defect, as shown in the inset of Figure 5. This suggests that the decrease in the occurrence of the OVC phase is also accompanied by the formation of OVC phases with higher Cu/In

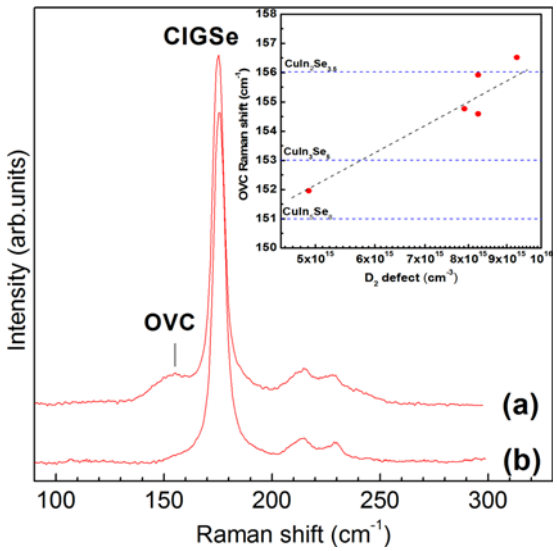

FIG. 5. Raman spectra from absorber layers corresponding to cells with different densities of D_2 defect: (a) D_2 defect density $4.9 \times 10^{15}\,cm^{-3}$, (b) D_2 defect density $\geq 9.3 \times 10^{15}\,cm^{-3}$. In the inset, the evolution of the OVC peak position is plotted vs the D_2 defect density for the analyzed samples. Frequency positions of the main Raman peak from different OVC phases are also included in the inset.[16]

content ratios,[16] which leads to a decrease in the amount of In_{Cu} antisites and Se vacancies (V_{Se}^{2-}) present in the phase. This decrease in the occurrence of the OVC phase correlates with the increase in the occurrence of the D_2 defect, and with the increase in the relative Cu/(Ga + In) relative content in the absorbers as, measured by ICP (that ranges from 0.8 for samples with the highest spectral OVC contribution up to 0.95 for samples with the lowest OVC spectral contribution). In this sense, monitoring of the relative spectral OVC contribution can give indirect qualitative information about the possible occurrence of defects related to Cu-excess inhomogeneities in the layers. In addition, it is interesting to remark that the presence of a surface OVC phase in the absorbers is also believed to have a beneficial effect on the characteristics of the devices, leading to a better band alignment at the buffer/CIGS interface.[20]

In conclusion, combining the electrical and Raman scattering analysis of CIGS electrodeposited cells has allowed characterization of the impact of the presence of Se and Cu related electronic defects on the Raman spectra. In particular, we have observed a direct correlation between the density of a defect at 100 meV that has been previously identified with Se vacancies and a blue shift and broadening of the main A1 Raman peak, being sensitive to in the presence of defect densities higher than $10^{15}\,cm^{-3}$. These results have been related to the decrease of the phonon lifetime and the appearance of disorder effects in the spectra breaking the momentum conservation rule as a consequence of the presence of the vacancies. Presence of a Cu related defect at 210 meV has also been observed to determine a significant inhibition in the relative intensity of the spectral contribution from OVC secondary phases at the surface of the absorbers. These data corroborate the potential of Raman scattering for the indirect detection at early process stages of layer inhomogeneities related to the presence of point defects that are relevant for device performance.

The research leading to these results has received funding from the People Programme (Marie Curie Actions) of the European Union's Seventh Framework Programme FP7/2007-2013/ under REA grant agreement n285897 (INDUCIS). Authors from IREC and the University of Barcelona belong to the M-2E (Electronic Materials for Energy) Consolidated Research Group and the XaRMAE Network of Excellence on Materials for Energy of the "Generalitat de Catalunya". V.I.R. thanks the MINECO, Subprogram Juan de la Cierva (ref. JCI-2011-10782).

[1]P. Jackson, D. Hariskos, E. Lotter, S. Paetel, R. Wuerz, R. Menner, W. Wischmann, and M. Powalla, Prog. Photovoltaics **19**(7), 894–897 (2011).
[2]M. A. Green, K. Emery, Y. Hishikawa, W. Warta, and E. D. Dunlop, Prog. Photovoltaics **20**, 606 (2012).
[3]P. Zabierowski, R. Bacewicz, N. Barreau, and A. Hultqvist, in *2011 37th IEEE Photovoltaic Specialists Conference (PVSC)* (2011), pp. 2–6.
[4]P. Zabierowski, K. Stankiewicz, A. Donmez, F. Couzinie-Devy, and N. Barreau, Thin Solid Films **519**, 7485 (2011).
[5]E. Rudigier, T. Enzenhofer, and R. Scheer, Thin Solid Films **480–481**, 327 (2005).
[6]V. Izquierdo-Roca, X. Fontané, E. Saucedo, J. S. Jaime-Ferrer, J. Álvarez García, A. Pérez-Rodríguez, V. Bermudez, and J. R. Morante, New J. Chem. **35**, 453 (2011).
[7]C. Broussillou, M. Andrieux, M. Herbst-Ghysel, M. Jeandin, J. Jaime-Ferrer, S. Bodnar, and E. Morin, Sol. Energy Mater. Solar Cells **95**, S13 (2011).
[8]T. Walter, R. Herberholz, C. Müller, and H. W. Schock, J. Appl. Phys. **80**, 4411 (1996).
[9]T. Sakurai, M. M. Islam, H. Uehigashi, S. Ishizuka, A. Yamada, K. Matsubara, S. Niki, and K. Akimoto, Sol. Energy Mater. Sol. Cells **95**, 227 (2011).
[10]M. Burgelman, P. Nollet, and S. Degrave, Thin Solid Films **361–362**, 527 (2000).
[11]M. Burgelman and J. Marlein, in *23rd European Photovoltaic Solar Energy Conference* (2008), pp. 1–5.
[12]M. Burgelman, J. Verschraegen, S. Degrave, and P. Nollet, Prog. Photovoltaics **12**, 143 (2004).
[13]C. M. Ruiz and V. Bermúdez, in *2009 34th IEEE Photovoltaic Specialists Conference (PVSC)* (2009), pp. 301–304.
[14]K. Decock, S. Kheli, and M. Burgelman, Thin Solid Films **519**(21), 7481–7484 (2011).
[15]R. Scheer, A. Perez-Rodriguez, and K. M. Wyatt, Prog. Photovoltaics **18**, 467 (2010).
[16]C.-M. Xu, X.-L. Xu, J. Xu, X.-J. Yang, J. Zuo, N. Kong, W.-H. Huang, and H.-T. Liu, Semicond. Sci. Technol. **19**, 1201 (2004).
[17]V. Izquierdo-Roca, A. Pérez-Rodríguez, J. R. Morante, J. Álvarez-García, L. Calvo-Barrio, V. Bermudez, P. P. Grand, L. Parissi, C. Broussillon, and O. Kerrec, J. Appl. Phys. **103**, 123109 (2008).
[18]C. Camus, E. Rudigier, D. Abou-Ras, N. A. Allsop, T. Unold, Y. Tomm, S. Schorr, S. E. Gledhill, T. Köhler, J. Klaer, M. C. Lux-Steiner, and C.-H. Fischer, Appl. Phys. Lett. **92**, 101922 (2008).
[19]J. Lazewski, P. T. Jochym, and K. Parlinski, J. Chem. Phys. **117**, 2726 (2002).
[20]A. Niemegeers, M. Burgelman, R. Herberholz, U. Rau, D. Hariskos, and H.-W. Schock, Prog. Photovoltaics **6**, 407 (1998).

Progress in PHOTOVOLTAICS

PROGRESS IN PHOTOVOLTAICS: RESEARCH AND APPLICATIONS
Prog. Photovolt: Res. Appl. (2014)
Published online in Wiley Online Library (wileyonlinelibrary.com). DOI: 10.1002/pip.2473

RESEARCH ARTICLE

Secondary phase formation in Zn-rich $Cu_2ZnSnSe_4$-based solar cells annealed in low pressure and temperature conditions

Andrew Fairbrother[1], Xavier Fontané[1], Victor Izquierdo-Roca[1], Marcel Placidi[1], Dioulde Sylla[1], Moises Espindola-Rodriguez[1], Simón López-Mariño[1], Fabian A. Pulgarín[2], Osvaldo Vigil-Galán[3], Alejandro Pérez-Rodríguez[1,4] and Edgardo Saucedo[1]*

[1] Solar Energy Materials and Systems Laboratory, IREC, Catalonia Institute for Energy Research, Barcelona, Spain
[2] Centro de Investigación en Energía, Universidad Nacional Autónoma de México, Temixco, Mexico
[3] Escuela Superior de Física y Matemáticas-Instituto Politécnico Nacional (IPN), México DF, Mexico
[4] IN^{2}UB, Department d'Electrònica, Universitat de Barcelona, Barcelona, Spain

ABSTRACT

Zn-rich $Cu_2ZnSnSe_4$ (CZTSe) films were prepared by a two-step process consisting in the DC-magnetron sputtering deposition of a metallic stack precursor followed by a reactive anneal under a Se + Sn containing atmosphere. Precursor composition and annealing temperature were varied in order to analyze their effects on the morphological, structural, and optoelectronic properties of the films and solar cell devices. Raman scattering measurements show the presence of ZnSe as the main secondary phase in the films, as well as the presence of SnSe at the back absorber region of the films processed with lower Zn-excess values and annealing temperatures. The ZnSe phase is found to accumulate more towards the surface of the absorber in samples with lower Zn-excess and lower temperature annealing, while increasing Zn-excess and annealing temperature promote its aggregation towards the back absorber region of the devices. These measurements indicate a strong dependence of these process variables in secondary phase formation and accumulation. In a preliminary optimization of both the composition and reactive annealing process, a solar cell with 4.8% efficiency has been fabricated, and potential mechanisms limiting device efficiency in these devices are discussed. Copyright © 2014 John Wiley & Sons, Ltd.

KEYWORDS

CZTSe; Zn-excess; secondary phases; zinc selenide; tin selenide; Raman spectroscopy

***Correspondence**

Edgardo Saucedo, Solar Energy Materials and Systems Laboratory, IREC, Catalonia Institute for Energy Research, Barcelona, Spain.
E-mail: esaucedo@irec.cat

Received 27 November 2012; Revised 2 July 2013; Accepted 16 December 2013

1. INTRODUCTION

Kesterite semiconductors, such as $Cu_2ZnSn(S,Se)_4$ (CZTS,Se), have received increasing interest as a photovoltaic absorber layer due to promising results obtained in the past decade, especially for the pentenary sulfo-selenide compounds [1–5]. CZTS,Se exhibits p-type conductivity and has an absorption coefficient on the order of 10^4–10^5 cm^{-1} [6]. These properties, in addition to its band gap of between 1.0 eV (CZTSe) and 1.5 eV (CZTS) [6], make it an ideal candidate as a thin film photovoltaic absorber. The key advantage of these materials with respect to more mature thin film solar cell absorbers like $Cu(In,Ga)Se_2$ and CdTe is that CZTS,Se is composed of more abundant and lower toxicity elements [7], and thus more aptly suited for mass production. Nevertheless, these materials are still at an incipient state of development, with a maximum device efficiency of 11.1% at the laboratory scale [8], which, while promising, is still far from the record cell efficiencies of above 20% and 16% for $Cu(In,Ga)Se_2$ and CdTe, respectively [6].

Because of the complexity of this material system, even small compositional variations or inhomogeneities are expected to have a strong influence on the properties of the final film, with secondary phases typically limiting the performance of the absorber layer. There is a general agreement that Zn-rich conditions are beneficial [1–5,8,9], because they may improve p-type conductivity and prevent

the formation of the ternary $Cu_2Sn(S,Se)_3$ (CTS,Se) compound, which can limit V_{OC} because of its lower band gap (0.84 eV for CTSe) [10], even though Zn-excess increases the risk of forming the n-type Zn(S,Se) binary phase. Nonetheless, under non-stoichiometric conditions, secondary phase formation becomes inevitable, thus it is also desirable to control the segregation of these phases in a manner in which they may be removed (i.e., via chemical etching) [11] or have a minimized effect on the absorber properties.

Characterization of kesterite films is an additional challenge specific to these systems because some of the main secondary phases are not readily distinguishable from one another using traditional methods such as x-ray diffraction (XRD). This is the case for CZTSe, CTSe and ZnSe phases, which has led to the rise of Raman spectroscopy as an important characterization technique for this material system. While the spectra of the main secondary phases still overlap with CZTSe in some cases, the greatest advantage is the ability to use different excitation wavelengths, which may potentially lead to pre-resonant Raman scattering if the excitation wavelength is closely matched to a fundamental energy transition of a particular phase, greatly increasing the signal of that phase. For ZnSe ($E_g = 2.7$ eV) this occurs with an excitation of about 457.9 nm, and permits the detection of even miniscule amounts of this phase [12].

The majority of research published up to now is devoted to the study of pure sulfide or sulfo-selenide kesterite systems [1–3,8]. In fact, while the record efficiency for the sulfo-selenide compound is 11.1% [8] and for the sulfide is 9.2% [2], in the case of the pure selenide compound it was much lower (3.2%) [13] until somewhat recently. The currently reported record of 9.2% was prepared by a single step co-evaporation process [4]. With careful control of the deposition rates and substrate temperature Repins *et al.* [4] were able to prevent the evaporation of volatile phases and greatly improve on the previous record efficiency for CZTSe and vacuum based techniques. These results and the fact that record device efficiencies have been obtained with Se-rich compositions give increased motivation for the study of the selenide system. A deeper understanding of the characteristics of this system is an important issue in order to improve the knowledge of these technologies and to identify the mechanisms limiting efficiency in selenium-rich record devices. Furthermore, devices based on pure selenium systems have additional interest related to their potential for higher current devices when compared with sulfide systems due to their smaller bandgap, albeit with lower V_{OC}: record $J_{SC} = 37.4$ mA/cm^2 for CZTSe [4] versus 21.6 mA/cm^2 for CZTS [2] and 35.0 mA/cm^2 for CZTS,Se (Se-rich) [9], and compared with V_{OC} of the same devices, 377, 708, and 460 mV, respectively.

In this work, we present a systematic study of $Cu_2ZnSnSe_4$ films prepared by a two-stage process as a function of precursor film Zn-excess concentration and reactive annealing temperature. This is done using a low total pressure thermal treatment, in order to protect the Mo back contact, which can be greatly affected by higher pressure and temperature treatments when using two-step processes. These processes commonly lead to the formation of a relatively thick $MoSe_2$ interfacial layer between the absorber and the back Mo contact layer, which can lead to decrease in device performance [5,14]. We show the importance of the accurate control of both parameters (composition and annealing temperature), which are significant determining factors for the optoelectronic properties of CZTSe devices. ZnSe is detected as the main secondary phase, and accumulation of this phase towards the surface or back absorber regions is significantly affected by the two process variables. With these preliminary results, we have obtained a maximum cell efficiency of 4.8% by using a relatively low temperature process (compare with, e.g, [4,5,14]) and identify potential mechanisms limiting the performance of the cells.

2. EXPERIMENTAL

Sn, Cu, and Zn films were sequentially deposited by DC-magnetron sputtering deposition (Ac450 Alliance Concepts) using 99.99% purity targets in Zn-excess and Cu-deficient conditions, as shown in Table I. The Zn layer was fixed at about 230 nm thickness, and the thickness of the other layers adjusted to achieve the desired compositional ratios. The substrate was 10×10 cm^2 Mo-coated soda-lime glass approximately 500 nm thick with a sheet resistance of 0.25 Ω/□. The depositions were carried out in a 1×10^{-3} mbar Ar atmosphere at 30 sccm flow, using power densities of 0.64 W/cm^2 for Sn and 1.27 W/cm^2 for Cu and Zn. The substrate/Sn/Cu/Zn stack order was selected in an effort to minimize Sn evaporation [9] and to promote the segregation of Zn-rich phases towards the surface, where they can be more easily removed by suitable etching processes [11]. The thickness and composition of the stacks were measured by X-ray fluorescence spectroscopy (Fischerscope XVD), which had been calibrated with inductively coupled plasma mass spectroscopy measurements. The topography of each precursor layer was imaged by tapping mode atomic force microscopy (AFM) (Park Systems XE-100).

Samples of the metallic precursors (2×2 cm^2 in area) were reactively annealed in a tubular furnace capable of working in vacuum (10^{-4} mbar) or an inert gas (Ar) atmosphere. A graphite box (23.5 cm^3 in volume) with crucibles containing Se powder (50 mg, Alfa Aesar 99.999% purity) and Sn powder (5 mg, Alfa Aesar 99.999%) was used for

Table I. Compositional ratios and total thickness of precursor stacks used in this study.

Precursor name	Zn/Sn	Cu/(Zn+Sn)	Total thickness (nm)
SnCuZn-1	1.24	0.77	814
SnCuZn-2	1.40	0.84	835
SnCuZn-3	1.49	0.87	798
SnCuZn-4	1.73	0.67	688

the reactive annealing. While elemental Sn and Se are placed in the annealing box, upon heating, they evaporate and react with the precursor film or each other to form Sn–Se binary phases. This means that while the initial annealing atmosphere contains elemental Sn and Se, within a short time, they form compounds based on Sn–Se. Nonetheless, Sn–Se phases are also volatile at these temperatures and serve as a chalcogen source to react with the film and form the desired CZTSe phase. After purging the tube with Ar, the system was brought under vacuum and the Ar flow increased until a stable working pressure of 1–2 mbar was obtained. The annealing temperature was set between 425°C and 550°C with a ramp rate of 20°C/min. After 45 min at the selenization temperature, the furnace was left to naturally cool to room temperature (approximately 2–3 h).

To fabricate solar cell devices, each sample was etched in 10% v/v HCl for 5 min at 75°C in order to remove superficial ZnSe phases [11]. It is important to note that this etching process has been demonstrated as effective for the removal of superficial ZnS from CZTS films, and its effectiveness at removing ZnSe is more limited. Next, a film of CdS (60 nm) was deposited by chemical bath deposition, followed immediately by pulsed DC-magnetron sputtering deposition of undoped ZnO (50 nm) and ZnO:Al (450 nm, 19 Ω/□ sheet resistance) (CT100 Alliance Concepts). For the optoelectronic characterization, 3×3 mm^2 cells were scribed using a micro-diamond scriber (MR200 OEG), thus avoiding the necessity of metallic grid deposition onto the ZnO:Al surface. Measurement of the optoelectronic properties was carried out using a Sun 3000 Class AAA solar simulator from Abet Technologies (uniform illumination area of 15×15 cm^2).

Selected absorbers were characterized by scanning electron microscopy (SEM), energy-dispersive X-ray spectroscopy (EDX), and Raman scattering spectroscopy. SEM images were taken using a Zeiss Series Auriga field emission scanning electron microscope. EDX elemental mappings were made with 10 kV acceleration voltage using an Oxford Instruments X-Max detector directly on the back absorber surface from films that were mechanically removed from the substrate by using double-sided tape to peel them off [15]. This usually results in a clean cleavage at the Mo/CZTSe interface, as evidenced by Raman scattering measurements, which show a lack of CZTSe characteristic peaks on the substrate, and a lack of $MoSe_2$-related peaks at the back region of the absorber layer after removal. Characterization by Raman spectroscopy was carried out with a T64000 Horiba-Jobin Yvon spectrometer with 457.9 nm, and 514.5 nm excitation wavelengths in micro- and macro-configurations. Scattered light penetration depth in CZTSe is estimated to be below 100 nm for these wavelengths. Raman spectroscopy with a 457.9 nm laser is particularly useful for identification of the ZnSe phase because it is in pre-resonant conditions [12], while with lower energy excitation, it is more difficult to distinguish between the contributions from the main CZTSe phase and a ZnSe secondary phase because of the proximity between the main ZnSe Raman peak and CZTSe characteristic ones. For the micro-configuration setup, the spot diameter is approximately 1 μm, and for the macro setup it is 100 μm. The macro-configuration was used to characterize the surface of the absorbers, and for measurements with the micro-configuration, the films were mechanically removed from the substrate so that the back absorber and substrate regions could be characterized [15].

3. RESULTS

Atomic force microscopy images of the precursor stacks shows relatively smooth and uniform deposition of Cu and Zn onto a glass or Mo substrate (average roughness (R_a) of a few to tens of nanometers depending on substrate and thickness). However, Sn films deposited onto Mo are much rougher ($R_a = 165$ nm for a 330 nm thick film), and subsequently deposited layers of Cu and Zn take on the morphology of the underlying Sn layer, as shown in Figure 1 ($R_a = 138$ nm for complete stack of precursor with Zn/Sn = 1.24). The rough morphology of Sn films deposited by physical vapor deposition methods has been noted in other works as well [16,17] and shown to have significant effects on the absorber properties.

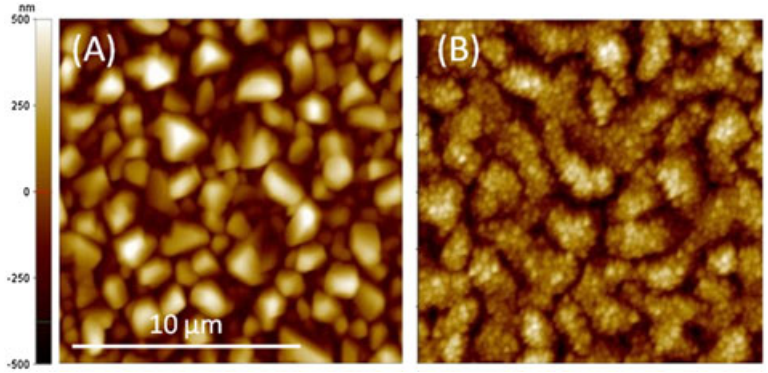

Figure 1. Atomic force microscopy topographical image of Sn film deposited onto a glass/Mo substrate (A) and glass/Mo/Sn/Cu/Zn precursor stack (Zn/Sn = 1.24) (B).

The morphology and grain size of the CZTSe absorber films as seen by SEM depends strongly on both the annealing temperature and precursor composition. Figure 2 (A), (B), and (C) shows the SEM cross sectional images of the complete cells fabricated with the first precursor stack (Zn/Sn = 1.24) and annealed at different temperatures. The grain size clearly increases with annealing temperatures from about 500 nm at 450°C up to 2 μm at 550°C. However, increasing the temperatures leads to a deterioration of the morphology of the Mo/CZTSe back absorber region, as voids are formed, which are detrimental to the optoelectronic properties and mechanical robustness of the cell. The size of these voids matches closely with the larger features seen in the Sn films by AFM, thus we attribute the formation of these voids to the diffusion and evaporation of Sn and SnSe, which becomes more probable at higher temperatures, as evidenced by subsequent Raman scattering measurements. Some of these voids may also be related to the decomposition of CZTSe in contact with the Mo back contact [14], and is suggested by the accumulation of ZnSe seen in these regions by Raman and EDX measurements. Increasing the Zn-excess in the precursor leads to the formation of a bilayer grain structure as seen in Figure 2(D) and (E) for films annealed at 450°C with precursors containing Zn/Sn = 1.40 and 1.49, respectively. In the front of the film, a grain size similar to that seen with the lowest Zn-excess is seen, while in the back absorber region smaller nanometric grains form. This back region becomes proportionally larger with respect to the upper one with increasing Zn excess. In fact, with the highest Zn-excess the entire film is composed of these small grains, as seen in Figure 2(F). The cause of the formation of this nanometric bilayer grain structure is not entirely clear, as it may be related to the varied Cu-deficient or Zn-excess conditions. Cu-excess/deficiency has been shown to affect the grain growth in CZTS,Se thin films [18,19], and each precursor has a varied Cu/(Zn + Sn) ratio (0.67–0.87). However, Zn/Sn ratios are varied over a much larger range (1.24–1.73) and may also have a significant effect on grain growth, though we have found no reports focusing on this effect in CZTSe films.

It is also important to remark that by using this low pressure thermal process, the Mo back contact is affected a little, indicating that this "soft" thermal treatment is effective in protecting the back region, avoiding the formation of a thick $MoSe_2$ layer. In other works, by using high pressure thermal treatments, the Mo layer is significantly affected, with the formation of very thick $MoSe_2$ layers [5,14]. In this case, because of the low background pressure used during annealing, a thin $MoSe_2$ layer is observed (and confirmed later by Raman spectroscopy), and independently of the annealing temperature and precursor composition, the thickness of this layer is estimated by SEM to be less than 50 nm. This low pressure process is attractive because it may avoid the necessity of using a chemical barrier for Se (such as TiN [5]), thus simplifying the technology. Also, by working at lower temperatures, the energy consumption and velocity of the thermal process could be remarkably improved.

To determine the impact of composition and annealing temperature on the structural properties of the absorbers, Raman spectroscopy measurements have been carried out on selected absorbers. Figure 3 shows the macro-Raman spectra measured with an excitation wavelength of 514.5 nm on the surface of the absorbers from the same precursor composition (Zn/Sn = 1.24) and annealed at different temperatures (450°C, 500°C, and 550°C). Also shown is a spectrum of Cu_2SnSe_3 (CTSe) synthesized from a Sn/Cu stack selenized at 450°C for comparative purposes. The spectra are characterized by the presence of two main peaks at 196 and 173 cm^{-1} identified as the main peaks of CZTSe [20–22], as well as weaker CZTSe characteristic peaks at about 233 and 244 cm^{-1}. Fitting of the spectra also shows a contribution at about

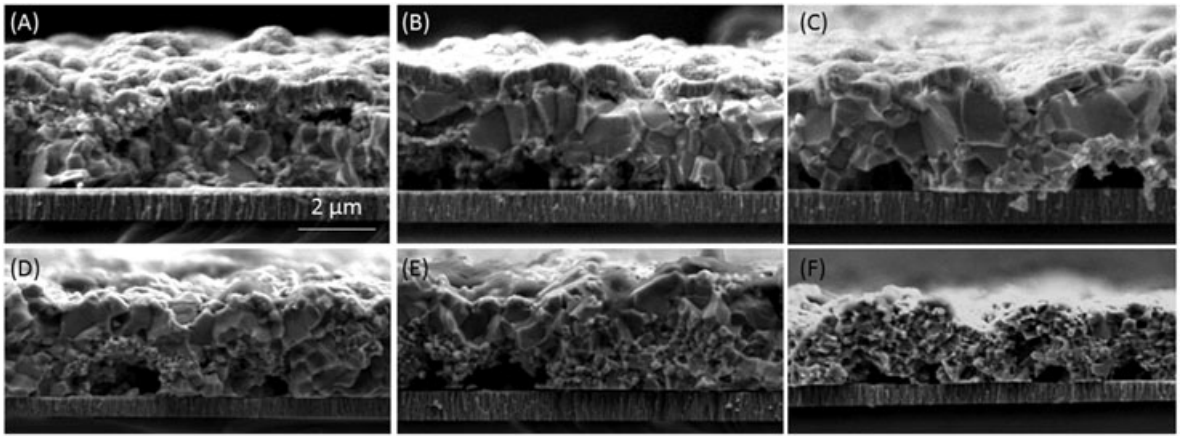

Figure 2. Cross sectional scanning electron microscopy micrographs for devices fabricated from precursor with Zn/Sn = 1.24 and selenized at 450°C (A), 500°C (B), and 550°C (C), and films annealed at 450°C with precursors with Zn/Sn = 1.40 (D), 1.49 (E), and 1.73 (F). Grain size increases with temperature, but the back absorber region degrades. Conversely, grain size decreases with increasing Zn-excess.

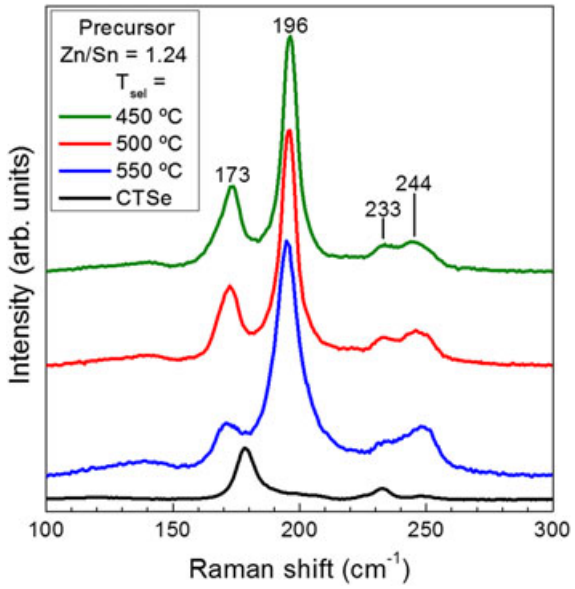

Figure 3. Surface Raman spectra of CZTSe films using precursor with Zn/Sn = 1.24 and annealed at different temperatures; also shown is a CTSe reference spectra for comparison (514.5 nm excitation, macro-configuration).

248–250 cm^{-1} that has been attributed to the main Raman peak of ZnSe [12,15], As shown later, this has been confirmed by Raman scattering measurements performed with 457.9 nm excitation wavelength. Increasing the annealing temperature leads to a slight red shift of the main CZTSe mode (from 196.2 to 195.3 cm^{-1}) and to an increase of the full width at half maximum (from 7.1 to 11.4 cm^{-1}). Similarly, broad CZTSe peaks are observed in [14] and are related to the decomposition of CZTSe at high temperatures, though those measurements were from samples prepared under a high pressure thermal process. These features could additionally be related to stress and/or disorder effects related to a higher density of point or extended defects at the surface region of the absorbers, or even the localized surface formation of CTSe at this temperature. However, even if the possibility of overlapping with CTSe peaks cannot be ruled out, we expect the relatively Sn-poor conditions to limit the formation of this phase. Changes in the surface Raman spectra due to composition at 450°C are less significant, and surface Raman spectra with 514.5 nm excitation are very similar (not shown).

By using 457.9 nm excitation, significant differences are observed in the samples in the surface region of the absorbers, as shown in Figure 4. First (250 cm^{-1}) and second order (about 498 cm^{-1}) peaks characteristic of ZnSe are clearly detected on the surface of all samples (a reference spectrum from a ZnSe sample (ABCR 99.995%) is also shown). The strong increase in the intensity of the ZnSe main peak at 250 cm^{-1} and the appearance of the second order peak are due to the existence of pre-resonant excitation conditions of these modes with the 457.9 nm wavelength and permit a very sensitive detection of this secondary phase. With increasing annealing temperature, the intensity of the ZnSe peaks decreases (Figure 4(A)). This is attributed initially to the diffusion of ZnSe towards the back absorber region, promoted by the higher annealing temperature, as evidenced later by EDX mapping measurements. The effect of the annealing process on Zn-rich phase accumulation has been noted in other works as well, such as [2] for the case of CZTS. For samples annealed at the same temperature, increasing the Zn-excess also leads to a decrease of the amount of ZnSe detected on the surface (Figure 4(B)), except for the sample grown with the highest Zn-excess in which the amount of ZnSe is comparable with that from the sample with lowest Zn-excess. This indicates that the amount of excess Zn also affects the formation and accumulation of ZnSe in the films, with higher excess promoting aggregation towards the back absorber region. In the case of the sample with the highest Zn-excess, the presence of ZnSe is expected to be more uniform throughout the film due to the high amount of Zn present (precursor Zn/Sn = 1.73) and lower film thickness (Figure 2(F)). In principle, presence of ZnSe

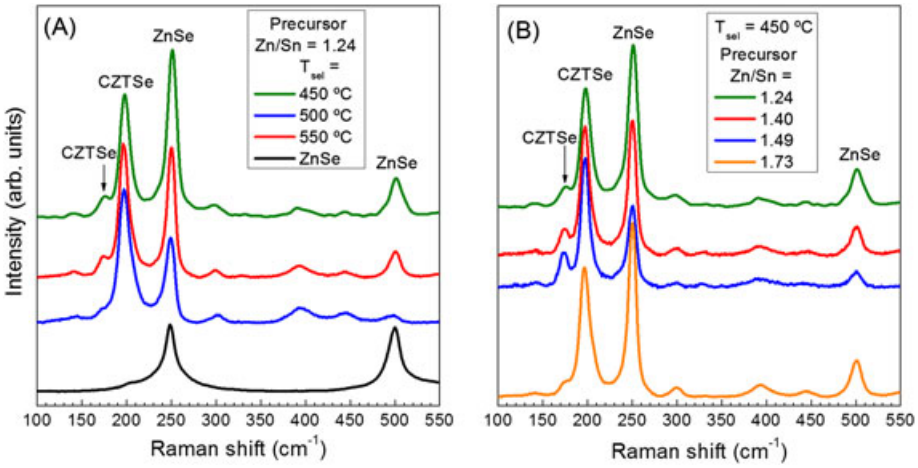

Figure 4. Surface Raman spectra of CZTSe films varying temperature (A) and Zn/Sn ratio annealed at 450°C (B); also shown in (A) is a reference spectrum of ZnSe (457.9 nm excitation, macro-configuration).

(n-type conductivity) on the surface of the absorber may be preferable because it could be removed more easily by a suitable etching process or it may even improve the p–n junction properties formed with the CdS layer. On the other hand, accumulation in the back absorber region could lead to the formation of an inverted p–n junction, with a subsequent deterioration of the optoelectronic properties of the devices.

Micro-configuration Raman scattering measurements directly performed in the back surface of the absorbers after mechanical removal of the films from the Mo-coated substrates confirm the presence of secondary phases in the back absorber region. With 514.5 nm excitation wavelength peaks characteristic of the SnSe phase are detected, as shown in Figure 5(A), with several peaks present: 35, 69, 106, 129, and 150 cm^{-1}. A reference spectrum of a SnSe powder sample (Alfa Aesar 99.999%) is also shown for comparison. This phase was only detected in the back region of samples with the lower Zn-excess values ($Zn/Sn \leq 1.40$) and processed at lower temperatures ($T_{sel} \leq 500°C$). This phase may be expected to form at the back region because of the poor uniformity of the sputtered Sn precursor layer as seen by AFM (Figure 1). In fact, the SnSe phase is only detected in certain points of the back region as seen in spectra taken at two distinct points shown in Figure 5(A), indicating that it is non-uniformly distributed. Also, the fact that this phase is not detected in samples with higher Zn-excess or annealing temperatures suggests that Sn-rich secondary phases are not readily formed under such conditions, or more readily diffuse towards the surface and volatilize. Also with a 514.5 nm excitation wavelength, the Raman peaks characteristic of $MoSe_2$ are also detected in the spectra directly measured on the substrate region from all the samples (spectra not shown).

With 457.9 nm excitation ZnSe is detected in the back absorber region of all samples (Figure 5(B)), and as with SnSe, it is unevenly distributed. Because of the non-uniform distribution of these phases, EDX elemental mapping measurements were performed on the back absorber region using low accelerating voltage (10 kV) to perform a relatively superficial measurement, shown in Figure 6. Accumulations of Sn are detected in samples with lower Zn-excess and annealing temperatures (Figure 7(A)). This accumulation is attributed to the presence of the SnSe phase, corresponding with Raman scattering measurements (Figure 5). Additionally, there are agglomerations of Zn in all samples. The locations of these agglomerations correspond with Raman measurements in which significant quantities of ZnSe are detected (Figure 5), thus excess Zn detected by EDX is shown to form as part of the ZnSe phase. It is interesting to note that the accumulation of Zn is found in regions in which voids have been formed. With increasing annealing temperature, the quantity of Zn in the back absorber region increases notably (comparison between Figure 6(A) and (B)). The same is also true to a lesser extent for the sample with high Zn-excess (comparison between Figure 6(A) and (C)). The average Zn concentration estimated from various EDX mappings agrees with this tendency, with Cu/Zn ratios compared with bulk measurements from X-ray fluorescence spectroscopy indicating increased accumulation of Zn in the back absorber region in samples with higher annealing temperature and precursor Zn-excess. In conjunction with Raman measurements of the surface with 457.9 nm excitation, this provides significant evidence that both increasing annealing temperature and precursor Zn-excess promote Zn/ZnSe accumulation towards the back absorber region of the CZTSe films, confirming the importance to develop

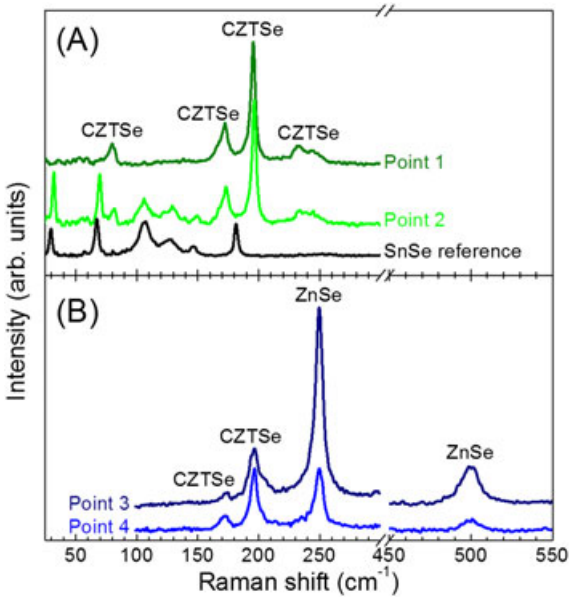

Figure 5. Raman spectra at different points of the back region of film with precursor Zn/Sn = 1.24 and selenized at 450°C, showing the non-uniform distribution of the SnSe (point 1, 2, and SnSe reference, 514.5 nm excitation) (A), and ZnSe phases (point 3 and 4, 457.9 nm excitation) (B).

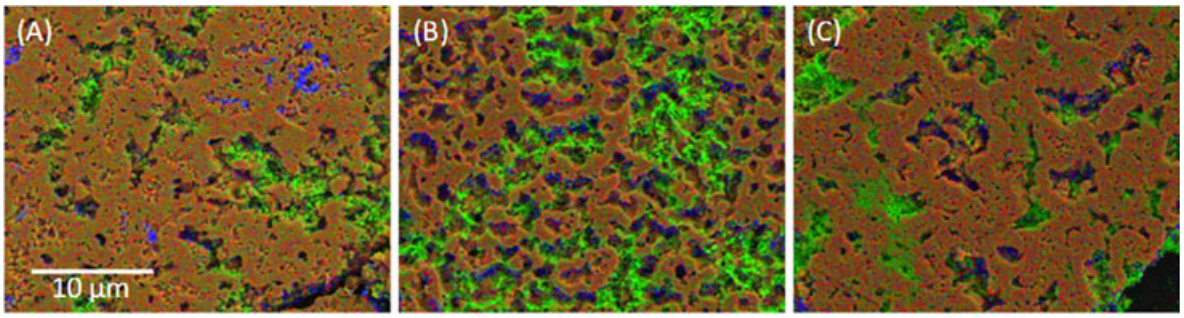

Figure 6. Energy-dispersive X-ray elemental mappings of the back of absorbers with precursor Zn/Sn = 1.24 annealed at 450°C (A), and 550°C (B), and sample with precursor Zn/Sn = 1.73 annealed at 450°C (C). The mapped elements are Cu (red), Zn (green), and Sn (blue), showing clear agglomerations of Zn and Sn in the back which, corresponding to Raman scattering measurements, are attributed to the presence of the ZnSe and SnSe phases.

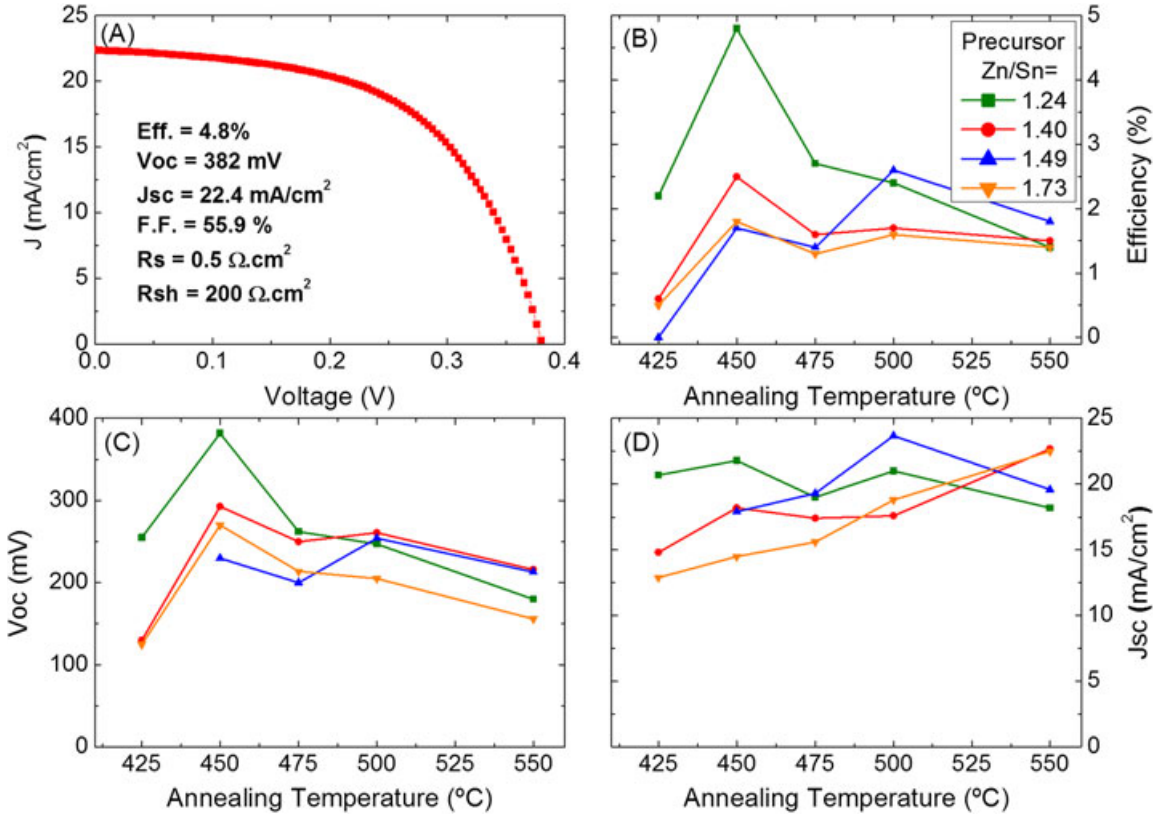

Figure 7. AM1.5 illuminated *J–V* curve of the best cell obtained in this work (A), and various cells properties as functions of precursor composition and annealing temperature: efficiency (B), V_{OC} (C), and J_{SC} (D).

low temperature annealing processes or other means of promoting accumulation of this phase on the surface rather than back of the absorber. Another potential explanation for the localized formation of ZnSe and SnSe in the back absorber region may be due to the decomposition of CZTSe to preferentially form $MoSe_2$ [14,23]. While Cu-Se phases are not detected, they may diffuse towards to surface region and react with the Se + Sn atmosphere and superficial ZnSe to form CZTSe, thus leading to a change from front absorber ZnSe accumulation in preference of back absorber region accumulation.

Finally, the AM1.5 illuminated *J–V* curve of the best cell and the evolution of device efficiency, V_{OC} and J_{SC} are shown as a function of precursor composition and annealing temperature in Figures 7. From Figure 7(B), it is clear that the highest efficiencies are typically obtained at 450°C regardless of the precursor composition for this low pressure thermal treatment (Eff. = 4.8%, V_{OC} = 0.382

V, $J_{SC} = 22.4\,mA/cm^2$, $FF = 55.9\%$). At higher and lower selenization temperatures, the efficiency tends to decrease. It is likely that selenization at 425°C does not allow sufficient crystallization of the films, while higher annealing temperatures lead to the deterioration of the back absorber region, as indicated by SEM and Raman scattering measurements. This means that working in such conditions, the optimum annealing temperature is remarkably lower than the optimum temperatures reported for processes at typically higher pressure, commonly equal to or higher than 500°C [4,5,13,14], that could be a clear advantage of the process presented here. Comparing Figure 7(B), (C), and (D), it is clear that the evolution of efficiency is mainly controlled by the V_{OC}, and not by J_{SC}. We propose that for higher Zn-excess and annealing temperatures the accumulation of ZnSe (n-type conductivity) and formation of voids at the back region of the absorber are the main mechanisms responsible for limiting the V_{OC}, as suggested by Raman scattering, SEM, and EDX measurements. Accumulation of ZnSe on the surface of the absorber does not appear to be as detrimental as formation of these voids. In contrast to V_{OC}, the average J_{SC} generally increases with temperature, but is not clearly influenced by the precursor composition. This suggests that the presence of ZnSe at the surface absorber region is detrimental for the short circuit current. This agrees with the behavior reported in [2,11,24,25] for the pure selenium and sulfide systems, where presence of superficial ZnS or ZnSe has been shown to have a direct impact on J_{SC}. On the other hand, the presence of SnSe in the back absorber region does not appear to be as detrimental to device properties as the presence of ZnSe and voids, because this phase is observed in samples with higher efficiencies.

4. CONCLUSIONS

CZTSe-based solar cells were prepared by a two-step process including a low pressure thermal treatment and the impact of the precursor composition, and annealing temperatures were studied. Both parameters have a significant effect on the V_{OC} of the devices, thus in turn on the power conversion efficiency. We have shown that ZnSe and SnSe are the main secondary phases in this system, and also how process parameters affect the accumulation of these phases. Increasing Zn-excess suppresses the formation of SnSe, but at the expense of increasing ZnSe formation especially at the back absorber region, concurrent with a reduction of the ZnSe concentration detected at the absorber surface region. Increasing annealing temperature leads to the formation of voids in the back absorber region due to the evaporation of SnSe formed from the poor uniformity of the Sn precursor layer or decomposition of CZTSe in contact with Mo, and promotes the diffusion of ZnSe to the back absorber region even more strongly than increased precursor Zn-excess. The best performing device had a power conversion efficiency of 4.8% and was fabricated from a precursor with compositional ratio of Zn/Sn = 1.24 and reactively annealed at the relatively low temperature of 450°C. We propose that the accumulation of ZnSe and formation of voids at the back absorber region mainly affects the V_{OC}, whereas accumulation on the surface appears to be detrimental for J_{SC}. Finally, low pressure and low temperature process parameters prevent the formation of a thick $MoSe_2$ interfacial layer at the absorber/Mo back contact interface, avoiding potential series resistance losses that can appear in devices with absorbers synthesized following a two-stage process.

ACKNOWLEDGEMENTS

The research leading to these results has received funding from the People Programme (Marie Curie Actions) of the European Union's Seventh Framework Programme FP7/2007–2013/ under REA grant agreement n°269167 (PVICOKEST). The research was also partially supported by MINECO, project KEST-PV (ref. ENE2010-121541-C03-01/02) and by European Regional Development Funds (ERDF, FEDER Programa Competitivitat de Catalunya 2007–2013). Authors from IREC and the University of Barcelona belong to the M-2E (Electronic Materials for Energy) Consolidated Research Group and the XaRMAE Network of Excellence on Materials for Energy of the "Generalitat de Catalunya". E. S. thanks the MINECO, Subprogram Ramón y Cajal (ref. RYC 2011-09212) and V. I Subprogram Juan de la Cierva (ref. JCI-2011-10782).

REFERENCES

1. Katagiri H, Jimbo K, Yamada S, Kamimura T, Maw WS, Fukano T, Ito T, Motohiro T. Enhanced conversion efficiencies of Cu_2ZnSnS_4-based thin film solar cells by using preferential etching technique. *Applied Physics Express* 2008; **1**: 041201. DOI: 10.1143/APEX.1.041201
2. Kato T, Hiroi H, Sakai N, Muraoka S, Sugimoto H. Characterization of front and back interfaces on Cu_2ZnSnS_4 thin-film solar cells. *27th European Photovoltaic Solar Energy Conference and Exhibition Proceedings* 2012; 2236–2239. DOI: 10.4229/27thEUPVSEC2012-3CO.4.2
3. Todorov TK, Reuter KB, Mitzi DB. High-efficiency solar cell with earth-abundant liquid-processed absorber. *Advanced Energy Materials* 2010; **22**: E159–159. DOI: 10.1002/adma.200904155
4. Repins I, Beall C, Vora N, DeHart C, Kuciauskas D, Dippo P, To B, Mann J, Hsu W-C, Goodrich A, Noufi R. Co-evaporated $Cu_2SnSnSe_4$ films and devices. *Solar Energy Materials and Solar Cells* 2012; **101**: 154–159. DOI: 10.1016/j.solmat.2012.01.008
5. Shin B, Zhu Y, Bojarczuk NA, Chey SJ, Guha S. Control of an interfacial $MoSe_2$ layer in $Cu_2ZnSnSe_4$ thin film solar cells: 8.9% power conversion efficiency with a TiN diffusion barrier. *Applied Physics Letters* 2012; **101**: 053903. DOI: 10.1063/1.4740276

6. Mitzi D, Gunawan O, Todorov TK, Wang K, Guha S. The path towards a high-performance solution-processed kesterite solar cell. *Solar Energy Materials and Solar Cells* 2011; **95**: 1421–1436. DOI: 10.1016/j.solmat.2010.11.028
7. Zuser A, Rechberger H. Consideration of resource availability in the technology development strategies: the case study of photovoltaics. *Resources, Conservation and Recycling* 2011; **56**: 56–65. DOI: 10.1016/j.resconrec.2011.09.004
8. Todorov TK, Tang J, Bag S, Gunawan O, Gokmen T, Zhu Y, Mitzi DB. Beyond 11% efficiency: characteristics of state-of-the-art $Cu_2ZnSn(S,Se)_4$ solar cells. *Advanced Energy Materials* 2012. DOI: 10.1002/aenm.201200348
9. Redinger A, Berg DM, Dale PJ, Siebentritt S. The consequences of kesterite equilibria for efficient solar cells. *Journal of the American Chemical Society* 2011; **133**: 3320–3323. DOI: 10.1021/ja111713g
10. Marcano G, Rincón C, López SA, Pérez GS, Herrera-Pérez JL, Mendoza-Alvarez JG, Rodríguez P. Raman spectrum of the monoclinic semiconductor Cu_2SnSe_3. et al. *Solid State Communications* 2011; **151**: 84–86. DOI: 10.1016/j.ssc.2010.10.015
11. Fairbrother A, García-Hemme E, Izquierdo-Roca V, Fontané X, Pulgarín-Agudelo FA, Vigil-Galán O, Pérez-Rodríguez A, Saucedo E. Development of a selective chemical etch to improve the conversion efficiency of Zn-rich Cu_2ZnSnS_4 solar cells. *Journal of the American Chemical Society* 2012; **134**: 8018–8021. DOI: 10.1021/ja301373e
12. Nesheva D, Scepanovic, MJ, Askrabic S, Levi Z, Bineva I, Popovic ZV. Raman scattering from ZnSe nanolayers. *Acta Physica Polonica A* 2009; **116**: 75–77.
13. Zoppi G, Forbes I, Miles RW, Dale PJ, Scragg JJ, Peter LM. $Cu_2ZnSnSe_4$ thin film solar cells produced by selenization of magnetron sputtered precursors. *Progress in Photovoltaics: Research and Applications* 2011; **19**: 315–319. DOI: 10.1002/pip.886.
14. López-Mariño S, Placidi M, Pérez-Tomás A, Llobet J, Izquierdo-Roca V, Fontané X, Fairbrother A, Espíndola-Rodríguez M, Sylla D, Pérez-Rodríguez A, Saucedo E. Inhibiting the absorber/Mo-back contact decomposition reaction in $Cu_2ZnSnSe_4$ solar cells: the role of a ZnO intermediate nanolayer. *Journal of Materials Chemistry A* 2013; **1**: 8338–8343. DOI: 10.1039/C3TA11419H
15. Redinger A, Hönes K, Fontané X, Izquierdo-Roca V, Saucedo E, Valle N, Pérez-Rodriguez A, Siebentritt S. Detection of a ZnSe secondary phase in coevaporated $Cu_2ZnSnSe_4$ thin films. *Applied Physics Letters* 2011; **98**: 101907. DOI: 10.1063/1.3558706
16. Araki H, Mikaduki A, Kubo Y, Sato T, Jimbo K, Maw WS, Katagiri H, Yamazaki M, Oishi K, Takeuchi A. Preparation of Cu_2ZnSnS_4 thin films by sulfurization of stacked metallic layers. *Thin Solid Films* 2008; **517**: 1457–1460. DOI: 10.1016/j.tsf.2008.09.058
17. Katagiri H. Cu2ZnSnS4 thin film solar cells. *Thin Solid Films* 2005; **480-481**: 426–432. DOI: 10.1016/j.tsf.2004.11.024
18. Babu GS, Kumar YBK, Bhaskar PU, Vanjari SR. Effect of Cu/(Zn + Sn) ratio on the properties of co-evaporated thin $Cu_2ZnSnSe_4$ films. *Solar Energy Materials and Solar Cells* 2010; **94**: 221–226. DOI: 10.1016/j.solmat.2009.09.005
19. Tanaka K, Fukui Y, Moritake N, Uchiki H. Chemical composition dependence of morphological and optical properties of Cu_2ZnSnS_4 thin films deposited by sol–gel sulfurization and Cu_2ZnSnS_4 thin film solar cell efficiency. *Solar Energy Materials and Solar Cells* 2011; **95**: 838–842. DOI: 10.1016/j.solmat.2010.10.031
20. Grossberg M, Krustok J, Raudoja J, Timmo K, Altosaar M, Raadik T. Photoluminescence and Raman study of $Cu_2ZnSn(Se_xS_{1-x})_4$ monograins for photovoltaic applications. *Thin Solid Films* 2011; **519**: 7403–7406. DOI: 10.1016/j.tsf.2010.12.099
21. Altosaar M, Raudoja J, Timmo K, Danilson M, Grossberg M, Krustok J, Mellikov E. $Cu_2Zn_{1-x}Cd_xSn(Se_{1-y}S_y)_4$ solid solution as absorber materials for solar cells. *Physica Status Solidi A* 2007; **205**: 167–170. DOI: 10.1002/pssa.200776839
22. Salomé PMP, Fernandes PA, da Cunha AF. Morphological and structural characterization of $Cu_2ZnSnSe_4$ thin films grown by selenization of elemental precursor layers. *Thin Solid Films* 2009; **517**; 2531–2534. DOI: 10.1016/j.tsf.2008.11.034
23. Scragg J, Wätjen JT, Edoff M, Ericson T, Kubart T, Plazter-Björkman C. A detrimental reaction at the molyenum back contact in $Cu_2ZnSn(S,Se)_4$ thin-film solar cells. *Journal of the American Chemical Society* 2012; **134**: 19330–19333. DOI: 10.1021/ja308862n
24. Hsu W-C, Repins I, Beall C, DeHart C, Teeter G, To B, Yang Y, Noufi R. The effect of Zn excess on kesterite solar cells. *Solar Energy Materials and Solar Cells* 2013; **113**: 160–164. DOI: 10.1016/j.solmat.2013.02.015
25. Wätjen JT, Engman J, Edoff M, Platzer-Björkman C. Direct evidence of current blocking by ZnSe in $Cu_2ZnSnSe_4$ solar cells. *Applied Physics Letters* 2012; **100**: 173510. DOI: 10.1063/1.4706256

ChemPubSoc Europe

DOI: 10.1002/cphc.201300157

Single-Step Sulfo-Selenization Method to Synthesize $Cu_2ZnSn(S_ySe_{1-y})_4$ Absorbers from Metallic Stack Precursors

Andrew Fairbrother,[a] Xavier Fontané,[a] Victor Izquierdo-Roca,[a] Moises Espindola-Rodriguez,[a] Simon López-Marino,[a] Marcel Placidi,[a] Juan López-García,[a] Alejandro Pérez-Rodríguez,[a, b] and Edgardo Saucedo*[a]

Pentenary $Cu_2ZnSn(S_ySe_{1-y})_4$ (kesterite) photovoltaic absorbers are synthesized by a one-step annealing process from copper-poor and zinc-rich precursor metallic stacks prepared by direct-current magnetron sputtering deposition. Depending on the chalcogen source—mixtures of sulfur and selenium powders, or selenium disulfide—as well as the annealing temperature and pressure, this simple methodology permits the tuning of the absorber composition from sulfur-rich to selenium-rich in one single annealing process. The impact of the thermal treatment variables on chalcogenide incorporation is investigated. The effect of the S/(S+Se) compositional ratio on the structural and morphological properties of the as-grown films, and the optoelectronic parameters of solar cells fabricated using these absorber films is studied. Using this single-step sulfo-selenization method, pentenary kesterite-based devices with conversion efficiencies up to 4.4% are obtained.

1. Introduction

The future mass deployment of thin-film photovoltaic technologies calls for the development of cost-effective processes based on earth-abundant, low-cost, and low-toxicity materials without significant reduction of the solar-cell efficiency. Of the three main thin film technologies at industrial levels of production, those based on $Cu(In,Ga)Se_2$ (CIGS) absorbers have the highest cell (>20%)[1] and module efficiency. However, the scarcity of indium constitutes a potential limitation for future mass deployment, and consequently, its replacement has led to the investigation of materials with similar properties. Among these materials, kesterite [$Cu_2ZnSn(S,Se)_4$, abbreviated CZTSSe] is attracting strong interest because it is composed of more earth-abundant elements, and has the potential to fulfill the requirements of a thin-film absorber layer.[2–4] The similarities between CZTSSe and CIGS indicate the potential of this new material to become a reliable alternative in the near future. Although very promising, the maximum conversion efficiencies reported for devices based on these materials are still far from those achieved with more mature CIGS technologies. Further improvement of these efficiencies strongly depends on a deeper understanding of the key parameters that limit the efficiency of the devices in the whole range of S/(S+Se) compositional ratios, as well as the development of customized synthesis routes adapted to the peculiarities of CZTSSe.

Currently, the highest efficiencies for kesterite-based devices that have been reported consist of the mixed sulfur-selenide compound with selenium-rich S/(S+Se) ratios, as illustrated in Figure 1, where the relevant references are listed. To date, several methods have been employed for the preparation of CZTSSe pentenary films and devices, for example, co-evaporation,[5] pulsed-laser deposition,[6] monograin molten-salt synthesis,[7] nanocrystal coatings,[8] hybrid solution-particle coatings,[2,9] and so forth. In nearly all cases, a precursor containing sulfur or selenium is submitted to a reactive annealing step under an atmosphere containing the alternate chalcogenide element to form the desired pentenary compound. However, little is reported on how to precisely tune the chalcogen composition, and therefore affect the bandgap of kesterite and other sulfur-selenium multinary compounds, except in the synthesis of bulk and powder compounds.[7,10,11] Deeper understanding of the influence of the different process parameters on the incorporation of sulfur and selenium into the precursor films is critical for the development of simple and reliable processes allowing for precise control of the composition and bandgap of the pentenary absorbers.

In this context, and in contrast to the typical method for fabrication of CZTSSe films, this work reports the preparation of CZTSSe pentenary films from chalcogenide-free (metallic) precursors using a one-step sulfo-selenization process. This process is of interest for a variety of metallic-film deposition meth-

[a] A. Fairbrother, X. Fontané, Dr. V. Izquierdo-Roca, M. Espindola-Rodriguez, S. López-Marino, Dr. M. Placidi, Dr. J. López-García, Prof. A. Pérez-Rodríguez, Dr. E. Saucedo
Advanced Materials for Energy
Catalonia Institute for Energy Research
Jardins de les Dones de Negre 1
2pl, 08930 Sant Adrià del Besòs, Barcelona (Spain)
E-mail: esaucedo@irec.cat

[b] Prof. A. Pérez-Rodríguez
IN²UB, Departament d'Electrònica
Universitat de Barcelona
Martí i Franquès, 1-11
08028 Barcelona (Spain)

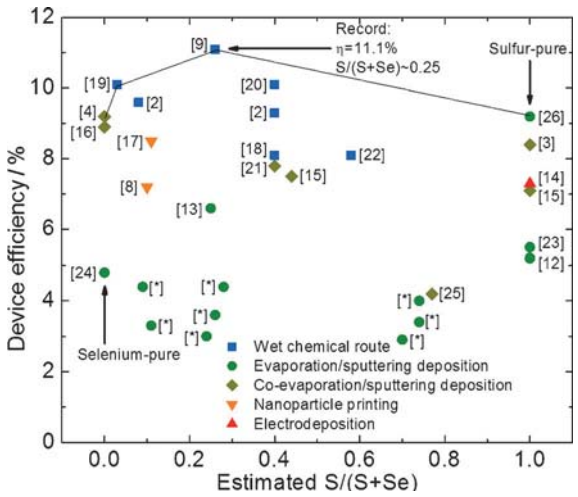

Figure 1. Efficiency versus estimated S/(S+Se) ratio from various devices reported in the literature. [*] refers to devices presented in this work. For references in which this value is not reported, S/(S+Se) content ratio was estimated from reported bandgaps,[10] assuming the commonly reported bandgap values of 1.0 eV for CZTSe and 1.5 eV for CZTS.

ods, many of them already used to prepare CZTS or CZTSe, including DC (direct current)-magnetron sputtering deposition,[12,13] thermal and electron-beam evaporation,[27] electroless and electrochemical deposition,[14,28] printing or coating of metal-based slurries or particulates, and so forth. The method proposed herein, even though applied to the particular case of the formation of $Cu_2ZnSn(S_{1-y}Se_y)_4$ pentenary films from metallic precursors, can also be applied to other important photovoltaic semiconductor materials, such as $CuIn(S_{1-y}Se_y)_2$, $CuIn_{1-x}Ga_x(Se_{1-y}S_y)_2$, $ZnS_{1-y}Se_y$, among others.

One potential method to prepare the pentenary compound from metallic precursors is to submit the precursors to a two-step thermal annealing, starting with a sulfurization step followed by a selenization step, or vice versa. Although viable, this approach complicates technology implementation due to the necessity of two different thermal processes with different characteristics, which would require different furnace setups. This would consume a considerable amount of time and energy by effectively doubling the total thermal processing time. Thus, a single-step thermal treatment capable of introducing both sulfur and selenium is of interest. There are some reports on single-step sulfo-selenization processes for Cu-In,[29,30] and even for Cu-Zn-Sn precursors,[13,25] but little is known on the effect of process parameters on chalcogen incorporation. Lechner et al.,[13] for example, used a fixed thermal treatment process giving a compositional ratio of S/(S+Se) of ~0.25, and focused their study on precursor composition variations. Momose et al.[25] demonstrated the ability of tuning the S/(S+Se) ratio by varying the amount of each chalcogen placed in vacuum-sealed ampoules. Under similar thermal processing conditions, the devices produced varied broadly in efficiency, indicating the need for different thermal processes (temperature, pressure, and so forth) to form high-quality absorber materials of a given composition.

To better understand the sulfo-selenization process it is useful to study sulfur and selenium in the vapor phase. Pure and mixed sulfur and selenium have been studied extensively. They have a complex structure involving numerous stable ring configurations, most commonly based on eight-atom rings (i.e. $S_{8-y}Se_y$).[31–36] Vapors of these chalcogens are mostly derived from such eight-atom-based clusters in a complementary manner (i.e. pairs of $S_y^+ + S^-_{8-y}$),[33] with smaller clusters forming at higher temperatures, and up to monatomic sulfur above 2200 °C.[32] Cluster formation varies significantly for sulfur-selenium mixtures when compared to pure sulfur or selenium vapors.[33–36] Vapors of sulfur-selenium mixtures have a tendency to form smaller clusters at higher temperatures, with sulfur-rich clusters inclined to form negatively charged ionic species, whereas selenium-rich clusters are positively charged.[33] Also, the vapor pressure of selenium is higher when mixed with sulfur, even when compared to pure selenium vapors under similar conditions.[35] The relation between various volatile species will affect CZTSSe formation during annealing, as positively charged chalcogenide clusters can be expected to be more reactive toward the metallic precursor. Additionally, the formation and stability of various compounds in the Cu-Zn-Sn-S-Se material system have been calculated.[37] Under equilibrium conditions sulfur binaries tend to have lower Gibbs free energies of formation. All these features confirm the complexity of the processes involved in annealing in a sulfur- and selenium-containing atmosphere to induce the formation of a sulfo-selenized compound. In the first case, the formation of selenium-rich Cu-Zn-Sn-S-Se compounds can be expected to be kinetically favored due to the positively charged selenium-rich clusters, which are more reactive. On the other hand, thermodynamic equilibrium conditions would favor the formation of sulfur-rich Cu-Zn-Sn-S-Se compounds due to a lower Gibbs free energy of formation for pure sulfur phases. An additional complication arises from the decomposition of CZTSSe,[37,38] as SnS is more volatile than its selenium analogue, SnSe.

In this work, pentenary CZTSSe thin films are synthesized by a one-step sulfo-selenization process, using Sn/Cu/Zn metallic precursor stacks deposited by DC-magnetron sputtering. We show the possibility of tuning the S/(S+Se) ratio to form sulfur-rich CZTSSe films, down through a range of selenium-rich films. Structural analysis by Raman scattering spectroscopy, morphological analysis by scanning electron microscopy (SEM), and photoluminescence measurements (PL) of the films are presented. The influence of annealing variables (chalcogenide source, total system pressure, and temperature) on sulfur and selenium incorporation in the films is studied. Solar-cell devices are prepared and characterized with the different absorbers, from which moderate efficiencies in the whole S/(S+Se) ratio range are obtained, including a maximum efficiency of 4.4%. The results obtained corroborate the potential of the proposed methodology for the development of a simple and reliable thermal process enabling deposition technologies based on metallic precursors to form pentenary CZTSSe-based solar cells of superior efficiency, which to date has been mostly limited to chalcogen-containing precursors.

2. Results and Discussion

$Cu_2ZnSn(S_ySe_{1-y})_4$ films were formed by a single-step sulfo-selenization process in a wide range of compositions, as shown in the schematic representation of the Raman spectra for ten different samples as a function of the S/(S+Se) ratio (Figure 2A), which includes nearly selenium-pure to nearly sulfur-pure films. Figure 2B shows the Raman spectra from selected samples, including both pure selenide and pure sulfide compounds (bottom and top spectra, respectively). The Raman spectrum from a pure sulfide CZTS film presents a dominant peak at ~337 cm^{-1}, whereas that from a pure selenide CZTSe film is found at ~194 cm^{-1}, both peaks corresponding to the main A-symmetry vibrational mode of the kesterite structure.[39,40] The Raman spectrum of the pentenary compound is characterized by the presence of a CZTS- and CZTSe-like peaks.[7] The changing composition of the films is reflected in the variation of the frequency of the CZTSe-like peak, which increases significantly with the S/(S+Se) relative content, whereas the relative peak intensity decreases. In contrast, the frequency of the CZTS-like peak shows a much smaller dependence on the S/(S+Se) content ratio. This peak is shifted only slightly in the spectral region from 337–331 cm^{-1}, even for selenium-rich films. On the other hand, the full width at half maximum (FWHM) increases significantly, from 6.6 to 17.2 cm^{-1} across the same range of sample compositions. This agrees with the behavior previously reported by Grossberg et al.,[7] and is similar to the evolution of Se–Se- and S–S-like vibrational modes from the structurally similar chalcopyrite $CuIn(S,Se)_2$ quaternary system.[41] Raman scattering is a superficial measurement (less than 100 nm penetration depth in CZTS for a 514 nm excitation), therefore, it is important to note that there is no evidence of grading in the S/(S+Se) ratio throughout the film thickness, as confirmed by secondary-ion mass spectroscopy measurements (not shown). The estimated compositions shown in Figure 2 were derived from external quantum efficiency (EQE) measurements presented in Figure 3A.

Incorporation of selenium and sulfur is affected in various orders of significance by each of the three process parameters: 1) chalcogen source, 2) total system pressure, and 3) annealing temperature. The most significant factor is the chalcogen source (1). Sulfur-rich S+Se mixtures and SeS_2 sources favor the formation of sulfur-rich films. This might be expected,[25] however, the amount of sulfur or selenium incorporated into the films may not readily be determined by the chalcogen source, as the vapor-phase behavior of S+Se mixtures varies from that of pure sulfur or selenium.[33–36] The second thermal treatment factor, apparently of lesser significance, is the total system pressure (2), in which higher pressures give rise to films richer in sulfur. Sulfur in the vapor phase is more likely to associate in small clusters,[33,34] which have higher vapor pressures than selenium and selenium-rich clusters. This means that more sulfur is lost than selenium in the low-pressure thermal processes. In fact, low-pressure thermal treatments with sulfur-rich chalcogen sources produce films that are still partially metallic, another indication of the higher volatility of sulfur-rich clusters. The least significant factor studied is the annealing temperature (3). Higher temperatures incorporate preferentially selenium into the films. This can be related to the increased volatility of selenium-rich clusters at higher temperatures, as well as the formation of smaller positively charged selenium-rich clusters, which may be more reactive. In summary, we can conclude that a selenium-rich chalcogen source, lower system pressure, and higher annealing temperatures favor the formation of more selenium-rich CZTSSe films, whereas sulfur-rich chalcogen sources, higher system pressure, and lower annealing temperatures favor the formation of more sulfur-rich films.

Photoluminescence and spectral response (EQE) measurements of some of the prepared films are shown in Figure 3, spanning the range of compositions shown in Figure 2. Regardless of the precursor composition and multiple process runs, each specific process resulted in films of a particular bandgap (±20 meV), indicating the reproducibility of achiev-

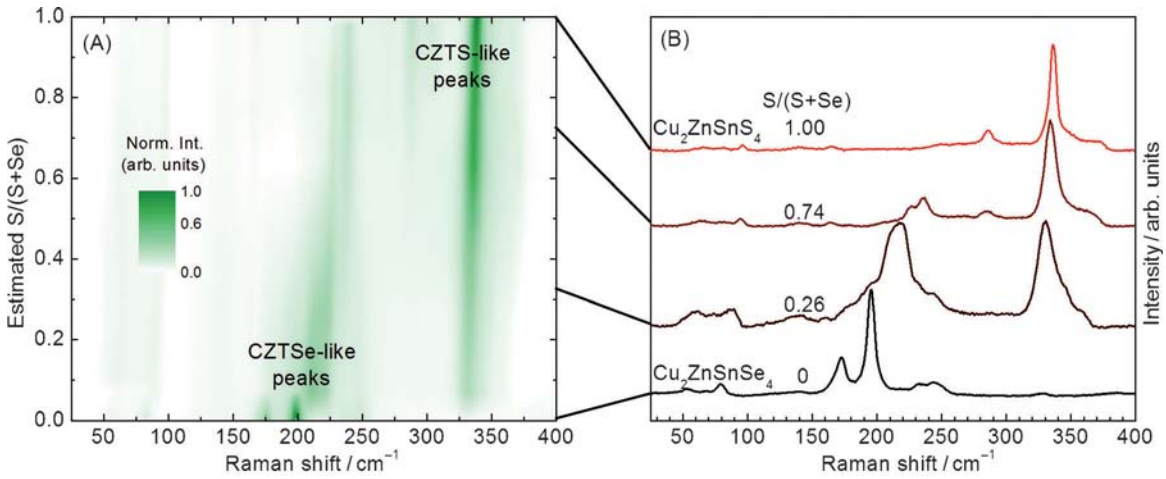

Figure 2. Multi-sample schematic color-code representation of the Raman spectra of ten different samples showing the whole range composition from sulfur-pure to selenium-pure compounds (A), and selected spectra of four samples (B). The sulfur content was estimated using the bandgaps estimated in Figure 3A from external quantum efficiency measurements.

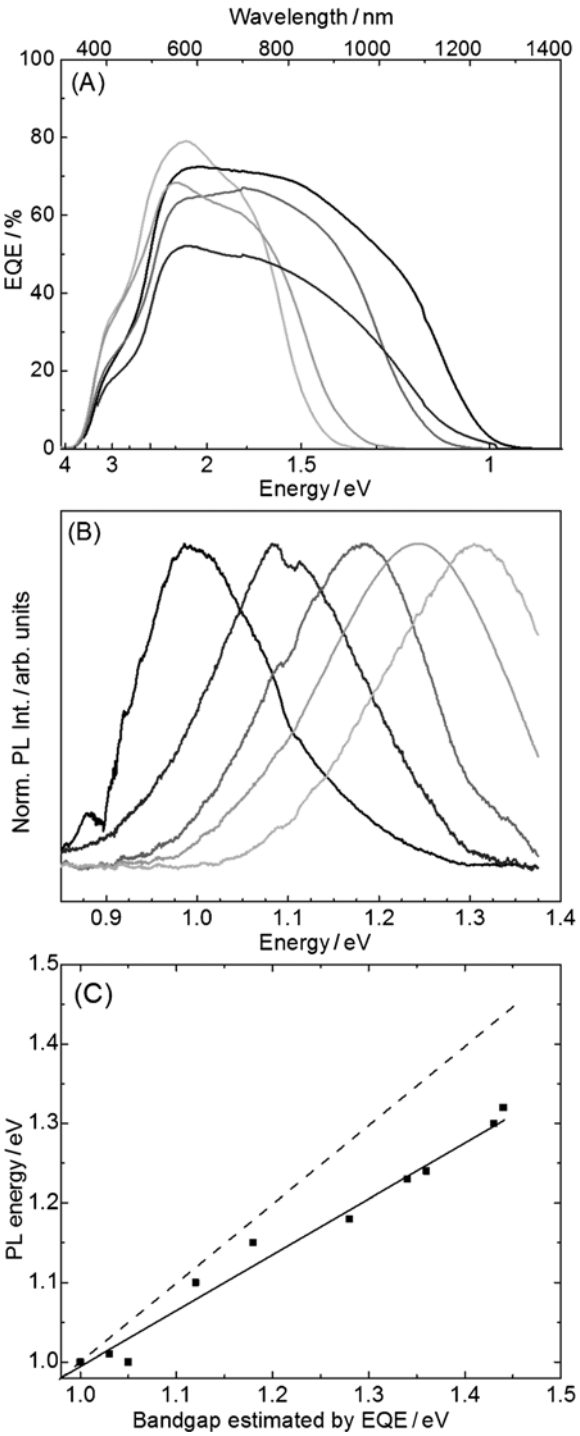

Figure 3. External quantum efficiency of CZTSSe-based devices and corresponding estimated bandgaps (A), room temperature photoluminescence spectra of films with varying S/(S+Se) content (B), and correlation between peak PL energy and bandgap (C). The dashed line shows the 1:1 correlation. Discontinuities (i.e. 0.9 and 1.1 eV) in the PL spectra are due to water absorption from the air.

ing a particular S/(S+Se) composition using this method. The EQE measurements (Figure 3A) can be used to perform a rough estimation of the absorber bandgap and thus determine the S/(S+Se) ratio.[10] These measurements corroborate the possibility of wide-range tuning of the CZTSSe-film bandgap, from 1.00 eV (CZTSe) to 1.46 eV (CZTS), obtaining peak EQE values for most samples between 50–80% in the 600–800 nm wavelength region. Room temperature PL measurements (Figure 3B) show a broad luminescence band that shifts toward higher energies as the S/(S+Se) relative content increases. As shown in Figure 3C, the energy of the maximum PL signal correlates linearly with the bandgap estimated from EQE measurements. However, this plot shows a slope lower than one. For selenium-rich films, the energy of the PL peak is close to the bandgap of the absorber, whereas increasing the S/(S+Se) relative content leads to a decrease of the energy of the PL peak in relation to that of the bandgap. Although the origin of the peaks observed in the PL measurements is not elucidated in this study, we suggest that the PL band from sulfur-rich films is related to donor–acceptor pair transitions from defects rather than band-to-band or band-to-defect radiative recombinations. The fact that the EQE bandgap estimation and PL energy are closely matched for CZTSe and selenium-rich CZTSSe suggests that the shallow defect levels are much closer to the valence and conduction bands for these films. This could be a confirmation of the noticeable differences between the band structure of selenium-rich and sulfur-rich absorbers.[7] This effect is also noticed in the EQE measurements, because the peak-charge collection region is much flatter for CZTSe compared to CZTS. This may explain why the open-circuit voltage (V_{OC}) of sulfur-rich CZTSSe-based devices is much lower than the expected value from the bandgap of the films (the so-called V_{OC} deficit), especially when compared with selenium-rich CZTSSe-based devices, as explained in more detail in the discussion of the device properties.

The morphology of the devices fabricated from the CZTSSe films is shown in the cross-sectional SEM micrographs in Figure 4. All films are approximately 2.5 μm thick, and a thin layer of $Mo(S,Se)_2$ forms at the Mo back contact, barely discernible from the SEM micrographs. These images show that the grain size of the pure selenide compound (Figure 4A) is typically smaller than that of the pure sulfide one (Figure 4F), whereas the pentenary compounds exhibit even larger grain sizes, up to 2 μm (Figure 4B–E, in order of increasing sulfur content). Note that annealing pressure and temperature for the pure-sulfide and pure-selenide films are different, 550 °C and 450 °C, respectively, which may be responsible for the larger grain size in pure sulfide films. Interestingly, when compared with the quaternary films, the sulfo-selenide films have larger grain sizes, even for similar annealing temperatures and pressures. According to these results, annealing atmospheres with mixed-chalcogen sources (S + Se or SeS_2) enhance grain growth when compared to pure sulfur or selenium atmospheres under the same conditions used herein. This could be related to the higher reactivity of S + Se vapor mixtures compared to the pure vapors. In addition, annealing temperature and pressure also affect the grain size. Figure 4B, C shows films annealed with 40 mg Se + 10 mg S, at 550 °C, 1 bar Ar, and 450 °C and 1 mbar Ar flow, respectively. In this case, the grain size is larger at lower temperature and annealing pressure, an unexpected result. This feature is potentially related to the increased volatility of the S + Se mixture at higher temper-

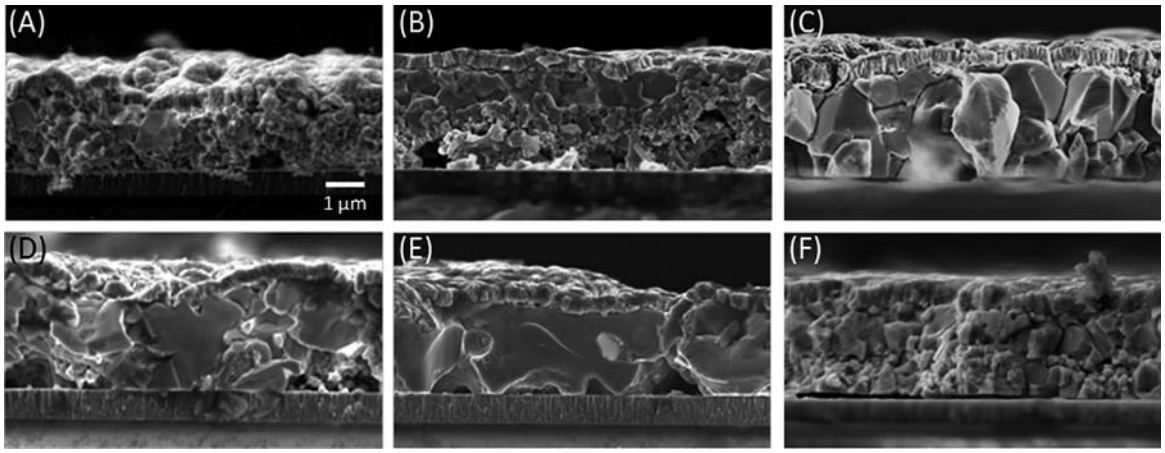

Figure 4. Cross sectional SEM images of kesterite films: pure selenide compound (A), sulfo-selenides with increasing S/(S+Se) ratios: 0.26 (B), 0.39 (C), 0.63 (D), and 0.74 (E), and pure sulfur compound (F). These samples were prepared from the same precursors with a composition of Zn/Sn = 1.24.

atures, which is not compensated by the total pressure of the system. It may also be related to the decomposition of the CZTSSe phase at these temperatures, which is due to tin loss at the surface of the films and reaction with the molybdenum back-contact, as observed in pure CZTS films,[37,38] which may inhibit grain growth. Figure 4D, E shows films annealed with 10 mg SeS_2 at 550 °C, at 1 mbar and 1 bar Ar pressure, respectively. In this case—a more sulfur-rich chalcogen source than the previous example—it appears that higher system pressure enhances grain growth for these films.

The maximum conversion efficiency as a function of the estimated bandgap and composition of the absorbers is listed in Table 1, with best-performing pentenary-device efficiencies of 4.4, 4.4, and 4.0%, obtained for S/(S+Se) ratios of 0.09, 0.28, and 0.74, respectively. Also listed are the annealing conditions used for each composition. The highest efficiencies were obtained for the pure sulfide and selenide compounds, in contrast to chemical-based routes reporting higher efficiencies for pentenary compounds.[2,9] This implies that further improvement on the sulfo-selenization process may increase device efficiency considerably. Various devices above 3% efficiency were produced, both with sulfur- and selenium-rich compositions. Samples prepared from precursors with the lowest Zn-excess (Zn/Sn = 1.24), exhibited higher device performance than those with higher precursor Zn-excess. There is a notable drop in device efficiency for films with bandgaps of ~1.2–1.3 eV, which does not necessarily indicate an intrinsic deficiency of middle-bandgap CZTSSe films (see for example the numerous higher efficiency devices in this range in Figure 1), but rather a need to optimize the thermal treatment parameters for this range of film compositions. When comparing grain sizes in the SEM micrographs, some films with smaller grains show higher efficiency than large-grain films. While one might expect higher efficiency for films with larger grains, there are additional factors affecting it, including passivation at the grain boundaries, interfaces with back and front contacts, and so forth. Thus, a direct correlation between grain size and efficiency may not be appropriate. It is interesting to note that sulfur-rich films (40 mg S + 10 mg Se, 550 °C, 1 bar Ar) show a notably lower efficiency compared to the pure sulfide compounds prepared under similar conditions (50 mg S, 550 °C, 1 bar Ar). This may be due to the addition of a small amount of selenium, which decreases significantly the abundance of positively charged sulfur-rich clusters in the annealing atmosphere; this could slow down the formation reaction and lead to worsened film properties.

Table 1. Best cell efficiencies listed by chalcogen source.

Chalcogen source[a]	Bandgap [eV]	S/(S+Se)	Best cell efficiency [%]	Annealing temp. [°C]	System pressure [bar]
50 mg Se					
	1.00	0.00	4.8[24]	450	0.001
40 mg Se + 10 mg S					
	1.04	0.09	4.4	550	0.001
	1.05	0.11	3.3	550	0.001
	1.11	0.24	3.0	550	1
	1.12	0.26	3.6	550	1
	1.13	0.28	4.4	550	1
	1.18	0.39	0.1	450	0.001
10 mg SeS_2					
	1.28	0.61	0.2	450	0.001
	1.29	0.63	0.7	550	0.001
	1.32	0.70	2.9	550	0.001
	1.33	0.72	1.6	550	1
	1.34	0.74	4.0	550	1
	1.34	0.74	3.4	550	1
	1.37	0.80	2.0	500	1
10 mg Se + 40 mg S					
	1.43	0.93	0.9	550	1
50 mg S					
	1.46	1.00	5.5[23]	550	1
	1.46	1.00	5.2[12]	550	1

[a] Repeated thermal treatments were done with different precursor films of varying composition in order to test the reproducibility of each process.

Additionally, low-pressure processes, with the exception of those for devices made from pure and selenium-rich films, produced shunted (i.e. still partially metallic films) or low-efficiency devices (<1%). These results indicate a need for optimization of the sulfo-selenization process to improve device performance for a desired S/(S+Se) composition.

While device efficiency did not show any apparent dependence on composition, other optoelectronic properties did (Figure 5). As expected, the values for V_{OC} show a positive linear dependence (Figure 5A) on the absorber bandgap, and

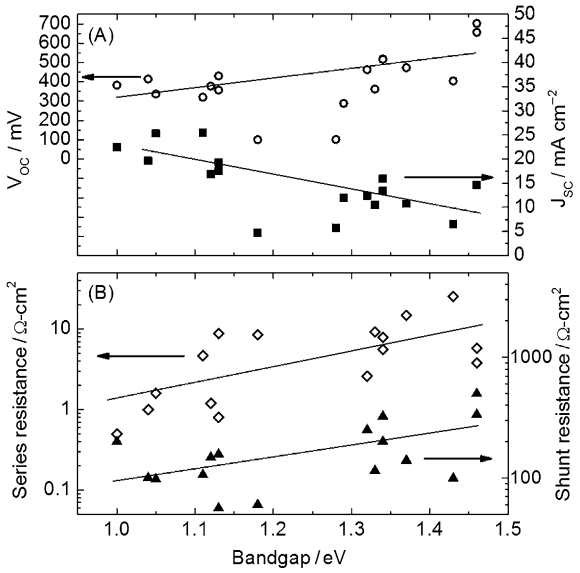

Figure 5. Device properties versus estimated absorber bandgap: A) open circuit voltage (V_{OC}, ○) and short-circuit current density (J_{SC}, ■) and B) series resistance (◇) and shunt resistance (▲).

are comparable to some of the best results reported so far in the literature.[2–4] On the other hand, short-circuit current density (J_{SC}) shows a negative linear dependence on the bandgap (Figure 5A).

When comparing relative changes for V_{OC} and J_{SC} [$\Delta V_{OC}/V_{OC(max)}$ and $\Delta J_{SC}/J_{SC(max)}$], the change for V_{OC} (~0.35) is smaller than for J_{SC} (~0.58). This could be related to the observed discrepancy of the estimated bandgap by EQE and PL, as shown in Figure 3C. For the sulfur-rich absorbers, V_{OC} is much lower than expected, suggesting that for these materials recombination at the bulk phase plays a more important role in the limitation of the devices efficiency than in selenium-rich devices. The series and shunt resistances are shown in Figure 5B; while these trends are less evident for V_{OC} and J_{SC}, both values increase with increasing bandgap. In summary, all of these results corroborate the possibility to tune the S/(S+Se) ratio and in consequence the bandgap of CZTSSe absorber-films with this simple sulfo-selenization approach. This opens the possibility to have a simpler route to synthesize pentenary films with a desired composition, starting from metallic precursors.

3. Conclusions

This work demonstrates the possibility of obtaining device-grade CZTSSe films of a wide range of S/(S+Se) compositions using a single-step sulfo-selenization annealing process of sputter-deposited metallic precursors. Such a single-step procedure does not necessitate incorporation of sulfur or selenium into the precursor prior to annealing, as usually done to obtain pentenary films, and as such is aptly suited for a wider variety of techniques used to prepare metallic thin films. Chalcogen source, pressure, and annealing temperature affect the incorporation of sulfur and selenium in order of decreasing effectiveness. Sources richer in one chalcogen favor its incorporation into the final film, whereas lower system pressures and higher annealing temperatures lead to preferential incorporation of selenium. Structural and morphological characterization of the films confirm the high-crystalline quality of the films, and suggest that further progress in the conversion efficiency (4.4%) depends on the improvement of the annealing process, which varies depending on the desired composition.

Experimental Section

Sn/Cu/Zn metallic-stack precursors were deposited by DC-magnetron sputtering (Ac450 Alliance Concepts) using four-inch diameter, 99.99% purity targets, onto 10×10 cm^2 Molybdenum-coated soda-lime glass (800 nm thickness, $R_{□}$=0.18 Ω/□). The conditions for the deposition of each metal were: tin (power density: 0.64 W cm^{-2}, argon gas pressure: 0.001 mbar), copper (1.27 W cm^{-2}, 0.001 mbar), and zinc (1.27 W cm^{-2}, 0.001 mbar). In all cases the substrate was rotated at 10 rpm unheated, though some heating may occur as a result of the deposition process. Thickness and composition of the stacks was determined by X-ray fluorescence spectroscopy (XRF, Fisherscope XVD), which was previously calibrated with measurements by inductively-coupled plasma-optical emission spectroscopy (ICP-OES). Precursor films were approximately 800–840 nm thick, with composition ratios of Cu/(Zn+Sn)=0.77–0.87 and Zn/Sn=1.24–1.49.

For pure sulfide and selenide samples, metallic precursors (2×2 cm^2 in area) were annealed reactively in a tubular furnace with the capability of functioning under vacuum (10^{-4} mbar) or an inert gas atmosphere (Ar). In this step the samples and chalcogen source were placed directly next to each other in a graphite box with an interior volume of 23.5 cm^3. The box serves as a semi-closed system to partially protect and maintain the chalcogen-containing atmosphere during annealing, though overpressure eventually equilibrates with the atmosphere of the tube outside of the box. Standard quaternary CZTS absorbers were produced by reactive annealing under a sulfur atmosphere at 550 °C during 30 min in a 1 bar argon atmosphere, using two crucibles, one with 50 mg of sulfur powder (Alfa Aesar, 99.995%) and the other with 5 mg of tin powder (Alfa-Aesar, 99.999%). Addition of elemental tin in the annealing process has been shown to suppress its loss from the films during annealing, and significantly improved device properties.[38] The standard CZTSe absorbers were produced by reactive annealing under a selenium atmosphere at 450 °C during 45 min, under a flow of argon to maintain a pressure of 1 mbar, and also with two crucibles, one containing 50 mg of selenium powder (Alfa Aesar, 99.999%) and the other with 5 mg of tin powder. The heating ramp for all thermal treatments was 20 °C min^{-1}, and the

cooling was allowed to proceed naturally, requiring approximately 2–3 h.

To form pentenary CZTSSe films a single-step sulfo-selenization annealing was used. The process is similar to that used for pure CZTS or CZTSe films, varying the reactive annealing element with powders of either a mixture of sulfur and selenium (S + Se), or selenium disulfide (SeS_2). For S + Se powder mixtures two compositions were used: sulfur-rich (10 mg Se powder + 40 mg S powder), and selenium-rich (40 mg Se powder + 10 mg S powder). SeS_2 (Alfa Aesar, 97%) was also investigated as a chalcogen source for reactive annealing, with 10 mg of powder used. In all cases 5 mg of tin powder were placed in a second crucible in the graphite box. Annealing temperature and pressure were varied within the range used for standard CZTS and CZTSe films, from 450 °C to 550 °C, and at a pressure from 1 mbar to 1 bar of argon, with an annealing time of 30 min.

Samples were characterized for structural (Raman, 514 nm excitation, T64000 Horiba-Jobin Yvon, 100 μm spot diameter), cross-section morphological (SEM, Zeiss Series Auriga field emission scanning electron microscope), and photoluminescent (PL) properties (785 nm excitation, Horiba-Jobin Yvon iHR310 spectrometer, 100 μm spot diameter). Solar-cell devices were fabricated first by etching each film in a solution of HCl 5% v/v at 75 °C for 300 s (motivation and details of this etching process can be found in ref. [12]), then by depositing CdS (60 nm) by chemical bath deposition, followed by pulsed DC-magnetron sputtering deposition of i-ZnO (50 nm) and ZnO:Al (450 nm, $R_{\square} = 19.0\ \Omega/\square$). For the optoelectronic characterization, $3 \times 3\ mm^2$ cells were scribed, and the illuminated *J–V* curves were obtained using an ABET Technologies Sun 3000 Class AAA solar simulator. The external quantum efficiency (EQE) of the devices was also measured and compared with the absorber composition and the device optoelectronic properties (Bentham PVE300).

Acknowledgements

This research was partially supported by the Ministerio de Economía y Competitividad, project KEST-PV (ref. ENE2010-121541-C03-1), the Framework 7 Program under the projects PVICOKEST (PIRSES-GA-2009-269167) and KESTCELLS (FP7-PEOPLE-2012-ITN-316488), and by theEuropean Regional Development Funds (ERDF, FEDER Programa Competitivitat de Catalunya 2007–2013). Authors from IREC and the University of Barcelona belong to the M-2E (Electronic Materials for Energy) Consolidated Research Group and the XaRMAE Network of Excellence on Materials for Energy of the "Generalitat de Catalunya". E.S. thanks the Government of Spain for the "Ramon y Cajal" fellowship (RYC-2011-09212), V.I. for the "Juan de la Cierva" fellowship (JCI-2011-10782).

Keywords: annealing · metallic precursors · pentenary mixtures · solar cells · chalcogenides

[1] P. Jackson, D. Hariskos, E. Lotter, S. Paetel, R. Wuerz, R. Menner, W. Wischmann, M. Powalla, *Prog. Photovolt. Res. Appl.* **2011**, *19*, 894–897.
[2] T. K. Todorov, K. B. Reuter, D. B. Mitzi, *Adv. Mater.* **2010**, *22*, 1–4.
[3] B. Shin, O. Gunawan, Y. Zhu, N. A. Bojarczuk, S. J. Chey, S. Guha, *Prog. Photovolt. Res. Appl.* **2013**, *21*, 72–76.
[4] I. Repins, C. Beall, N. Vora, C. DeHart, D. Kuciauskas, P. Dippo, B. To, J. Mann, W.-C. Hsu, A. Goodrich, R. Noufi, *Sol. Energy Mater. Sol. Cells* **2012**, *101*, 154–159.
[5] L. Grenet, S. Bernardi, D. Kohen, C. Lepoittevin, S. Noël, N. Karst, A. Brioude, S. Perraud, H. Mariette, *Sol. Energy Mater. Sol. Cells* **2012**, *101*, 11–14.
[6] J. He, L. Sun, N. Ding, H. Kong, S. Zuo, S. Chen, Y. Chen, P. Yang, J. Chu, *J. Alloys Compd.* **2012**, *529*, 34–37.
[7] M. Grossberg, J. Krustok, J. Raudoja, L. Timmo, M. Altosaar, T. Raadik, *Thin Solid Films* **2011**, *519*, 7403–7406.
[8] Q. Guo, G. M. Ford, W.-C. Yang, B. C. Walker, E. A. Stach, H. W. Hillhouse, R. Agrawal, *J. Am. Chem. Soc.* **2010**, *132*, 17384–17386.
[9] T. K. Todorov, J. Tang, S. Bag, O. Gunawan, T. Gokmen, Y. Zhu, D. B. Mitzi, *Adv. Energy Mater.* **2013**, *3*, 34–38.
[10] J. He, L. Sun, S. Chen, Y. Chen, P. Yang, J. Chu, *J. Alloys Compd.* **2012**, *511*, 129–132.
[11] M.-Y. Chiang, S.-H. Chang, C.-Y. Chen, F.-W. Yuan, H.-Y. Tuan, *J. Phys. Chem. C* **2011**, *115*, 1592–1599.
[12] A. Fairbrother, E. García-Hemme, V. Izquierdo-Roca, X. Fontané, F. A. Pulgarín-Agudelo, O. Vigil-Galán, A. Pérez-Rodríguez, E. Saucedo, *J. Am. Chem. Soc.* **2012**, *134*, 8018–8021.
[13] R. Lechner, S. Jost, J, Palm, M. Gowtham, F. Sorin, B. Louis, H. Yoo, R. A. Wibowo, R. Hock, *Thin Solid Films* **2012**, DOI: 10.1016/j.tsf.2012.10.042.
[14] S. Ahmed, K. Reuter, O. Gunawan, L. Guo, L. Romankiw, H. Deligianni, *Adv. Energy Mater.* **2012**, *2*, 253–259.
[15] B. Shin, K. Wang, O. Gunawan, K. B. Reuter, S. J. Chey, N. A. Bojarczuk, T. Todorov, D. B. Mitzi, S. Guha, *Proc. 37th IEEE PVSC Conf.* (Seattle, WA, USA) **2011**, p. 002510.
[16] B. Shin, Y. Zhu, N. A. Bojarczuk, S. J. Chey, S. Guha, *Appl. Phys. Lett.* **2012**, *101*, 053903.
[17] Y. Cao, M. S. Denny, Jr., J. V. Caspar, W. E. Farneth, Q. Guo, A. S. Ionkin, L. K. Johnson, M. Lu, I. Malajovich, D. Radu, H. D. Rosenfeld, K. R. Choudhury, W. Wu, *J. Am. Chem. Soc.* **2012**, *134*, 15644–15647.
[18] W. Yang, H.-S. Duan, B. Bob, H. Zhou, B. Lei, C.-H. Chung, S.-H. Li, W. W. Hou, Y. Yang, *Adv. Mater.* **2012**, *24*, 6323–6329.
[19] S. Bag, O. Gunawan, T. Gokmen, Y. Zhu, T. K. Todorov, D. B. Mitzi, *Energy Environ. Sci.* **2012**, *5*, 7060–7065.
[20] D. A. R. Barkhouse, O. Gunawan, T. Gokmen, T. K. Todorov, D. B. Mitzi, *Prog. Photovolt. Res. Appl.* **2012**, *20*, 6–11.
[21] J. B. Li, V. Chawla, B. M. Clemens, *Adv. Mater.* **2012**, *24*, 720–723.
[22] T. Todorov, O. Gunawan, S. J. Chey, T. G. de Monsabert, A. Prabhakar, D. B. Mitzi, *Thin Solid Films* **2011**, *519*, 7378–7381.
[23] A. Fairbrother, X. Fontané, V. Izquierdo-Roca, M. Espíndola-Rodríguez, S. López, M. Placidi, L. Calvo-Barrio, A. Pérez-Rodríguez, E. Saucedo, *Sol. Energy Mater. Sol. Cells* **2013**, *112*, 97–105.
[24] A. Fairbrother, X. Fontané, V. Izquierdo-Roca, M. Placidi, D. Sylla, M. Espíndola-Rodríguez, S. López-Mariño, F. A. Pulgarín, O. Vigil-Galán, A. Pérez-Rodríguez, E. Saucedo, *unpublished results*.
[25] N. Momose, M. T. Htay, K. Sakurai, S. Iwano, Y. Hashimoto, K. Ito, *Appl. Phys. Exp.* **2012**, *5*, 081201.
[26] T. Kato, H. Hiroi, N. Sakai, S. Muraoka, H. Sugimoto, *Proc. 27th EU PVSEC*, (Frankfurt, Germany) **2012**, p. 2236.
[27] H. Araki, A. Mikaduki, Y. Kubo, T. Sato, K. Jimbo, W. S. Maw, H. Katagiri, M. Yamazaki, K. Oishi, A. Takeuchi, *Thin Solid Films* **2008**, *517*, 1457–1460.
[28] J. J. Scragg, D. M. Berg, P. J. Dale, *J. Electroanal. Chem.* **2010**, *646*, 52–59.
[29] F. O. Adurodija, J. Song, I. O. Asia, K. H. Yoon, *Sol. Energy Mater. Sol. Cells* **1999**, *58*, 287–297.
[30] A. Hölzing, R. Schurr, H. Schäfer, A. Jäger, S. Jost, J. Palm, K. Desler, P. Wellmann, R. Hock, *Thin Solid Films* **2009**, *517*, 2213–2217.
[31] R. S. Laitinen, *Acta Chem. Scand. Ser. A* **1987**, *41*, 361–376.
[32] J. Berkowitz, J. R. Marquart, *J. Chem. Phys.* **1963**, *39*, 275–283.
[33] A. K. Hearley, B. F. G. Johnson, J. S. McIndoe, D. G. Tuck, *Inorg. Chim. Acta* **2002**, *334*, 105–112.
[34] O. Šedo, M. Alberti, J. Havel, *Polyhedron* **2005**, *24*, 639–644.
[35] R. Cooper, J. V. Culka, *J. Inorg. Nucl. Chem.* **1967**, *29*, 1217–1224.
[36] A. T. Ward, M. B. Myers, *J. Chem. Phys.* **1969**, *73*, 1374–1380.
[37] J. J. Scragg, P. J. Dale, D. Colombara, L. M. Peter, *ChemPhysChem* **2012**, *13*, 3035–3046.
[38] A. Redinger, D. M. Berg, P. J. Dale, S. Siebentritt, *J. Am. Chem. Soc.* **2011**, *133*, 3320–3323.

[39] X. Fontané, L. Calvo-Barrio, V. Izquierdo-Roca, E. Saucedo, A. Pérez-Rodriguez, J. R. Morante, D. M. Berg, P. J. Dale, S. Siebentritt, *Appl. Phys. Lett.* **2011**, *98*, 181905.
[40] A. Redinger, K. Hónes, X. Fontané, V. Izquierdo-Roca, E. Saucedo, N. Valle, A. Pérez-Rodríguez, S. Siebentritt, *Appl. Phys. Lett.* **2011**, *98*, 101907.
[41] R. Scheer, A. Pérez-Rodríguez, W. K. Metzger, *Prog. Photovolt.: Res. Appl.* **2010**, *18*, 467 – 480.

Received: February 12, 2013
Published online on April 10, 2013

JACS
JOURNAL OF THE AMERICAN CHEMICAL SOCIETY
Communication
pubs.acs.org/JACS

Development of a Selective Chemical Etch To Improve the Conversion Efficiency of Zn-Rich Cu_2ZnSnS_4 Solar Cells

Andrew Fairbrother,[†] Eric García-Hemme,[†] Victor Izquierdo-Roca,[†] Xavier Fontané,[†] Fabián A. Pulgarín-Agudelo,[‡] Osvaldo Vigil-Galán,[§] Alejandro Pérez-Rodríguez,[†,∥] and Edgardo Saucedo*[,†]

[†]IREC, Catalonia Institute for Energy Research, C. Jardins de les Dones de Negre 1, 08930 Sant Adrià del Besòs, Barcelona, Spain
[‡]Centro de Investigación en Energía-UNAM, 62580 Temixco, Morelos, Mexico
[§]Escuela Superior de Física y Matemáticas, Instituto Politécnico Nacional, C.P. 07738, México D.F., Mexico
[∥]IN2UB, Departament d'Electrònica, Universitat de Barcelona, C. Martí i Franquès 1, 08028 Barcelona, Spain

Supporting Information

ABSTRACT: Improvement of the efficiency of Cu_2ZnSnS_4 (CZTS)-based solar cells requires the development of specific procedures to remove or avoid the formation of detrimental secondary phases. The presence of these phases is favored by the Zn-rich and Cu-poor conditions that are required to obtain device-grade layers. We have developed a selective chemical etching process based on the use of hydrochloric acid solutions to remove Zn-rich secondary phases from the CZTS film surface, which are partly responsible for the deterioration of the series resistance of the cells and, as a consequence, the conversion efficiency. Using this approach, we have obtained CZTS-based devices with 5.2% efficiency, which is nearly twice that of the devices we have prepared without this etching process.

Two years ago, with the challenging demonstration of a 9.7% efficiency $Cu_2ZnSn(S,Se)_4$ (CZTSSe)-based solar cell,[1] interest in these materials began to increase rapidly. CZTSSe, also commonly referred to as kesterites because of their crystal structure, are currently the most promising materials to replace $Cu(In,Ga)(S,Se)_2$ (CIGS) absorbers in photovoltaic devices in the mid- to long-term, anticipating potential limitations for mass production of CIGS-based technologies in the coming years due to the scarcity of In and Ga.[2,3] Kesterites have the advantage that they are formed by abundant or cheap and low-toxicity elements, with a direct band gap tunable between 1.0 and 1.5 eV (from pure Se to pure S compounds). In addition, they exhibit p-type conductivity and have a high light absorption coefficient, up to 1 order of magnitude higher than for CIGS, suggesting that devices with reduced thickness could function efficiently.[4] Even though the current highest efficiency values have been obtained for films with a significant Se content,[1,5] targeting a Se-free Cu_2ZnSnS_4 (CZTS)-based device is still interesting because of the lower cost of S and the lower toxicity of sulfide-related compounds compared to selenide ones. This gives motivation for the further development and optimization of CZTS-based technologies using processes compatible with scale-up to industrial and mass production levels.

Despite the promising qualities of CZTS, the maturity of kesterite-based technologies is still low, and, aside from their intrinsic peculiarities, most of the processes required to obtain the current highest efficiency devices are identical to previous CIGS technology.[1,6,7] One of the most interesting results in kesterite research is that the best efficiencies have been obtained using absorbers synthesized by means of liquid-phase methods, as opposed to the vapor-phase methods that are required for the highest efficiency CIGS devices.[1,8] A significant amount of work has been carried out to understand the physical mechanisms limiting the efficiency of CZTS solar cells fabricated using vapor-phase methods, and it has been established that Sn loss at temperatures >400 °C is one of the main limiting features during processes involving high temperatures.[7] A remarkable increase in the conversion efficiency was reported when samples were thermally treated in a Sn-containing atmosphere. As additional evidence, the decomposition of CZTS has been clearly observed when samples were heated at 560 °C in vacuum during 6 h, confirming the loss of Sn under Sn- and S-deficient atmospheric conditions.[7]

Almost all CZTS solar cells that exhibit efficiency >3% have been prepared under Cu-poor and Zn-rich conditions.[1,5,7−10] The most common compositional ranges are Cu/(Zn+Sn) ratio between 0.80 and 0.95 and Zn/Sn ratio between 1.10 and 1.25.[1,5,7−10] These ratios prevent the formation of low band gap ternary phases (with Cu−Sn−S, for example Cu_2SnS_3) which are favored in Cu-rich conditions and are considered responsible in large part for the low V_{OC} of devices prepared in such conditions. Due to the Zn excess in the best devices, Zn-rich secondary phases are expected, and in fact the presence of ZnS(Se) phases in CZTS(Se) films has been confirmed by Raman spectroscopy measurements.[11,12] However, to date no specific procedures have been adopted for the selective removal of these phases, and the classical KCN-based etching for the selective removal of Cu-rich phases such as Cu_xS_y and Cu_xSe_y,[13,14] initially developed for CIGS technologies, is still widely used in published works about CZTS.[1,6,7] In our experience, the solubility of ZnS in KCN solutions (up to KCN 10% m/v) is practically negligible.

Received: February 10, 2012
Published: April 30, 2012

   dx.doi.org/10.1021/ja301373e | J. Am. Chem. Soc. 2012, 134, 8018−8021

Some alternative etching procedures have been explored, but with limited improvement in device properties reported. One notable exception is the H_2O etching used by Katagiri to remove superficial oxide phases, leading to an improvement in efficiency from 5.74% to 6.77%.[10] Timmo and Mellikov used Br-MeOH, NH_4OH, and HCl as etchants on CZTS monograins with Zn-poor surfaces,[15,16] and Maeda used HCl on films prior to CdS deposition but did not discuss its purpose or effects.[17] The effectiveness of HCl at removing Zn-rich phases has been evidenced indirectly in some works but not explored in detail. For example, Platzer-Björkman and Scragg showed compositional depth profiles with Zn-poor surface regions in cells that were etched short times with HCl to remove the window layer for analysis,[9,18] and Lauermann noted the solubility of ZnS in HCl at room temperature but with etch times of several hours.[19]

In this Communication, we present an alternative chemical etching procedure based on hydrochloric acid solutions that has been developed for the selective removal of Zn-rich secondary phases, and we show its effectiveness in improving solar cell conversion efficiency. With this aim, we have prepared Zn-rich and Cu-poor CZTS-based solar cells by a two-stage process, involving the deposition of Sn/Cu/Zn metallic stacks by means of DC-magnetron sputtering onto Mo-coated soda-lime glass substrates, followed by reactive annealing under a sulfur- and tin-containing atmosphere. The composition ratios of the precursor stack as measured by X-ray fluorescence spectroscopy (XRF) are Cu/(Zn+Sn) = 0.73 and Zn/Sn = 1.27, while the sulfurized samples before etching have ratios of Cu/(Zn+Sn) = 0.80 and Zn/Sn = 1.55, the difference being due to Sn loss during annealing. The composition ratios after 300 s of etching in HCl (5% v/v, 75 °C) are Cu/(Zn+Sn) = 1.00 and Zn/Sn = 1.15. The effects of HCl concentration and etch time are described in more detail in the Supporting Information (SI).

After etching of the absorbers, glass/Mo/CZTS/CdS/ZnO(i)/ZnO(Al) cells were produced by chemical bath deposition of the CdS buffer layer, followed by two-stage sputtering deposition of the ZnO layers (see the SI for experimental details).

Figure 1 shows the Raman spectra measured with 325 nm (UV) excitation wavelength (blue spectra) and 514 nm excitation wavelength (red spectra) from the as-grown sample (curves labeled (a)) and from the samples etched with the HCl solution (curves labeled (b) and (c)). The spectrum measured from the as-grown sample with the UV excitation wavelength is dominated by three intense peaks at 348, 696, and 1044 cm^{-1}, which are identified as the first-, second-, and third-order peaks characteristic of the ZnS phase.[11] The high intensity of these peaks is due to the existence of a quasi-resonant excitation of the ZnS vibrational modes at these excitation conditions, in which Raman spectroscopy becomes extremely sensitive in the detection of even small quantities of ZnS in the sample.[11] This spectrum also shows a contribution at 338 cm^{-1} (appearing as a shoulder at the low-frequency side of the dominant first-order ZnS peak) and a weaker peak at 287 cm^{-1} which correspond to the main A1 modes characteristic of the CZTS phase.

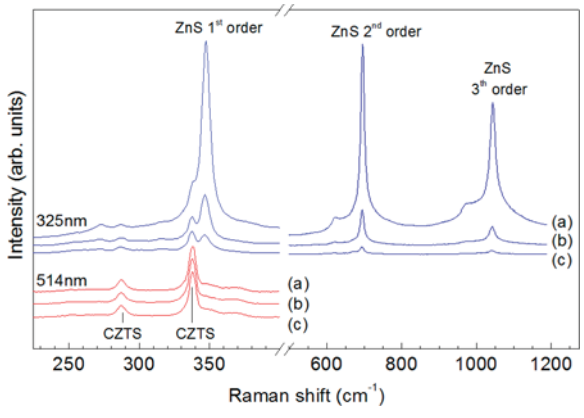

Figure 1. Raman spectra taken for the as-grown sample (a), sample etched with a solution of HCl (5% v/v) at 75 °C for 90 s (b), and sample etched with HCl solution (5% v/v) at 75 °C for 300 s (c). Excitation wavelengths: 325 nm (blue spectra), 514 nm (red spectra).

After chemical etching with a solution of HCl (5% v/v, 75 °C, 90 s), the intensity of the ZnS Raman peaks is drastically reduced (Figure 1, blue spectrum (b)), and for longer etching times (300 s, Figure 1, blue spectrum (c)) the ZnS Raman peaks are reduced even more. In contrast, under equivalent measurement conditions, the Raman peaks corresponding to CZTS remain unaffected, in both their intensity and spectral features (frequency, width). This suggests that the proposed chemical etching does not significantly affect the kesterite surface. To confirm this, the same analysis was made using a 514 nm excitation wavelength, which is well suited for analysis of the dominant kesterite phase (see red spectra in Figure 1). No significant changes in the spectra from the different samples are observed, confirming that the proposed etching procedure does not significantly affect the CZTS surface. It is important to remark that sample etched by the classical KCN route (aqueous solution 10% m/v, 25 °C, 120 s) does not show any significant difference in the Raman spectra measured with both excitation wavelengths in comparison with the as-grown sample, confirming the ineffectiveness of this procedure to eliminate the ZnS secondary phase.

This agrees with the measurements that we performed on the solubility of 20 mg of some potential secondary phases of the system both in 20 mL of a KCN solution (aqueous solution 10% m/v, 25 °C, 120 s) and in an HCl solution (aqueous solution 5% v/v, 75 °C, 300 s). For the KCN etching we obtained the following results: CuS, completely soluble; ZnS, insoluble; and SnS, insoluble. For the HCl etching we obtained the following results: CuS, insoluble; ZnS, completely soluble; and SnS, slightly soluble. This chemical approach supports the high selectivity of our proposed etching process for the ZnS binary phase. It is important to note that the solubility of Sn-rich phases in HCl is noted by Timmo, Mellikov, and Li in CZTS,[15,16,20] but the presence of SnS in Zn-rich films tends to be related to peculiarities of that specific system, i.e., a Sn-rich surface or localized SnS phase formation due to Sn layer nonuniformity. In fact, by using inductively coupled plasma mass spectroscopy (ICP-OES), we estimate that the solubility of ZnS is ~2 orders of magnitude greater under similar dissolution conditions than that of SnS (see SI for more details). Also, we analyzed the supernate after the etching marked as (c) in the Figure 1, obtaining the following composition results: [Zn], 0.4 ppm; [Cu] and [Sn], not detected. This compositional analysis supports the observed insolubility and low solubility of CuS and SnS in HCl respectively.

The distribution of the ZnS secondary phase on the surface of the samples and its dependence on the etching processes have also been investigated by Raman scattering mapping measurements performed under UV excitation conditions.

dx.doi.org/10.1021/ja301373e | J. Am. Chem. Soc. 2012, 134, 8018−8021

Figure 2A shows an optical image on the surface of the as-grown sample, where dark areas correspond to ZnS-rich regions

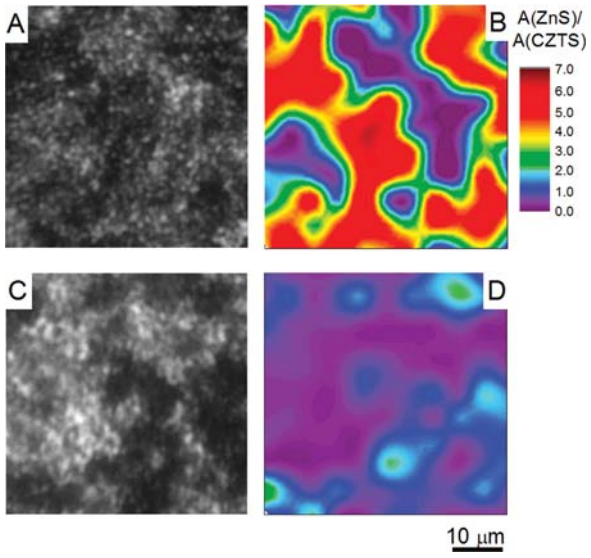

Figure 2. Optical image of the as-grown sample (A) and UV Raman mapping in the same area, representing the ratio between the intensity of the main ZnS Raman mode at 348 cm^{-1} and that of the main CZTS A1 mode at 338 cm^{-1} (B). Optical image of the sample etched with the solution of HCl (5% v/v, 75 °C) for 300 s (C) and UV Raman mapping in the same area, representing the ratio between the intensity of the main ZnS Raman mode at 348 cm^{-1} and that of the main CZTS A1 mode at 338 cm^{-1} (D).

and white areas to CZTS-rich regions. The UV Raman mapping in Figure 2B shows in a color code the ratio between the intensity of the main ZnS Raman peak at 348 cm^{-1} and that of the main A1 CZTS mode at 338 cm^{-1}, with red areas corresponding to regions with high ZnS content and violet areas corresponding to regions with low ZnS content. This Raman mapping correlates strongly with the optical image, showing the nonuniform distribution of ZnS on the surface, similar to the distribution of Cu_xS in CIGS.[14] After the etching process with an HCl-based solution, a drastic reduction of the black areas in the optical image is clearly seen, as well as corresponding changes in the UV Raman mapping. The ZnS phase is practically eliminated from the entire sample surface, with only residual quantities of ZnS found in certain places. This is a very important result, because for the first time we shown unambiguously the effectiveness of this selective etching for the elimination of ZnS.

An additional proof of concept for the presented chemical etching process is reflected in its effect on the optoelectronic parameters of the cells made with the different absorbers. Figure 3 shows the illuminated $J-V$ characteristics of the solar cells prepared with three different absorber layers: the as-grown layer, that obtained after the classical KCN etching, and that obtained after our novel HCl-based etching. Comparing the optoelectronic parameters, the classical KCN etching gives limited improvement to the results obtained from the unetched (as-grown) sample. The conversion efficiency is improved slightly, from 2.7% to 3.3%, as presented in the table shown in Figure 3. In contrast, the largest improvement on the optoelectronic parameters is achieved when the HCl-based etch is applied to the samples, giving solar cells with 5.2% conversion efficiency. This improvement is clearly seen over

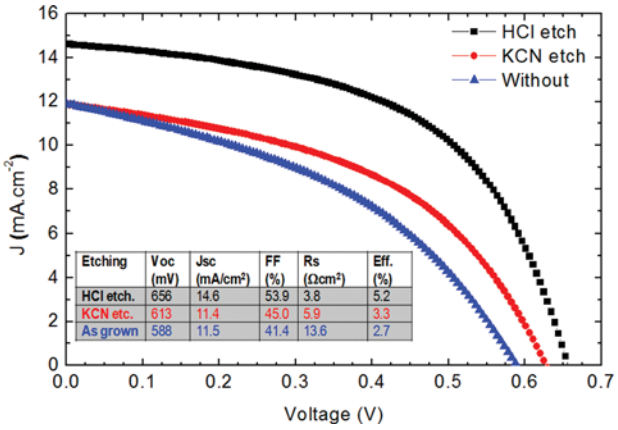

Etching	Voc (mV)	Jsc (mA/cm²)	FF (%)	Rs (Ωcm²)	Eff. (%)
HCl etch.	656	14.6	53.9	3.8	5.2
KCN etc.	613	11.4	45.0	5.9	3.3
As grown	588	11.5	41.4	13.6	2.7

Figure 3. Illuminated $J-V$ characteristics (AM1.5G filter, 100 mW/cm^2) of the solar cells prepared from the as-grown absorber, the absorber etched with KCN, and the absorber etched with HCl. Optoelectronic parameters have been extracted from these curves.

various samples, where the following average efficiencies were obtained: HCl treated, 9 samples, Eff. = 4.9 ± 0.3%; KCN treated, 6 samples, Eff. = 2.8 ± 0.5; and as grown, 6 samples, Eff. = 2.4 ± 0.3. As is clearly observed in Figure 3 and the corresponding table, this improvement is mainly related to those of the short-circuit current and the series resistance. These changes are directly related to the significant reduction of the content of the ZnS phase on the CZTS surface. The presence of this phase leads mainly to a degradation (increase) of the series resistance of the devices because of its high band gap, as has been previously suggested.[9]

The effectiveness of this etching process for Zn-rich phases (ZnSe) in CZTSe has not been studied as extensively as for the case of ZnS in CZTS. However, we have preliminary results to show that there is some reduction of the Zn and ZnSe signals as measured by XRF and Raman spectroscopy, albeit not as drastically as for ZnS. After etching in HCl (10% v/v, 75 °C, 600 s), the composition ratio Zn/Sn as measured by XRF changes from 1.53 to 1.34, and the intensity of the main ZnSe mode reduces ∼12% (see SI). Further optimization of the etching process, i.e., with different mineral acids, concentration, temperature, and etch time, may prove it to be ideal for CZTSSe films of varied S−Se content.

In summary, our preliminary results show the effectiveness of the proposed HCl-based etch for the selective removal of superficial Zn-rich secondary phases. This etching process has a significant impact on the optoelectronic parameters of the solar cells, markedly influencing the J_{sc} and R_s parameters and, consequently, the conversion efficiency of the devices. This opens the possibility for a customized process for CZTS technologies that is more environmentally friendly and considerably less toxic than the classical KCN etch. These results can be considered very important for the future industrial implementation of this low-cost technology.

■ ASSOCIATED CONTENT

Ⓢ Supporting Information

Experimental methods and characterization techniques. This material is available free of charge via the Internet at http://pubs.acs.org.

AUTHOR INFORMATION

Corresponding Author
esaucedo@irec.cat

Notes
The authors declare no competing financial interest.

ACKNOWLEDGMENTS

The research leading to these results has received funding from the People Programme (Marie Curie Actions) of the European Union's Seventh Framework Programme FP7/2007-2013/ under REA grant agreement no. 269167). The research was also partially supported by MINECO, project KEST-PV (ref. ENE2010-121541-C03-1). Authors from IREC and the University of Barcelona belong to the M-2E (Electronic Materials for Energy) Consolidated Research Group and the XaRMAE Network of Excellence on Materials for Energy of the "Generalitat de Catalunya". E.S. thanks the MINECO, Subprogram Ramón y Cajal (ref. RYC 2011-09212), and V.I.-R. thanks Subprogram Juan de la Cierva (ref. JCI-2011-10782).

REFERENCES

(1) Todorov, T.; Reuter, K. B.; Mitzi, D. B. *Adv. Mater.* **2010**, *22*, E156.
(2) Andersson, B. A. *Prog. Photovolt.: Res. Appl.* **2000**, *8*, 61.
(3) Wadia, C.; Alivisatos, A. P.; Kammen, D. M. *Environ. Sci. Technol.* **2009**, *43*, 2072.
(4) Persson, C. *J. Appl. Phys.* **2010**, *107*, 053710.
(5) Barkhouse, D. A. R.; Gunawan, O.; Gokmen, T.; Todorov, T. K.; Mitzi, D. B. *Prog. Photovolt.: Res. Appl.* **2011**, *20*, 6.
(6) Schubert, B.-A.; Marsen, B.; Cinque, S.; Unold, T.; Klenk, R.; Schorr, S.; Schock, H.-W. *Prog. Photovolt.: Res. Appl.* **2011**, *19*, 93.
(7) Redinger, A.; Berg, D. M.; Dale, P. J.; Siebentritt, S. *J. Am. Chem. Soc.* **2011**, *133*, 3320.
(8) Guo, Q.; Ford, G. M.; Yang, W.; Walker, B. C.; Stach, E. A.; Hillhouse, H. W.; Agrawal, R. *J. Am. Chem. Soc.* **2010**, *132*, 17384.
(9) Platzer-Björkman, C.; Scragg, J.; Flammersberger, H.; Kubart, T.; Edoff, M. *Sol. Energy Mater. Sol. Cells* **2012**, *98*, 110.
(10) Katagiri, H.; Jimbo, K.; Yamada, S.; Kamimura, T.; Maw, W. S.; Fukano, T.; Ito, T.; Motohiro, T. *Appl. Phys. Exp.* **2008**, *1*, 041201.
(11) Fontané, X.; Calvo-Barrio, L.; Izquierdo-Roca, V.; Saucedo, E.; Pérez-Rodriguez, A.; Morante, J. R.; Berg, D. M.; Dale, P. J.; Siebentritt, S. *Appl. Phys. Lett.* **2011**, *98*, 181905.
(12) Redinger, A.; Hönes, K.; Fontané, X.; Izquierdo-Roca, V.; Saucedo, E.; Valle, N.; Pérez-Rodríguez, A.; Siebentritt, S. *Appl. Phys. Lett.* **2011**, *98*, 101907.
(13) Weber, M.; Scheer, R.; Lewerenz, H. J.; Jungblut, H.; Störkel, U. *J. Electrochem. Soc.* **2002**, *149*, G77.
(14) Weinhardt, L.; Fuchs, O.; Groß, D.; Umbach, E.; Heskeb, C.; Dhere, N. G.; Kadam, A. A.; Kulkarni, S. S. *J. Appl. Phys.* **2006**, *100*, 024907.
(15) Timmo, K.; Altosaar, M.; Raudoja, J.; Grossberg, M.; D'Anilson, M.; Volobujeva, O.; Mellikov, E. Proceedings of the 35th IEEE Photovoltaic Specialists Conference, Honolulu, HI, 2010; 001982.
(16) Timmo, K.; Altosaar, M.; Raudoja, J.; Volobujeva, O.; Kauk, M.; Krustok, J.; Varema, T.; Grossberg, M.; Danilson, M.; Muska, K.; Ernits, K.; Lehner, F.; Meissner, D. *Mater. Challenges Alternative Renewable Energy: Ceramic Trans.* **2011**, *224*, 137.
(17) Maeda, K.; Tanaka, K.; Fukui, Y.; Uchiki, H. *Sol. Energy Mater. Sol. Cells* **2011**, *95*, 2855.
(18) Scragg, J.; Berg, D.; Dale, P. *J. Electroanal. Chem.* **2010**, *646*, 52.
(19) Lauermann, I.; Bär, M.; Fischer, C.-H. *Sol. Energy Mater. Sol. Cells* **2011**, *95*, 1495.
(20) Li, X.; Wang, D.; Du, Q.; Liu, W.; Jiang, G.; Zhu, Ch. *Adv. Mater. Res.* **2012**, *418*−*420*, 67.

Development of a selective chemical etch to improve the conversion efficiency of Zn-rich Cu_2ZnSnS_4 solar cells

Andrew Fairbrother, Eric García-Hemme, Victor Izquierdo-Roca, Xavier Fontané, Andrés F. Pulgarín-Agudelo, Osvaldo Vigil-Galán, Alejandro Pérez-Rodríguez and Edgardo Saucedo

Supporting information

Methods

Metallic layer deposition by DC-magnetron sputtering: precursor Sn/Cu/Zn metallic stacks have been deposited by DC-magnetron sputtering (Ac450 Alliance Concepts) using 99.99% purity targets, onto 10x10 cm^2 Mo coated soda-lime glass (500 nm, R□ = 0.25 Ω/□). The Sn/Cu/Zn stack order was selected in order to prevent or reduce the evaporation of volatile SnS species during the annealing process [Supp1]; Cu was deposited in the middle of the stack because of its high diffusion coefficient; and finally Zn was deposited on the top of the stack to ensure that the ZnS secondary phase formed mostly on the surface after the reactive anneal, which is particularly important because Zn was deposited in excess (Cu/(Zn+Sn) = 0.73, Zn/Sn = 1.27). The conditions for the deposition of each metal were: Sn (0.64 W/cm^2, 0.001 mBar, 42 min), Cu (1.27 W/cm^2, 0.001 mBar, 23 min) and Zn (1.27 W/cm^2, 0.001 mBar, 17 min). In all cases the substrate was rotated at 10 rpm and unheated, i.e. deposition at room temperature, though some heating may occur as a result of the deposition process. The thickness of the stacks was determined by X-ray fluorescence spectroscopy (XRF) (Fisherscope XVD) - previously calibrated with inductively coupled plasma optical emision spectroscopy (ICP-OES) - in order to measure the composition.

Reactive annealing: the metallic precursor samples (2.5x2.5 cm^2 in area) were reactively annealed in a three zone tubular furnace capable of working in vacuum (10^{-4} mBar) and inert gas atmosphere (Ar). For this step a graphite box (23.5 cm^3 in volume) was used for the reactive annealing under a sulfur atmosphere at 550 ºC ± 2 ºC during 30 min in a 1 Bar Ar atmosphere, and using two crucibles, one with 50 mg of sulfur powder (Alfa-Aesar, 99.995%) and the other with 4-5 mg of tin powder (Alfa-Aesar, 99.999%). The heating ramp was 20 ºC/min, and the natural cooling down to room temperature typically took 2 hours.

Etching process: a set of samples were submitted to a classical etching with a KCN solution (Sigma-Aldrich, 98%), 10% m/V in deionized water (18 MΩ) with few drops of a 1M KOH solution (to ensure basicity for safety reasons) during 120 seconds at 25 ºC, and then rinsed several times with deionized water. A second set of samples were etched with HCl 10% V/V at 75 ºC during 300 seconds and then carefully rinsed first with a 1M KOH solution, followed by deionized water. A third set of samples were treated only with deionized water at room temperature for 300 s. All the samples were dried in a N_2 flux before proceeding to the device fabrication.

Device fabrication: devices were fabricated by depositing CdS (60 nm) by chemical bath deposition onto the kesterite layers, followed DC-pulsed sputtering deposition of i-ZnO (50 nm) and ZnO:Al (450 nm, R□ = 19 Ω/□) (CT100 Alliance Concepts). For the optoelectrical characterization 3x3 mm^2 cells were scribed using a micro diamond scriber MR200 OEG, thus avoiding the necessity of metallic grid deposition onto the ZnO:Al surface.

I-V characterization under illumination: to measure the optoelectronic properties a Sun 3000 class AAA solar simulator from Abet Technology (uniform illumination area of 15x15 cm^2) was used. Measurements were carried out after the calibration of the system with a reference Si solar cell under AM 1.5 illumination and fixing the temperature of the samples to 298 K.

Raman Spectroscopy:

Visible-excitation: macro Raman measurements were performed with a T64000 Horiba-Jobin Yvon spectrometer in backscattering configuration using a 514 nm excitation wavelength with the laser spot focused on surface of the kesterite films. The power was kept below 5 mW for a spot diameter of approx. 100 μm in order to avoid the presence of thermal effects in the spectra and to integrate the signal of a more representative area when compared to a micro Raman configuration.

UV-excitation: Raman microprobe measurements were performed with a LabRam HR800-UV Horiba-Jobin Yvon spectrometer coupled with an Olympus metallographic microscope. Backscattering measurements were made using a 325 nm excitation wavelength with the laser spot focused on the surface of the kesterite films. The power was kept below 0.4 mW at a magnification of 40X (spot diameter approx. 1 μm), scanning a 30x30 μm^2 area with the Duo-Scan™ accessory, in order to integrate the signal of a more representative area. The wavelength was chosen in order to reach pre-resonant excitation conditions for the ZnS phase with the aim of strongly enhancing its signal. Mapping measurements were performed using a motorized x-y table coupled to the Raman set-

up over a 50x50 μm^2 area with 5 μm steps using a punctual spot of about 1 μm diameter at 0.4 mW.

This supporting material includes additional morphological, structural and compositional information to directly show that the main changes in the films after the chemical etching with the HCl solution is the selective elimination of the ZnS binary without affecting the CZTS main phase. This is a very important issue because it is requisite that the etchant has a negligible effect on the absorber layer.

Figure S1 shows the cross sectional image of the complete cells studied in this paper, where Figure S1 (a) corresponds to the sample etched with KCN and Figure S1 (b) to the sample etched with HCl. In the Figures from bottom to top, the substrate, the Mo back contact, the CZTS absorber and the CdS/i-ZnO/ZnO:Al front contact are clearly shown. Although not observable in the Figure, a very thin MoS_2 layer was formed between the Mo back contact and the CZTS absorber, which was clearly detected by Raman spectroscopy. The morphology of the absorber is very similar in both cases and is formed by small crystallites with sizes ranging from hundreds of nanometers up to 1 μm, as is typical for CZTS grown by this method [Supp1, Supp2]. No significant differences are observed between both absorbers as was expected because the samples were produced in the same experimental run. This information supports our hypothesis that the main differences in the optoelectronic response of the absorbers are not related to its morphological/structural properties, nor to the properties of the other layers forming the solar cells, but to the etching procedure.

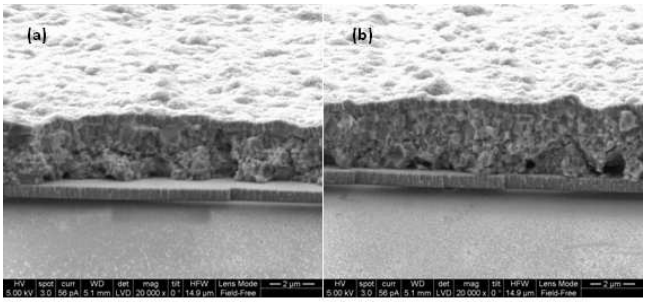

Figure S1: Cross sectional SEM images of the typical solar cell obtained with our process, where the glass substrate, molybdenum back contact, absorber and window layers are clearly observed. Sample etched in KCN (a) and sample etched in HCl (b).

To further support the hypothesis about the selectivity of the proposed etching for Zn-rich phases, compositional measurement on the surface before and after etching with HCl using X-ray photoemission spectroscopy (XPS) were carried out with a PHI-ESCA 5500 (see Figure S2). With this technique we are able to analyze approximately the first 300 nm of the absorber, i.e. it is very sensitive to the surface composition. In the as-grown sample (black line in Figure S2) the Sn, Cu and Zn signals are observed and we use the Sn3p3, Sn3p1, Cu2p3, Cu2p1, Zn2p3 and Zn2p1 peaks to follow the evolution of the three elements. Samples etched with KCN do not show any remarkable difference in the XPS spectra with respect to the as grown one, confirming the limited impact of this etchant on the surface composition (spectra not shown). After the HCl based etch the signal intensity of the samples changes in a different way depending on the analyzed element. In particular, the Sn and Cu signals are increased whereas the Zn signal decreases. This is in agreement with the proposed selectivity of the etching process for Zn-based secondary phases. The reduction of the Zn signal is explained by the removal of the ZnS binary on the surface in good agreement with the UV-Raman spectroscopy analysis. In addition, removal of the top ZnS layer leads to the observed increase in the Sn and Cu signals after the etching process. It is important to remark that no significant change is observed in the shape and position of the peaks, indicating that the chemical etching apparently does not oxidize the surface layers although it is an oxidizing medium. This is consistent with the absence of any effect of the etching process on the CZTS absorber layer, in agreement with the strong selectivity of the proposed etchant.

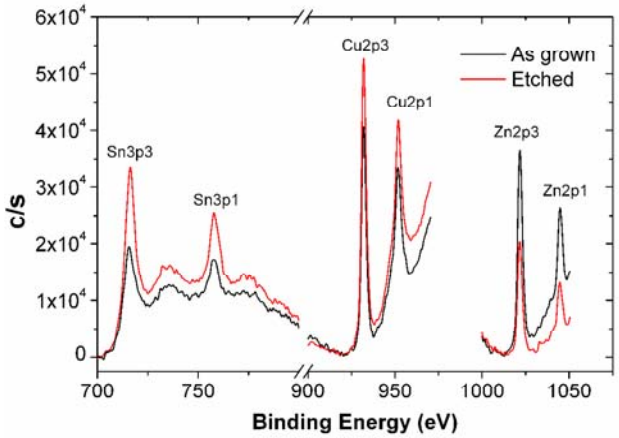

Figure S2: XPS spectra of the as-grown sample (black line) and etched sample (red line). The etching was: HCl 10% V/V at 75 ºC during 300 s.

To show the concentration and time dependence of the etching process a series of identical samples were prepared with enough excess Zn to ensure the formation of a high quantity of ZnS on the surface. After the sulfurization of the Zn-rich precursor a Zn/Sn ratio of 1.55 is obtained and the presence of a high amount of ZnS was confirmed by means of UV-Raman spectroscopy (Figure not shown). Samples were submitted to two different etching processes (with HCl 5% V/V and 10% V/V, at 75 ºC), analyzing the effect of each etchant with time. The composition of the layers was measured using XRF. Figure S3 shows the compositional evolution of samples treated with HCl 5% V/V. The Zn/Sn ratio diminished with treatment time up to 450 s, where it stabilized at values close to 1.3. Further times seem to have a limited effect on the composition, probably due to the evaporation of HCl because the treatment is carried-out at 75 ºC. Consequently, the Cu/(Zn+Sn) ratio increased with time, which could be explained by the diminution of the Zn concentration. The lower part of Figure S3 confirms this, where the Zn concentration is

greatly affected by the etch time in comparison with Cu and Sn concentrations.

The effect of the etching process is greatly enhanced when the HCl concentration is increased to 10% V/V, as is presented in Figure S4. The Zn/Sn ratio decreased in the first 120 s stabilizing at a ratio of 1.15. Consequently the Cu/(Zn+Sn) ratio increased from 0.8 to nearly 1.0 in the same time range. Longer times did not have any further significant compositional change in the layers, probably because of HCl evaporation at 75 ºC. The diminution of the Zn concentration is more flagrant in this case, as is observed in the lower part of the Figure S4.

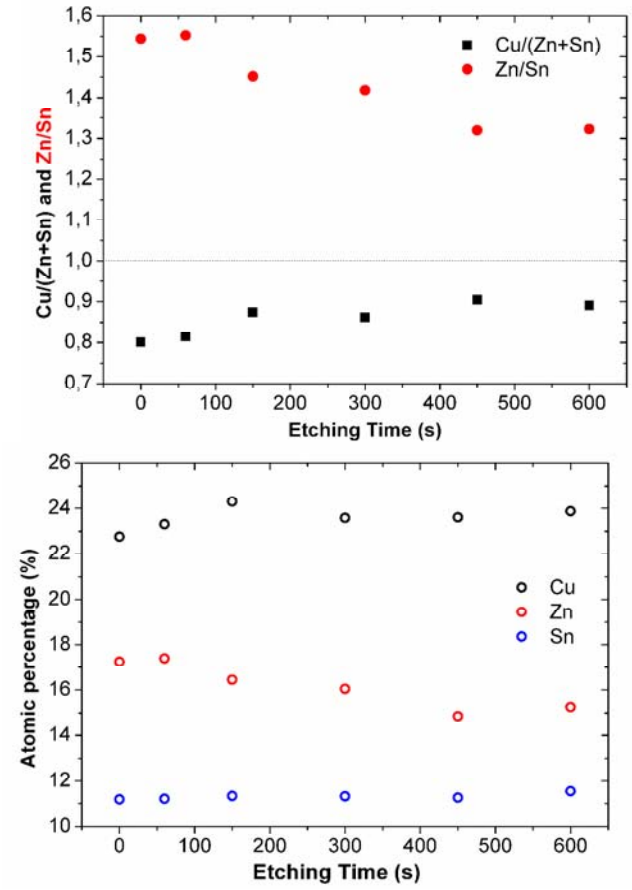

Figure S3: Evolution as a function of the time of the Zn/Sn ratio, Cu/(Zn+Sn) ratio (top), Zn, Cu and Sn atomic concentration (bottom) before and after etching with HCl 5% V/V at 75 ºC.

The solubility of the potential binaries of the CZTS system - CuS, SnS, and ZnS were studied by dissolving 20 mg in 20 mL of HCl (10% V/V) at 75 ºC during 600 s. The supernates were then centrifuged and analyzed by ICP-OES. Table S1 summarizes the compositional analysis for the three binaries, confirming the low solubility of CuS, the limited solubility of SnS, and the high solubility of ZnS in the etchant (approximately 2 orders of magnitude higher than for SnS).

Binary	[Cu] ppm	[Sn] ppm	[Zn] ppm
CuS	0	0	0
SnS	0	0.3	0
ZnS	0	0	28.9

Table S1. Test of solubility of the different binaries in HCl 10% V/V at 75 ºC during 600 s.

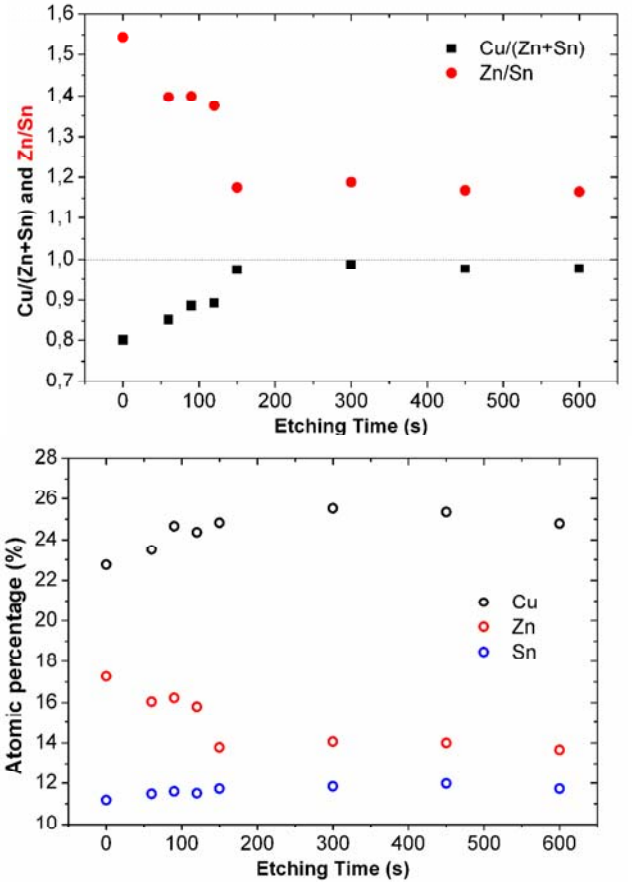

Figure S4: Evolution as a function of the time of the Zn/Sn ratio, Cu/(Zn+Sn) ratio (top), Zn, Cu and Sn atomic concentration (bottom) before and after the etch with HCl 10% V/V at 75 ºC.

Finally, we have analyzed the possible extension of this etch process to the case of ZnSe in CZTSe. The etching of the surface of ZnSe crystals with HCl at different concentrations has been reported as moderate (3.5 g/(h.cm^2) with HCl 6M at room temperature), decreasing notably with time [Supp3]. We have tested the etching of $Cu_2ZnSnSe_4$ (CZTSe) films with initial Zn/Sn ratio of 1.53, by using HCl 10% V/V at 75 ºC, during 600 s. The Zn/Sn ratio decreased to 1.34, indicating that the etch is considerably less effective than in the case of the ZnS, where the Zn/Sn ratio decreases to 1.15 under the same etching conditions. To confirm this, we have performed pre-resonant Raman characterization by using a 457.9 nm excitation wavelength, which is especially suited to detect even small quantities of ZnSe. Figure S5 shows the spectra taken in the as grown and HCl etched samples. Although a diminution of the ZnSe Raman signal is observed suggesting a

reduction in the ZnSe quantity, the impact is very limited in comparison with the sulfide case. In fact, cells prepared without etching exhibit a conversion efficiency of (4.1 ±0.3) %, whereas samples etched with HCl under such conditions (4.4 ± 0.4) %, confirming the limited effect of this etching process in the selenide case.

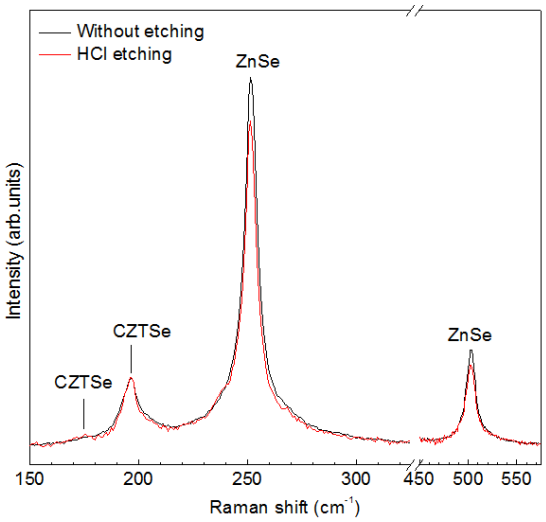

Figure S5. Pre- resonant Raman spectra of CZTSe films before and after the HCl based etch (excitation wavelength 457.9 nm).

In summary, we have presented additional morphological, structural and compositional information with the aim of unambiguously confirming the effectiveness and selectivity of the proposed hydrochloric acid based etching. All our results strongly suggest that this methodology is useful for the etching of ZnS secondary phase on the surface of Cu_2ZnSnS_4 films, and in the future could be a simple and interesting way to eliminate this secondary phase which has a detrimental impact on the optoelectronic parameters of the CZTS based devices. The methodology presented here is very well suited for the etching of Zn-rich phases in pure Cu_2ZnSnS_4, and potentially in S-rich $Cu_2ZnSn(Se,S)_4$ pentenary compounds, but is considerably less effective in the case of the pure selenide and Se-rich films, which will need an alternative etching process different to the simple and effective way presented here.

Additional References

[Supp1] H. Katagiri, K. Jimbo, W.S. Maw, K. Oishi, M. Yamazaki, H. Araki, and A. Takeuchi, *Thin Solid Films* **517** (2009) 2455.

[Supp2] H. Katagiri, K. Jimbo, S. Yamada, T. Kamimura, W.S. Maw, T. Fukano, T. Ito, and T. Motohiro, Applied Physics Express 1 (2008) 041201.

[Supp3] E. M. Gavrishchuk, E. Yu. Vilkova, O. V. Timofeev, U. P. Borovskikh, and E. L. Tikhonova, *Inorganic Materials* **43** (2007) 579.